Astronomy Reports, Vol. 47, No. 2, 2003, pp. 110–118. Translated from Astronomicheskiĭ Zhurnal, Vol. 80, No. 2, 2003, pp. 130–139.

Radio Identification and Continuum Spectra of Decameter-Wavelength Sources

O.V. Verkhodanov[1], N. V. Verkhodanova[1], and H. Andernach[2]

[1]*Special Astrophysical Observatory, Russian Academy of Sciences, Nizhniĭ Arkhyz, Karachaevo-Cherkesskaya Republic, 357169 Russia*

[2]*University of Guanajuato, Department of Astronomy, Apdo Postal 144, Guanajuato, GTO, CP36000, México*

Received March 22, 2002; in final form, June 26, 2002

Abstract—The paper describes a method for the radio identification of decameter-wavelength sources based on their continuum spectra and analysis of their coordinates in relatively large error boxes surrounding a specified position on the sky. The distribution of continuum spectra and identifications in other wavelength ranges are analyzed for the resulting radio catalog. Using identifications with the FIRST and NVSS surveys, the statistics of the spectral index–size and spectral index–flux density distributions for steep-spectrum sources have been studied, and a catalog of ultrasteep-spectrum ($\alpha < -1.2$) decameter-wavelength sources has been compiled. © *2003 MAIK "Nauka/Interperiodica".*

1. INTRODUCTION

The catalog of 1822 radio sources obtained with the UTR telescope (Kharkov) by Braude *et al.* [1–5] at 10, 12.6, 14.7, 16.7, 20, and 25 MHz covers about 30% of the sky and is the lowest-frequency catalog currently available. It can be used to cross-identify objects at low frequencies and to construct their spectra, or to derive upper limits for the decameter fluxes of northern sources. The original publications do not give information on the identifications of 121 (7%) sources, and there are no optical identifications for most of the sources (81%).

Our aim was to identify as many of the UTR objects as possible with known radio sources. Cross identification and further studies enabled us to revise the coordinates of the radio sources and obtain their radio spectra. We used the new coordinates for a number of objects to obtain optical identifications with objects in the Palomar Digital Sky Survey. The spectral data have enabled us to construct samples of decameter sources with various types of spectra, such as samples of steep-spectrum sources.

2. DATA CLEANING

The problems encountered when constructing the radio spectra of sources from the UTR catalog that have been detected on the T-shaped Kharkov radio telescope [6] at decameter wavelengths (10, 12.6, 14.7, 16.7, 20, and 25 MHz) are associated first and foremost with the identification of sources within large error boxes; in this case, the error box is a $40' \times 40'\mathrm{cosec}\delta$ window obtained from a cross identification with the CATS database [7]. We addressed this problem via interactive processing of the radio spectra [8] obtained through a cross-identification of the UTR objects with sources from the CATS database using a 40′ identification window. The main parameters of the catalogs used for the identifications are listed in Table 1.

The spectra were cleaned with the spg software [22] using a verified technique [8]. In the cleaning, we

Table 1. Basic catalogs used for the identification of the decameter objects

Name	Frequency, MHz	HPBW	S_{lim}, mJy	Reference
6C	151	4.2′	∼200	[9, 10]
7C	151	1.2	80	[11]
MIYUN	232	3.8	∼100	[12]
WENSS	325	0.9	∼18	[13]
TXS	365	∼ 0.1	∼200	[14]
B3	408	3 × 5	100	[15]
WB92	1400	10 × 11	150	[16]
87GB	4850	3.7	25	[17]
GB6	4850	3.7	15	[18]
PMN	4850	4.2	30	[19]
MSL	Var.	Var.	Var.	[20, 21]

1063-7729/03/4702-0110$24.00

eliminated sources whose spectra did not reach the UTR catalog values when approximated by standard curves. The searches for candidates for identifications consisted of several steps.

(1) We performed a cross-identification of the UTR objects [1–5] with the main radio catalogs of the CATS database [7], except for the highly sensitive (to 2.5 mJy) NVSS catalog [23].

(2) We selected all objects from the resulting list in the search box ($40' \times 40'$) for which there were data at several different frequencies.

(3) The spectrum of each object was approximated by a curve and extrapolated to the UTR frequencies.

(4) From the resulting list of objects inside this box, we selected radio sources satisfying the following conditions:

(a) the estimated flux densities at the UTR frequencies are the closest to the observed fluxes (the flux estimation was done by fitting a curve to the spectrum at the given frequency);

(b) the source positions are the closest to the center of gravity of the coordinates of the UTR objects.

Each UTR source has from one to four identification candidates (Fig. 1). We assumed that all candidate objects satisfying the above criterion contribute to the UTR source; i.e., they are blended.

(5) The coordinates used for further identification were taken from the Texas (365 MHz) [14], GB6 (4850 MHz) [18], and PMN (4850 MHz) [19] catalogs (in order of decreasing preference). As a rule, data from at least one of these catalogs are present for the objects falling into the error box.

(6) If the identification area is poor in objects (e.g. at a low declination), so that there are no sources with data at several frequencies for the spectrum approximation, we used all the objects in the error box for the subsequent analysis.

(7) We used the resulting positions to obtain identifications with objects in the NVSS catalog [23]; the NVSS data (flux densities) were then used to revise the spectra.

(8) We adopted the NVSS positions as the most accurate ones if there was an identification with an NVSS object; otherwise we used the positions obtained in step (5).

(9) The resulting coordinates were used for identification with nonradio catalogs and for APM [24] identifications of the UTR objects.

The spectra were checked using a number of low-frequency catalogs—6C (151 MHz) [9, 10], 3C, and 4C (178 MHz) [25–27]—as well as catalogs included in the Master List [20, 21]—CL (26 MHz) [28], WKB (38 MHz) [29], and MSH (85 MHz) [30–32]. Although they do not overlap with all the UTR bands, these demonstrate the high effectiveness of the proposed technique in the sky regions where observation areas intersect.

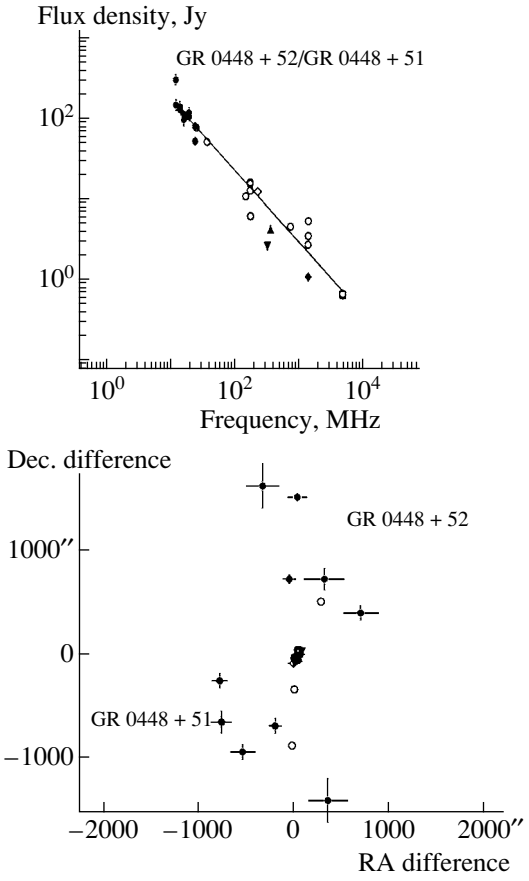

Fig. 1. Upper: spectra of two sources contributing to a UTR object. They are virtually indistinguishable in the plot. Lower: locations of the two blended sources and of the corresponding UTR object in the plane of the sky. The data have been cleaned. Filled circles: UTR points.

After obtaining identifications and more accurate positions, we performed cross-identifications with objects from the NVSS [23] and FIRST [33] catalogs, whose basic parameters are listed in Table 2. The cross-identifications with these catalogs enabled us to improve the positions and distinguish multicomponent objects.

3. THE CATALOG OF IDENTIFICATIONS

Using the identifications of the UTR sources, we compiled a catalog of 2316 objects (Catalog 1, accessible at http://cats.sao.ru/doc/UTR_ID.html and astro-ph/0008431 [34]), which includes all the identified blends. The catalog contains the equatorial coordinates; spectral indices at 365, 1400, and 5000 MHz; parameters of the fitted curves; and information about the presence of detected optical,

Table 2. Parameters of the catalogs used to improve the positions

Name	Frequency, MHz	HPBW	$S_{\rm lim}$, mJy	Reference
NVSS	1400	0.75′	2.5	[23]
FIRST	1400	0.08	1	[33]

infrared, or X-ray radiation. When processing the spectra, we used the parameterization $\log S(\nu) = A + Bx + C(x)$, where S is the flux in Jy, x is the logarithm of the frequency ν in MHz, and $f(x)$ is one of the following functions: $\exp(-x)$, $\exp(x)$, or x^2. In addition, the list contains all identified blends and the corresponding names of the radio sources from the 3C [25, 26], 4C [27], and PKS [35] catalogs.

For three sources—GR 0801−11, GR 0930−00, and GR 1040−02—we found no identifications in the above catalogs. We were not able to obtain

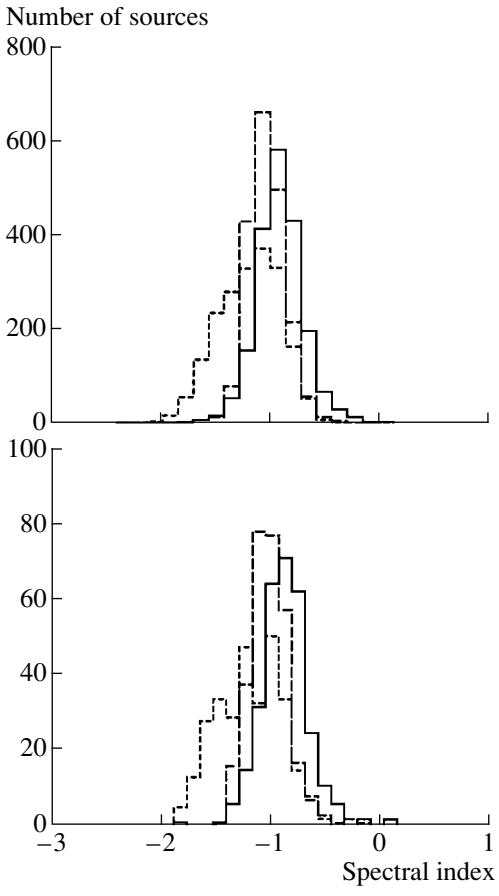

Fig. 2. Distribution of spectral indices of the identified sources at 80 MHz (dotted), 365 MHz (dashed), and 1400 MHz (solid) for 2006 sources with $|b| > 10°$ (upper) and for 301 sources near the Galactic plane ($|b| \le 10°$) (lower). The spectral index α is defined via $s = \nu^{\alpha}$.

Table 3. Statistics of the spectra of the decameter sources

Spectral class	Fitted curve	Number	%
Linear spectrum	$+A + BX$	898	39
Convex (C^+)	$+A \pm BX - CX^2$	184	8
Concave (C^-)	$+A - BX + CX^2$	1147	50
	$\pm A \pm BX + C\exp(-X)$	77	3

firm identifications for GR 0520−08, GR 0537−00, GR 0629+02, and GR 2345+03, as noted in the given list (there is only one point from another catalog, with a large offset from the center of gravity of the UTR map).

When compiling the final list of UTR objects, we used, in addition to the published UTR catalog [1–5], the data of a later electronic version (http://www.ira.kharkov.ua/UTR2/). As a result, in the final catalog, we identified 64 sources from the electronic version that were missing from the printed version, as well as four sources from the published lists that were missing from the electronic version. Furthermore, we reduced identified sources having different names in different lists to a single name, in accordance with the early version of the catalog.

4. THE STATISTICS OF THE RADIO SOURCES

The behavior of the source spectra at decameter wavelengths has already been studied by Sokolov [36], who used the UTR data but neglected the effect of blending; i.e., he assumed that each UTR source was identified with a single object. Our study uses the results of multiple identifications. We obtained distributions of the spectral indices of the identified UTR objects based on the curves used to approximate their spectra. We can see from the distribution of spectral indices at 80, 365, and 1400 MHz (Fig. 2) that the fraction of steeper spectra increases toward lower frequencies. This could be a consequence of two effects: blending unresolved sources in the decameter range and the fact that the UTR, which operates at low frequencies with low angular resolution, is more sensitive to extended regions of radio galaxies ("lobes"), which have steeper spectra than the sources as a whole [37]. The distribution of spectra for 2154 sources, including blended sources, is presented in Table 3. We found no identifications for three sources. Of the identified sources, 341 are blends of two or more components.

Of the 546 UTR sources that were identified with FIRST objects within a 60″ search circle, 374 (68%)

have a multicomponent structure; i.e., there are several FIRST sources in the search window. This, of course, suggests the following two effects. First, in this type of classification, some of the multicomponent objects will include physically unassociated sources. Second, the remaining single-component objects include some extended FIRST sources with sizes larger than the telescope beam (i.e., $> 5''$). Nevertheless, this approach enables us to distinguish and/or classify objects with composite structures at an early stage.

We used the list of UTR sources with improved positions for cross-identification within a $10''$ radius with the PGC [38] optical and mixed catalogs of AGN, the catalog of Dixon [39], and other catalogs of the CATS database. As a result, we obtained identifications for 575 different UTR sources, which can be found in Catalog 1. This list is based solely on the CATS information and was not "filtered" through NED or SIMBAD. We plan to refine our identifications using these databases. The resulting list represents 32% of the entire UTR catalog, as opposed to the 19% of the object identifications that were published in the original papers.

For a small number of objects, especially very extended sources near the Galactic plane, such as supernova remnants or HII regions, catalogs of discrete objects have natural limitations, and the estimated positions can be incorrect. One example is GR 1901+05, which corresponds to the very extended supernova remnant 3C 396. For such objects, we should expand the radius of the optical identification window and study the radio emission on larger scales, for instance, using single-dish maps, to ensure a valid optical identification.

Virtually all the objects identified with optical catalogs are contained in the AGN list [40]. Several sources were identified with objects of the PGC catalog of bright galaxies [38]. For unidentified objects, we used the APM system [24] to search for possible existing identifications.

We have also performed cross-identifications with ROSAT X-ray and IRAS infrared objects. In the X-ray, we searched for emission in $90''$ windows around the source positions in the 1WGA [41], EIN2S [42], EMSS [43, 44], RGN [45], and ROSAT [46] catalogs. X-ray emission was found for 146 candidates, mostly identified with active galactic nuclei.

In the infrared, we searched for identifications in the HII_H [47], HII_I [48], IFSC [49], IPSC [50], IRSSS [51], and ISSC [52] catalogs. Given the position errors for the IR sources, which are considerably larger than that in the optical range, we chose a window with a radius of $60''$ for the radio–IR identifications. We found 39 candidates for identifications with UTR objects. Some are associated with HII regions and some with active galactic nuclei. We have three fairly firm identifications of UTR sources with HII regions: GR 0238+58, GR 0704−12, and GR 1901+05. The presence of decameter sources in HII regions, which usually have a low-frequency cutoff due to the effects of propagation in the interstellar plasma (more specifically, because of the thermal absorption in the interstellar medium), may be due to the contrast against the nonthermal Galactic background radiation at the boundaries of the regions. This was found, for example, by Caswell [53] in 1976 as a depression (dip in the background) of the 10 MHz emission in a survey of the Northern sky using the Penticton telescope. However, Taylor *et al.* [54] have shown that a small fraction of sources at 327 MHz are associated with HII regions that have negative spectral indices; for several, α is even < -1. Although Taylor *et al.* [54] do not discuss the origin of such steep spectra, a superposition of various objects is also possible. In our case, judging from the shape of the radio spectra, a decameter "source" is detected in an HII region against the Galactic background only in the case of GR 1901+05. This cannot be asserted for the other two HII regions with confidence.

The lists of X-ray and infrared identifications are also accessible at the Catalog 1 address.

5. SOURCES WITH ULTRASTEEP SPECTRA

Radio sources with steep spectra are being actively studied by several groups [55–57], primarily because they include a large fraction of objects identified with distant radio galaxies, which can be used to study the early Universe and as tracers of protoclusters [58]. An important feature of the studied catalog is the presence of decameter points in the source spectra, which is a useful supplement to studied lists of steep-spectrum sources [59].

We can see from the distribution of spectral indices (Fig. 2) that a rather large fraction of the objects have steep spectra at all three frequencies. To compile a list of candidate distant objects, we made a selection [60] for spectral indices $\alpha \leq -1.2$, linear (S type) spectra, and extended structure in the FIRST catalog.

Of all the 2314 catalog sources that have radio identifications, 422 S-type sources have very steep spectra ($\alpha \leq -1.0$); for this work, we selected a subsample of 102 objects with ultrasteep spectra (USS, $\alpha \leq -1.2$). In this subsample, we found 30 FIRST sources for 23 UTR objects, which are listed in Table 4. The first column contains the names of the UTR sources and their blends, labeled ID2 and ID3, as in the main list of radio identifications of Catalog 1.

Among the listed FIRST sources, only one [GR 1527+51 (ID2)] is unresolved and appears

Table 4. 43 FIRST components for 23 USS sources ($\alpha \leq -1.2$) from the UTR catalog. (The table lists the object name, composite source size (or single-component size after deconvolution) from the NVSS and FIRST surveys, FIRST RA and DEC, major and minor axes after deconvolution, and the FIRST position angle (degrees from north to east).)

UTR (B1950)	α	NVSS Size	FIRST Size	RA Dec (J2000)	S_p, mJy	S_i, mJy	Major axis	Minor axis	PA
GR0002+00(ID2)	−1.52	16″	7.4″	000650.56+003648.4	47.6	75.9	7.4″	1.1″	154°
GR0135−08	−1.34	28	20	013714.87−091155.4	5.2	44.3	30.8	7.5	98
				013715.08−091203.3	10.2	36.9	15.6	4.3	90
				013715.45−091155.8	8.2	25.7	13.0	5.4	148
				013716.22−091149.5	10.0	39.3	11.3	9.3	119
GR0257−08	−1.20	<18	4.5	025919.15−074501.2	162.5	211.9	4.5	1.3	59
GR0257−08(ID2)	−1.23	80	83	030040.22−075302.2	18.4	52.8	15.6	3.0	174
				030040.56−075259.6	10.1	122.8	30.7	13.1	163
				030042.99−075413.8	7.0	34.2	16.2	8.4	32
				030042.99−075358.0	13.6	47.8	12.3	7.4	152
				030043.60−075418.3	6.4	22.0	11.2	7.6	75
				030043.75−075407.2	6.6	22.4	15.6	4.8	170
GR0723+48(ID2)	−1.26	47	3.1	072651.18+474041.5	23.8	29.1	3.1	2.0	175
				072655.00+474051.0	51.8	75.7	5.6	1.1	85
GR0818+18	−1.28	24	22	082032.48+192731.3	31.1	49.2	6.1	1.7	174
				082032.73+192709.0	76.4	98.5	3.9	1.6	8
GR0858−02(ID2)	−1.54	70	55	085935.06−015842.1	11.7	27.2	10.2	3.2	122
				085936.10−015851.8	9.8	15.9	6.2	2.8	128
				085938.21−015908.1	20.2	43.6	8.1	4.5	133
GR0910+48	−1.22	36	29	091359.00+482738.0	26.9	88.6	11.6	5.2	100
				091401.83+482729.2	39.6	110.2	10.9	3.9	106
GR0922+42(ID2)	−1.21	<19	2.7	092559.66+420335.3	199.7	244.1	2.7	2.4	98
GR0942+54	−1.24	14	8	094618.12+543003.8	51.1	57.1	2.5	0.9	36
				094618.53+543010.1	75.3	80.6	1.7	1.1	16
GR1149+42	−1.24	<17	5.0	115213.58+415344.9	83.7	115.4	5.0	1.0	18
GR1214−03	−1.26	70?	3.2	121755.30−033722.0	176.9	208.9	3.2	1.2	111
GR1223−00	−1.79	25	25	122722.97−000813.8	5.8	13.6	8.4	5.0	100
				122724.54−000821.1	8.4	16.9	7.1	4.6	116
GR1243+04	−1.25	<18	6.8	124538.38+032320.1	249.4	379.9	6.8	1.3	158
GR1318+54		25	23	132202.81+545758.1	30.3	90.3	9.5	5.9	82
				132205.33+545805.3	8.6	35.9	10.7	8.6	55
GR1320+43	−1.32	<19	3.3	132232.32+425726.5	129.3	154.6	3.3	1.0	81
GR1355+01(ID3)	−1.26	<19	10	135821.64+011442.0	77.0	88.4	2.9	1.4	42
				135822.08+011449.4	169.9	180.9	1.6	1.3	32
GR1447+57	−1.26	<19	4.5	144630.04+565146.8	75.2	99.2	4.5	0.7	148
GR1527+51(ID2)	−1.22	<19	1.4	152828.36+513401.4	203.9	212.8	< 2.	< 2.	140
GR1539+53(ID2)	−1.24	<18	6.4	154144.69+525054.5	87.0	136.7	6.4	0.8	66
GR1613+49	−1.24	<19	3.0	161631.16+491908.2	56.1	66.2	3.0	1.3	10
GR1731+43	−1.56	42	40	173333.87+434318.6	32.9	57.9	6.3	3.0	164
				173334.26+434300.8	22.8	27.3	3.1	1.5	173
				173334.41+434251.4	12.3	15.8	3.3	2.4	159
				173334.58+434239.8	27.3	51.0	7.5	2.3	150
GR2211−08(ID2)	−1.39	<19	8.6	221519.65−090005.8	75.2	125.0	8.6	1.4	176

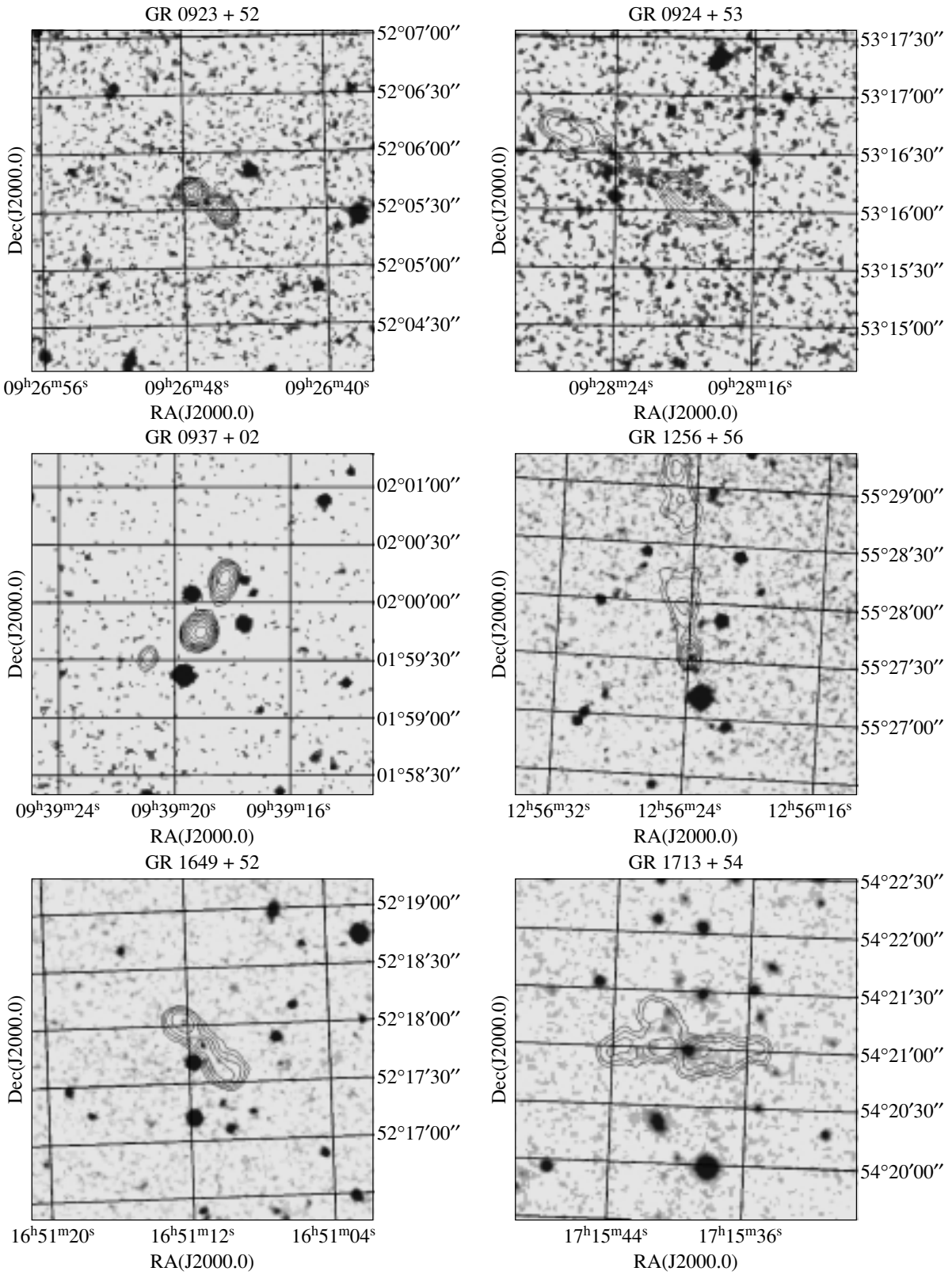

Fig. 3. FIRST 1.5-GHz radio maps (contours) of some UTR objects overlaid on the Digitized optical Sky Survey (gray scale).

Table 5. Samples from the UTR and VLA catalogs: minimum, median, and maximum flux densities (mJy) according to the spectral-index rank. (N is the number of the objects.)

α range	FIRST				NVSS			
	N	min	med	max	N	min	med	max
$-0.9\ldots-1.0$	88	1.2	514	1710	183	4.2	574	3902
$-1.0\ldots-1.1$	93	3.6	363	875	168	5.7	365	1322
<-1.1	75	29	193	650	185	3.3	212	796

Table 6. Samples from the UTR and VLA catalogs: minimum, median, and maximum object sizes (arcsec) according to the spectral-index range

α range	FIRST			NVSS		
	min	med	max	min	med	max
$-0.9\ldots-1.0$	0.7	26	133	<13	24	127
$-1.0\ldots-1.1$	1.0	19	139	<15	22	130
<-1.1	2.9	12	122	<14	17	127

pointlike to the FIRST $\sim 5''$ beam (i.e., it has major and minor axes $< 2''$), while the remaining objects have multicomponent or extended structures. We also checked the structures of objects observed with lower resolution at the same frequency (1.4 GHz) in the NVSS survey [23]. We confirmed that the more complex the source, the higher the NVSS/FIRST flux-density ratio.

Among the objects of Table 4, we found three identifications in the NED database. The composite source GR 0135−08 is associated with the galaxy MCG-02-05-020, which has a redshift $z = 0.041$. The source GR 1214−03 is a LCRS quasar at $z = 0.184$, and GR 1243+04 is a radio galaxy (4C+03.24) at $z = 3.57$. We are continuing our analysis of the images of the objects using the Digital Sky Survey (DSS2), available on the web page of the Space Telescope Science Institute (http://archive.stsci.edu/dss/).

6. STATISTICAL ANALYSIS OF VLA MAPS OF DECAMETER SOURCES

We obtained identifications with NVSS objects [23] for the majority of the UTR sources (97%, in total 2253 identifications), and we searched for identifications in the FIRST survey [33] for all the UTR objects with $\delta > 28°$ (1143 objects). Among the FIRST and NVSS sources in $60''$ identification areas around the positions of the decameter sources, 552 NVSS sources (beamwidth $45''$) and 988 FIRST sources (beamwidth $5''$) were resolved into components.

For selected objects, we studied the dependence of the NVSS and FIRST maps on the morphological properties of the radio spectra. We selected sources with linear spectra and divided them into three groups according to their spectral indices: (1) $-0.9 > \alpha > -1.0$, (2) $-1.0 > \alpha > -1.1$, and (3) $\alpha < -1.1$ ($S \propto \nu^{\alpha}$). We selected NVSS objects outside the Galactic plane ($|b| > 15°$), while $|b|$ is always $> 20°$ for the FIRST sources. We selected 536 NVSS sources and 256 FIRST sources, for which we determined the minimum, median, and maximum values of the flux and source size as functions of the spectral index. The parameters of the samples are listed in Tables 5 and 6, which contain the corresponding values for the NVSS and FIRST catalogs. The rows list the various parameters for the specified spectral-index intervals, while the columns give the value of each parameter.

The upper and lower limits in both tables are determined only by selection effects. An interesting fact is that the median source size decreases with decreasing spectral index α ($S \propto \nu^{\alpha}$) but remains in the range $10''$–$30''$. In spite of this, we found no correlation between spectral index and source size for the complete FIRST and NVSS subsamples. The lack of correlation in the complete subsamples is due to the relatively wide scatter of the values, which create a "cloud of points" in the coordinate plane. The median value $m_{1/2}$ demonstrates that points fall into intervals with values greater or smaller than $m_{1/2}$ with equal probability. The spectral-index dependence of this quantity indicates variations in this boundary and may, in principle, suggest some relationship; however, based on our analysis of the distributions for the entire subsample, we treat this possibility cautiously.

Figure 3 presents maps of some objects possessing interesting morphological features. The maps are based on the FIRST data and are superposed on the DSS2 optical images. Below we give comments for each source.

GR 0923+52. Double radio source. An arc emanating from the identified galaxy is visible in the optical image.

GR 0924+53. Double radio source in a group of galaxies.

GR 0937+02. Three-component source or independent objects in a group of galaxies.

GR 1256+56. Multicomponent source (double jet?) in a group of galaxies.

GR 1649+52. Composite (three-component?) source. An arc is visible in the image of the optical candidate.

GR 1713+54. A multicomponent source in a group of galaxies that are probably merging. The axis of the optical emission is aligned with the radio axis.

7. CONCLUSION

Our iterative method for obtaining radio identifications and cross identifications with data from an existing decameter catalog operates effectively as a first step toward the optical identification of radio sources from catalogs obtained with a broad beam.

We have obtained a catalog of 2316 radio sources corresponding to 1822 UTR objects. It follows that at least 395 UTR sources have more than one identified object that contributes significantly to the decameter flux. We obtained radio identifications at frequencies higher than the decameter frequencies for all but three of the UTR sources. This fraction of radio-identified UTR sources is much greater than the 93% quoted in the original UTR catalogs or the 83% quoted in the more recent electronic version.

Using cross-identifications with optical catalogs, we have increased the number of optical identifications from the 19% in the original UTR publications to 32%.

We have also found probable identifications of UTR sources in the infrared and X-ray ranges, and constructed a subsample of 38 ultrasteep-spectrum sources ($\alpha \leq -1.2$) for which associations with FIRST objects are available.

The median source size for the steep-spectrum objects ($\alpha < -0.9$) decreases with decreasing spectral index α but remains in the range $10''$–$30''$. No spectral index–source size correlation has been found.

ACKNOWLEDGMENTS

The authors are grateful to A.P. Miroshnichenko and D. Krivitskiĭ (Institute of Radio Astronomy, Kharkov, Ukraine) for providing their data and useful discussions; to S.A. Trushkin, V.N. Chernenkov (Special Astrophysical Observatory, Russian Academy of Sciences), their coauthors in the creation of the CATS database, for useful discussions on identification problems; and also to R.D. Dagkesamanskiĭ for valuable comments, which have allowed us to improve the article. This work was partially supported by the Russian Foundation for Basic Research (project no. 02-07-90038). H.A. thanks CONACyT for financial support (grant 27602-E). When identifying radio sources, we used the Digital Sky Survey of the Space Telescope Science Institute, based on photographic data from the Oschin Schmidt Telescope (Mt. Palomar) and the Schmidt Telescope (Great Britain). This research also used the NASA/IPAC Extragalactic Database (NED), created and supported at the Jet Propulsion Laboratory (California Institute of Technology, USA) under contract with the National Aeronautics and Space Administration.

REFERENCES

1. S. Ya. Braude, A. V. Megn, S. L. Rashkovski, *et al.*, Astrophys. Space Sci. **54**, 37 (1978).
2. S. Ya. Braude, A. V. Megn, K. P. Sokolov, *et al.*, Astrophys. Space Sci. **64**, 73 (1979).
3. S. Ya. Braude, A. P. Miroshnichenko, K. P. Sokolov, and N. K. Sharykin, Astrophys. Space Sci. **74**, 409 (1981).
4. S. Ya. Braude, N. K. Sharykin, K. P. Sokolov, and S. M. Zakharenko, Astrophys. Space Sci. **111**, 1 (1985).
5. S. Ya. Braude, K. P. Sokolov, and S. M. Zakharenko, Astrophys. Space Sci. **213**, 1 (1994).
6. S. Ya. Braude and A. V. Men', Radiofiz. Radioastron. **1**, 9 (1996).
7. O. V. Verkhodanov, S. A. Trushkin, H. Andernach, and V. N. Chernenkov, in *Astronomical Data Analysis Software and Systems VI,* Ed. by G. Hunt and H. E. Payne, Astron. Soc. Pac. Conf. Ser. **125**, 322 (1997); http://cats.sao.ru.
8. O. V. Verkhodanov, H. Andernach, and N. V. Verkhodanova, in *Problems of Modern Radio Astronomy: Proceedings of the XXVII Radio Astronomical Conference, Inst. of Applied Astronomy, Russian Academy of Sciences, St. Petersburg, 1997,* Vol. 1, p. 330.
9. S. E. G. Hales, J. E. Baldwin, and P. J. Warner, Mon. Not. R. Astron. Soc. **234**, 919 (1988).
10. S. E. G. Hales, C. R. Masson, P. J. Warner, and J. E. Baldwin, Mon. Not. R. Astron. Soc. **246**, 256 (1990).
11. M. M. McGilchrist, J. E. Baldwin, J. M. Riley, *et al.*, Mon. Not. R. Astron. Soc. **246**, 110 (1990).
12. X. Zhang, Y. Zheng, H. Chen, *et al.*, Astron. Astrophys., Suppl. Ser. **121**, 59 (1997).
13. R. B. Rengelink, Y. Tang, A. G. de Bruyn, *et al.*, Astron. Astrophys., Suppl. Ser. **124**, 259 (1997).
14. J. N. Douglas, F. N. Bash, F. A. Bozyan, *et al.*, Astron. J. **111**, 1945 (1996).
15. A. Ficarra, G. Grueff, and G. Tomassetti, Astron. Astrophys., Suppl. Ser. **59**, 255 (1985).
16. R. L. White and R. H. Becker, Astrophys. J., Suppl. Ser. **79**, 331 (1992).
17. P. C. Gregory and J. J. Condon, Astrophys. J., Suppl. Ser. **75**, 1011 (1991).
18. P. C. Gregory, W. K. Scott, K. Douglas, and J. J. Condon, Astrophys. J., Suppl. Ser. **103**, 427 (1996).
19. A. E. Wright, N. Tasker, D. McConnell, *et al.*, Astrophys. J., Suppl. Ser. **103**, 145 (1996).
20. R. S. Dixon, Astrophys. J., Suppl. Ser. **20**, 1 (1970).
21. R. S. Dixon, Master List of Radio Sources, Version 43 (with corrections by H. Andernach, 15/Nov/98) (1981).

22. O. V. Verkhodanov, in *Problems of Modern Radio Astronomy: Proceedings of the XXVII Radio Astronomical Conference, Inst. of Applied Astronomy, Russian Academy of Sciences, St. Petersburg, 1997,* Vol. 1, p. 322.
23. J. J. Condon, W. D. Cotton, E. W. Greisen, *et al.*, Astron. J. **115**, 1693 (1998).
24. Irwin Mike, Catalogue of Automated Plate Measuring Machine (1998); http://www.ast.cam.ac.uk/ apmcat/.
25. D. O. Edge, J. R. Shakeshaft, W. B. McAdam, *et al.*, Mon. Not. R. Astron. Soc. **68**, 37 (1959).
26. A. S. Bennett, Mem. R. Astron. Soc. **68**, 163 (1961).
27. J. D. H. Pilkington and P. F. Scott, Mem. R. Astron. Soc. **69**, 183 (1965).
28. M. R. Viner and W. C. Erickson, Astron. J. **80**, 931 (1975).
29. P. J. S. Williams, S. Kenderdine, and J. E. Baldwin, Mem. R. Astron. Soc. **70**, 53 (1966).
30. B. Y. Mills, O. B. Slee, and E. R. Hill, Aust. J. Phys. **11**, 360 (1958).
31. B. Y. Mills, O. B. Slee, and E. R. Hill, Aust. J. Phys. **13**, 676 (1960).
32. B. Y. Mills, O. B. Slee, and E. R. Hill, Aust. J. Phys. **14**, 497 (1961).
33. R. L. White, R. H. Becker, D. J. Helfand, and M. D. Gregg, Astrophys. J. **475**, 479 (1997).
34. O. V. Verkhodanov, H. Andernach, and N. V. Verkhodanova, Bull. SAO, No. 49, 53 (2000); astro-ph/0008431.
35. R. E. Otrupcek and A. E. Wright, Proc. Astron. Soc. Aust. **9**, 170 (1990); Bull. Inf. CDS, **41**, 47.
36. K. R. Sokolov, Radiofiz. Radioastron. **1**, 42 (1996).
37. G. K. Miley, Ann. Rev. Astron. Astrophys. **18**, 165 (1980).
38. G. Paturel, P. Fouqué, L. Bottinelli, and L. Gouguenheim, Astron. Astrophys., Suppl. Ser. **80**, 299 (1989).
39. R. S. Dixon and G. Sonneborn, *A Master List of Nonstellar Optical Astronomical Objects* (Ohio State University Press, 1980).
40. M.-P. Véron-Cetty and P. Véron, Astron. Astrophys. **374**, 92 (2001).
41. N. E. White, P. Giommi, and L. Angelini, Bull. AAS **26**, 1372 (1994).
42. E. C. Moran, D. J. Helfand, R. H. Becker, and R. L. White, Astrophys. J. **461**, 127 (1996).
43. I. M. Gioia, T. Maccacaro, R. E. Schild, and A. Wolter, Astrophys. J., Suppl. Ser. **72**, 567 (1990).
44. J. T. Stocke, S. L. Morris, I. M. Gioia, *et al.*, Astrophys. J., Suppl. Ser. **76**, 813 (1991).
45. M. Neumann, W. Reich, E. Fürst, *et al.*, Astron. Astrophys., Suppl. Ser. **106**, 303 (1994).
46. W. Voges, R. Gruber, F. Haberl, *et al.*, *The First ROSAT Source Catalog (ROSAT SRC)* (Max-Planck-Institut für Physik und Astrophysik, Institut für extraterrestrische Physik, Garching, Germany, 1994); http://ftp.rosat.mpe-garching.mpg.de/archive/sourcecat.
47. V. A. Hughes and G. C. Macleod, Astron. J. **97**, 786 (1989).
48. C. Codella, M. Felli, and V. Natale, Astron. Astrophys. **284**, 233 (1994).
49. M. Moshir, *IRAS Faint Source Survey, Explanatory Supplement. Version 1 and Tape,* Ed. by M. Moshir (IPAC, CIT, Pasadena, 1989).
50. IRAS Group, *IRAS Point source catalogue; Catalogs and Atlases, Explanatory Supplement* (Joint IRAS Science Working Group, 1987).
51. G. Helou and D. W. Walker, *IRAS Small Scale Structure Catalog* (Jet Propulsion Laboratory, 1985).
52. S. G. Kleinmann, R. M. Cutri, E. T. Young, F. J. Low, and F. C. Gillett, *IRAS Serendipitous Survey Catalogue, Explanatory Supplement* (1986).
53. J. L. Caswell, Mon. Not. R. Astron. Soc. **177**, 601 (1976).
54. A. R. Taylor, W. M. Goss, P. H. Coleman, *et al.*, Astrophys. J., Suppl. Ser. **107**, 239 (1996).
55. Yu. N. Parijskij, W. M. Goss, A. I. Kopylov, *et al.*, Bull. SAO **40**, 5 (1996).
56. H. J. A. Röttgering, R. van Ojik, G. K. Miley, *et al.*, Astron. Astrophys. **326**, 505 (1997).
57. P. J. McCarthy, G. K. Miley, S. De Koff, *et al.*, Astrophys. J., Suppl. Ser. **112**, 415 (1997).
58. S. Djorgovski, in *Nearly Normal Galaxies,* Ed. by S. Faber (Springer-Verlag, 1987), p. 290.
59. C. De Breuck, W. van Breugel, H. J. A. Röttgering, and G. Miley, Astron. Astrophys., Suppl. Ser. **143**, 303 (2000).
60. H. Andernach, O. V. Verkhodanov, and N. V. Verkhodanova, in *IAU Symp. 199: Universe at Low Radio Frequencies,* p. 217 (2002), astro-ph/0001473.

Translated by G. Rudnitskiĭ

Astronomy Reports, Vol. 47, No. 2, 2003, pp. 119–128. Translated from Astronomicheskiĭ Zhurnal, Vol. 80, No. 2, 2003, pp. 140–150.

Objects from a Cross-Identification of the IRAS and Low-Frequency Texas Radio Catalogs

O. V. Verkhodanov[1], V. H. Chavushyan[2], Raul Mújica[2], S. A. Trushkin[1], and José R. Valdés[2]

[1] *Special Astrophysical Observatory, Russian Academy of Sciences, Nizhniĭ Arkhyz, Karachaĭ-Cherkessian Republic, 357147 Russia*

[2] *Instituto Nacional de Astrofísica, Óptica y Electrónica, Puebla, México*

Received April 26, 2002; in final form, June 26, 2002

Abstract—A cross-identification of objects in the low-frequency (365 MHz) Texas radio catalog and in IRAS catalogs at four infrared wavelengths has yielded a list of 715 objects for further studies. Objects with steep spectra for which the difference in the centers of gravity of the radio and infrared sources was less than 3″ were selected from this list. Seventeen of the objects have been observed at six wavelengths using the RATAN-600 radio telescope. Spectra of nine objects from the initial list for which there were candidate optical counterparts were obtained using the 2.1-m telescope of the INAOE. The results of these observations are discussed. The presence of steep spectral indices for the radio sources is confirmed. The possible optical counterparts include interacting galaxies, an infrared galaxy, two emission-line galaxies, and a candidate BL Lac object. Optical images of the optical counterparts are presented together with radio and optical spectra. © *2003 MAIK "Nauka/Interperiodica"*.

1. INTRODUCTION

The sifting of radio catalogs using other catalogs—cross identification—can aid in detecting unusual objects. Using the CATS database [1], which includes more than 300 catalogs, and specially developed search procedures, Trushkin and Verkhodanov [2] carried out cross-identifications between three catalogs of infrared sources (PSC [3], FSC [4], and SSC [5]) derived from the IRAS all-sky survey [6] and a radio catalog based on the Texas sky survey at 365 MHz [7].

The goal of this work was to identify and investigate both Galactic and extragalactic objects near IRAS sources, particularly those with low-frequency radio emission. This could help distinguish infrared objects with steep radio spectra, active galactic nuclei (AGN), and active Galactic objects. In addition, the inclusion in the CATS database of a large number of catalogs in various wavelength ranges could facilitate more detailed studies of the properties of sources in the derived sample.

The resulting catalog of radio sources with PSC, FSC, and SSC identifications contains 715 objects [8]. This catalog was obtained using an identification window with a radius of 60″ and includes all objects falling within this region taking into account the coordinate errors, which somewhat increase the distance between the centers of gravity at the different wavelengths.

We constructed two samples [9] from the total list for the investigations considered here: (1) objects for which the positions of the infrared and radio centers of gravity did not exceed 3″ (and the likelihood ratio for the identification exceeds unity [10]) and the radio spectral index calculated using data in the CATS database was steeper than -0.85 ($S \sim \nu^{\alpha}$); and (2) objects for which the radio source had a possible counterpart on the Palomar Digital Sky Survey (DSS2).

2. RADIO DATA

We carried out radio studies of the first sample at the Special Astrophysical Observatory. The list of objects and number of observations of each are presented in Table 1. The radio observations were carried out on November 7–14, 1999, on the northern sector of the RATAN-600 telescope. Continuum radiometers of the first feed at wavelengths of 1.38, 2.7, 3.9, 7.6, 13, and 31 cm were used. The tie to the absolute flux scale [11] was performed using observations of the sources PKS 0023−263, PKS 1245−197, 3CR 286, PKS 1345+125, and NGC7027. The data reduction was carried out in the FADPS [12] system and included a procedure for eliminating low-frequency interference (the background component), averaging, and a Gaussian analysis. In spite of the fact that the situation with regard to interference at decimeter wavelengths has sharply worsened compared to previous years, it was nevertheless possible

1063-7729/03/4702-0119$24.00

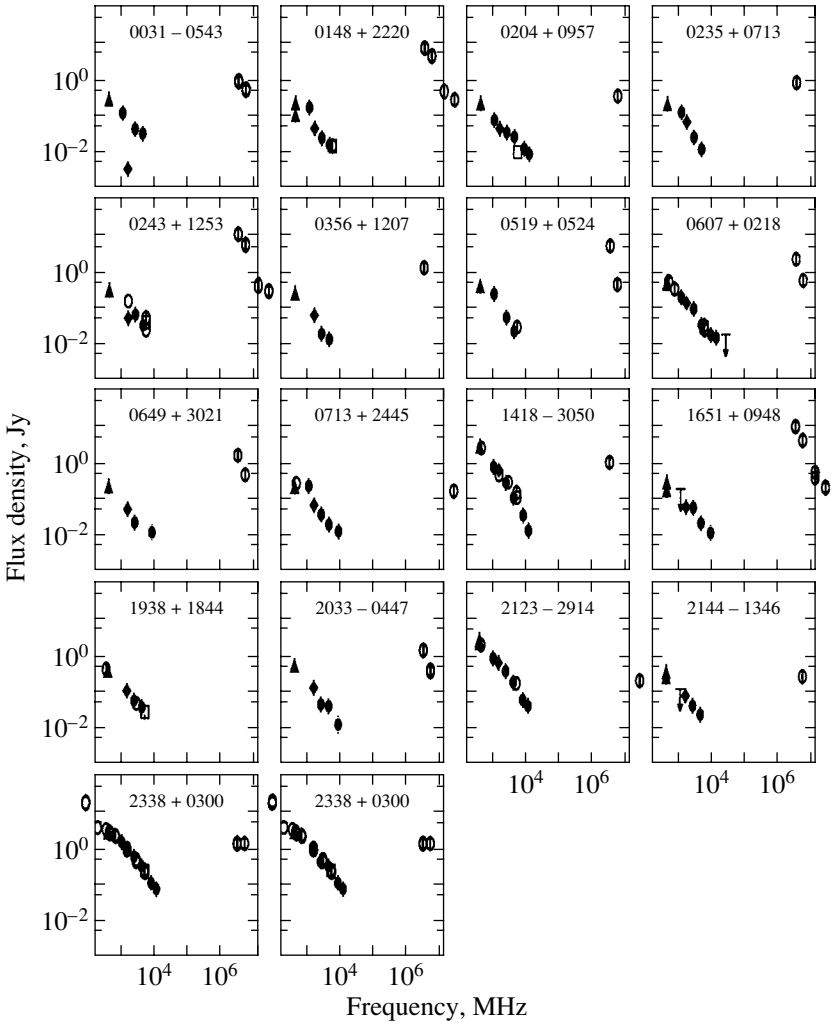

Fig. 1. Radio and infrared spectra of some objects from the IRAS–Texas cross-identification list based on RATAN-600 data and additional radio data from the CATS database. The filled circles show the RATAN-600 data.

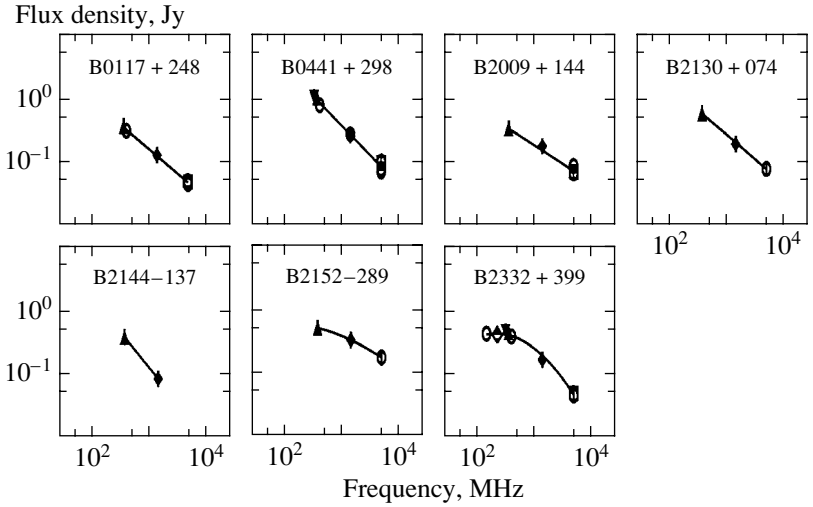

Fig. 2. Radio spectra of some objects from the IRAS–Texas cross identification for which there are candidate DSS2 optical counterparts. The spectra were constructed using data from the CATS database.

Table 1. Objects with steep spectra observed on RATAN-600

TXS name	IRAS name	RA (2000.0)	Dec (2000.0)	N
B0031−057	F00318−0543	00 34 25.766	−05 26 53.77	8
B0148+223	F01484+2220	01 51 14.821	+22 34 54.79	11
B0204+099	F02044+0957	02 07 06.321	+10 11 47.77	11
B0235+072	02358+0712	02 38 29.889	+07 26 25.73	8
B0243+128	F02435+1253	02 46 16.329	+13 05 46.59	3
B0356+121	03561+1207	03 58 51.236	+12 15 56.82	11
B0519−056	05192−0524	05 21 41.988	−05 21 44.47	12
B0607+022	06074+0218	06 09 58.997	+02 17 27.44	12
B0649−303	06492−3021	06 51 09.708	−30 24 51.50	12
B0713+247	F07130+2445	07 16 05.856	+24 40 08.33	12
B1418−308	14189−3050	14 21 55.515	−31 04 26.85	11
B1651−098	F16516−0948	16 54 24.545	−09 53 19.98	11
B1938+187	19384+1843	19 40 45.127	+18 51 04.56	2
B2033−047	F20337−0447	20 36 23.558	−04 37 16.16	5
B2123−292	F21237−2913	21 26 40.102	−29 01 06.00	11
B2144−137	F21443−1346	21 47 04.600	−13 32 11.65	11
B2338+030	F23389+0300	23 41 30.353	+03 17 26.65	10

to derive flux densities in this range for a number of sources. The results of the RATAN-600 observations are summarized in Table 2.

We constructed the spectra of 17 objects (Fig. 1) using our radio observations and CATS data. We derived spectral indices by approximating the spectra using straight lines of the form $y = A + \alpha x$, where x is the logarithm of the frequency in MHz, y is the flux density in Jy, α is the spectral index, and A is a constant. The results of this analysis showed that the source TXS B0031−057 has a flatter spectra than was previously thought (previous value: $\alpha = -3.3$, new value: $\alpha = -0.95$), while the spectral indices for the other sources studied did not change appreciably. The NVSS flux density used to construct the initial spectrum for B0031−057 based on two measurements from the Texas (365 MHz) and NVSS (1400 MHz) catalogs was apparently underestimated. The new spectral indices are presented in Table 2.

3. OPTICAL OBSERVATIONS

We selected for optical studies those objects with IRAS−Texas identification radii not exceeding 3″ with probable optical counterparts in the Palomar atlas brighter than 19^m on the E plate. In all, nine objects fulfilled these criteria, three of which (B0031−057, B0204+099, and B2144−137) have steep spectra and also fell into the first subsample. The list of objects with candidate optical counterparts are presented in Table 3. This table presents the coordinates of the radio sources and candidate optical counterparts, together with additional optical objects

Table 2. RATAN-600 flux densities and spectral indices α for some objects derived from RATAN-600 and CATS radio data

Name of radio source	S(1.38 cm), mJy	S(2.7 cm), mJy	S(3.9 cm), mJy	S(7.6 cm), mJy	S(13 cm), mJy	S(31 cm), mJy	α
B0031−057	<35	< 110	< 25	54 ± 9	72 ± 17	202 ± 64	−0.95
B0148+223	<23	< 20	< 15	27 ± 4	41 ± 11	289 ± 60	−1.02
B0204+099	<31	< 24	29 ± 6	25 ± 4	32 ± 12	133 ± 36	−0.94
B0235+072	<32	< 24	< 19	21 ± 5	45 ± 15	224 ± 47	−1.11
B0243+128	<45	< 27	< 30	46 ± 7	92 ± 23	< 180	−0.80
B0356+121	<31	< 12	< 15	19 ± 3	27 ± 11	< 250	−1.24
B0519−056	<35	< 40	< 18	32 ± 7	78 ± 13	351 ± 31	−1.16
B0607+022	<27	22 ± 6	26 ± 6	50 ± 4	139 ± 12	293 ± 44	−1.16
B0649−303	<26	< 17	14 ± 8	<40	13 ± 13	< 160	−1.06
B0713+247	<24	< 8	15 ± 5	23 ± 3	44 ± 09	262 ± 49	−1.09
B1418−308	<38	< 21	42 ± 9	127 ± 6	327 ± 16	916 ± 34	−1.27
B1651−098	<35	31 ± 11	14 ± 8	26 ± 7	70 ± 14	227 ± 45	−0.96
B1938+187	<50	< 31	< 27	39 ± 8	60 ± 25	< 300	−1.03
B2033−047	<56	< 44	13 ± 10	42 ± 8	47 ± 22	< 220	−1.13
B2123−292	<33	43 ± 8	63 ± 8	195 ± 6	397 ± 16	910 ± 34	−1.14
B2144−137	<35	< 22	< 19 ± 7	25 ± 6	44 ± 14	129 ± 38	−1.07
B2338+030	<27	66 ± 7	99 ± 7	286 ± 5	525 ± 14	1349 ± 49	−1.01

near the radio sources. The optical coordinates were taken from the DSS2 survey or the USNO-2 catalog. Figure 2 presents the spectra of the radio sources of this subsample for which spectra are not presented in Fig. 1.

We present maps of the optical counterparts from the Digital Sky Survey (DSS2) in Fig. 3. Figure 4 shows enlarged images of the complex objects TXS B0031−057, TXS B0117+248, TXS B0204+099, and TXS B2130−074.

We obtained optical spectral observations in October–November 1999 on the 2.1-m telescope of the INAOE Guillermo Haro Observatory in Cananea, Mexico. The observations were carried out using the LFOSC (Faint Object Spectrograph and Camera) [13] at 4000—9000 Å with a resolution of 16 Å. The data reduction was carried out in the IRAF package, and included bias correction, flat-fielding, removal of cosmic rays, linearization of the wavelength scale, and flux calibration. Figure 5 shows the resulting optical spectra of these objects.

We present remarks about each object below. The source IRAS F02044+0957 (B0204+099) is discussed separately.

B 0031−057. The radio spectrum is steep, and is fit by the line $y = 2.128 - 0.951x$, where x is the logarithm of the frequency in MHz and y is the logarithm of the flux density in Jy. The DSS image of the candidate optical counterpart shows a lenticular galaxy for which the USNO-2 catalog gives $B = 17\overset{m}{.}0$ and $R = 15\overset{m}{.}6$. Hα emission is observed in the optical spectrum. The [SII] 6731/6717 lines are not

Table 3. List of objects with candidate optical counterparts

TXS name	IRAS name	TXS coordinates (RA/Dec (2000.0))	Object	Optical coordinates* (RA/Dec (2000.0))
B0031−057	F00318−0543	003425.77-052653.8		003424.96−052646.6 (USNO)
B0117+248	F01173+2448	012006.65+250417.6	A	012006.78+250416.5
			B	012006.36+250405.9
B0204+099	F02044+0957	020706.32+101147.8	A	020706.09+101147.4 (USNO)
			B	020706.24+101146.7 (USNO)
			C	020706.38+101133.5 (USNO)
			D	020706.67+101137.8 (USNO)
			E	020708.50+101117.9 (USNO)
B0441+298	04411+2951	044414.96+295716.3		044414.09+295705.8
B2009+144	20089+1427	201120.12+143653.8		201119.44+143649.5 (USNO)
B2130−074	F21309−0726	213333.26-071250.0		213333.33−071248.9
B2144−137	F21443−1346	214704.60-133211.6		214704.39−133210.6 (USNO)
B2152−289	F21527−2856	215537.88-284208.2	A	215538.10−284206.0
			B	
B2332+399	F23320+3957	233434.38+401324.2		233434.71+401327.2

* Coordinates taken from the USNO-2 catalog are marked.

Table 4. Logarithms of the observed and reddening-corrected ratios of emission-line intensities to the Hβ flux for optical objects near IRAS F02044+0957

Object	z	c(Hβ)	EW(Hβ), Å	[OIII] λ5007	[OI] λ6300	[NII] λ6583	[SII] $\lambda\lambda$(6717+6731)
A	0.093	1.377	19	0.26	−0.13	0.30	0.23
B	0.094	0.645	11	0.31	−	−0.30	−0.09
C	0.186	−	−	−	−	−	−
E	0.094	−	−	−	−	−	−

resolved. We find the redshift to be $z = 0.069$. The object is included in the NED database, which gives the redshift $z = 0.067$.

B0117+248. The radio spectrum is fit by the line $y = 1.531 - 0.776x$. We investigated two objects near the source (Table 3): A is a stellar object, while B is most likely an interacting galaxy (a system such as NGC 4038−NGC 4039 or VV 21). We obtained optical spectra for both these objects. Object A has the spectrum of a quasar with $z = 1.616$; lines of MgII with $l_0 = 2798$, $l_{\rm obs}$=7323 and C[III] with $l_0 = 1909$, $l_{\rm obs} = 4992$ were identified in the spectrum. Object B is an emission-line galaxy (ELG) with a redshift $z = 0.115$, based on Hα emission with $l_0 = 6563$, $l_{\rm obs} = 7320$ and a [SII] line with $l_{\rm obs}$=7501. It is most likely that B should be identified with the infrared source.

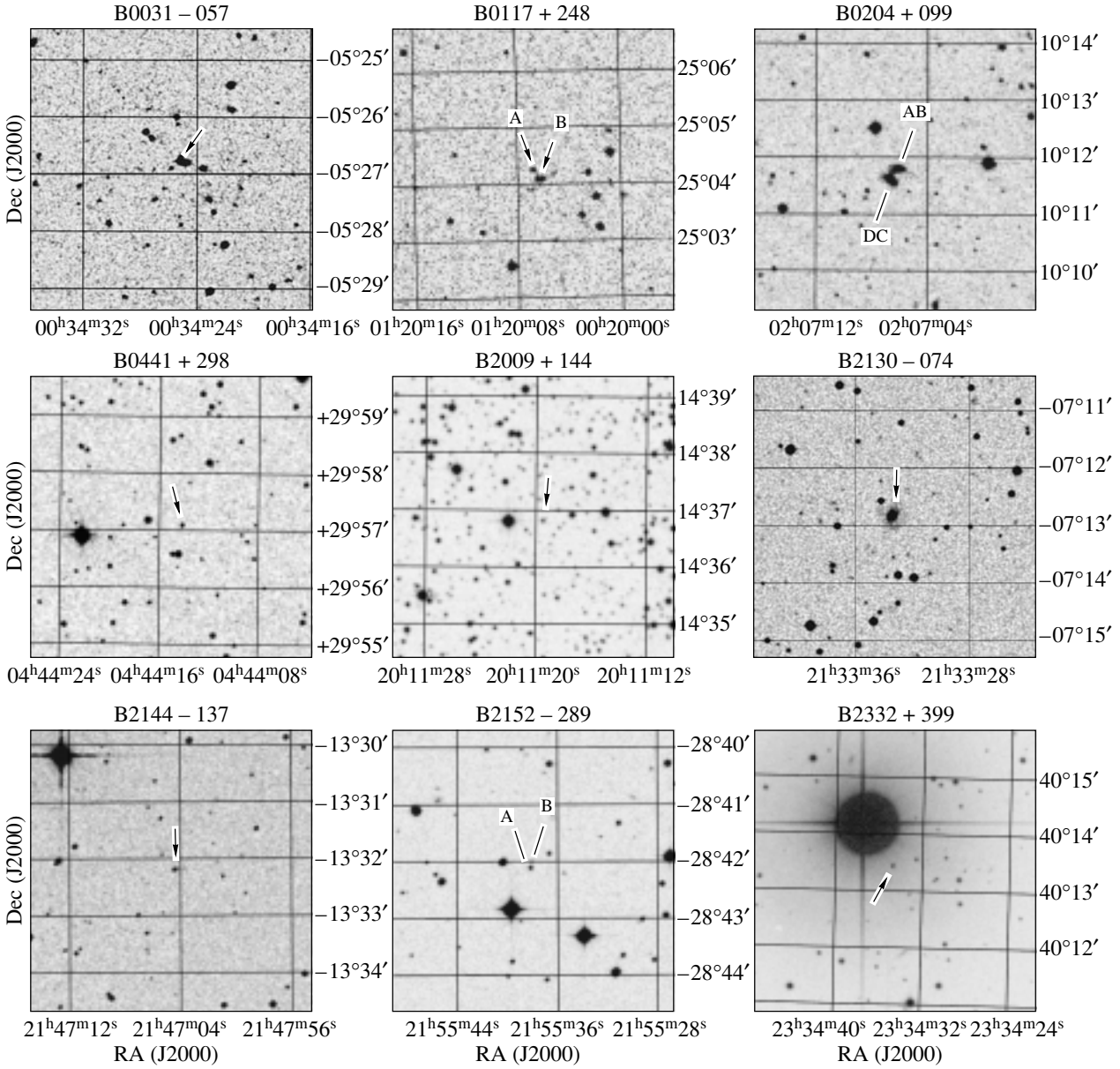

Fig. 3. Maps of the Palomar DSS2 optical counterparts of the radio sources. The arrows show the possible identifications.

The radio source could be associated either with the quasar A or with the pair of interacting galaxies B or possibly represents a superposition of the linear spectra of both these objects.

B0441+298. The radio spectrum is fit by the line $y = 2.418 - 0.951x$. The candidate DSS2 optical counterpart is a stellar object. There are no lines detected in the optical spectrum. It is possible that B0441+298 is a BL Lac object.

B2009+144. The radio spectrum is fit by the line $y = 1.052 - 0.597x$. The candidate DSS2 optical counterpart is a stellar object. The USNO-2 magnitudes are $B = 17\overset{m}{.}1$ and $R = 16\overset{m}{.}7$. The object has a stellar spectrum with Hβ and $H\alpha$ lines.

B2130−074. The radio spectrum is fit by the line $y = 1.771 - 0.783x$. The candidate DSS2 optical counterpart is a spiral galaxy with a bright bulge (see Fig. 4). The USNO-2 magnitudes are $B = 16\overset{m}{.}0$ and $R = 14\overset{m}{.}4$. The galaxy spectrum contains emission lines (which suggest it is an ELG) of Hβ with $l_0 = 4861$, $l_{\rm obs} = 5277$; [OIII] with $l_0 = 4959$, $l_{\rm obs} = 5385$; [OIII] with $l_0 = 5007$, $l_{\rm obs} = 5438$; Hα with $l_0 = 6563$, $l_{\rm obs} = 7300$; and [SII] with $l_{\rm obs} = 7300$, corresponding to a redshift $z = 0.086$.

B2144−137. The radio spectrum is fit by the line $y = 2.499 - 1.137x$. The optical image shows an extended object with a weak component and may be the result of an interaction. The USNO-2 magnitudes are

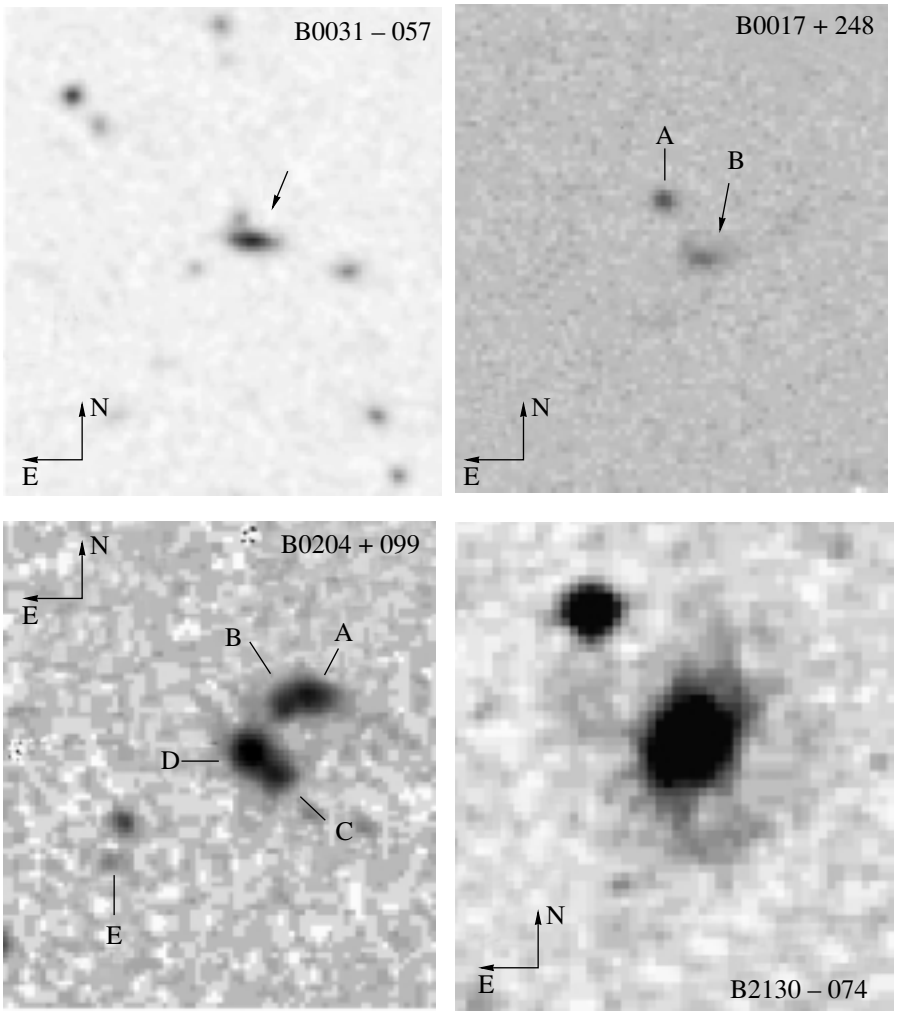

Fig. 4. Enlarged images of some complex objects presented in Fig. 3.

$B = 18^m.2$ and $R = 17^m.8$. The redshift is $z = 0.143$, based on Hβ with $l_0 = 4861$, $l_{\rm obs} = 5562$; [OIII] with $l_0 = 5007$, $l_{\rm obs} = 5715$; Hα with $l_0 = 6563$, $l_{\rm obs} = 7497$; and [SII] with $l_{\rm obs} = 7675$.

B2152−289. The radio spectrum is fit by the parabola $y = -0.752 + 0.593x - 0.161x^2$. The DSS2 image shows two objects with magnitudes $B = 17^m.7$ and $R = 17^m.4$ (A) and $B = 18^m.6$ and $R = 17^m.9$ (B) based on the USNO-2 data. Our spectroscopic data show that object A is an ELG with a redshift of $z = 0.232$, based on Hγ with $l_0 = 4340$, $l_{\rm obs} = 5342$ (absorption); Hβ with $l_0 = 4861$, $l_{\rm obs} = 5986$ (absorption); [OIII] with $l_0 = 4959$, $l_{\rm obs} = 6109$; [OIII] with $l_0 = 5007$, $l_{\rm obs} = 6167$; Hα with $l_0 = 6563$, $l_{\rm obs} = 8088$; and [SII] with $l_{\rm obs} = 8278$. Emission lines with a redshift of $z = 0.232$ observed in the spectrum of object B may originate in object A.

B2332+399. The radio spectrum is fit by the parabola $y = -3.375 + 2.563x - 0.545x^2$. Our spectroscopy reveals a stellar spectrum (Hβ, MgI, NaI, and Hα). The infrared source is probably a nearby A0 SAO star (USNO 1275.18492757) with $R = 5^m.6$.

4. IRAS F02044+0957: A PAIR OF INTERACTING GALAXIES

We studied the source IRAS F02044+0957 (TXS B0204+099) in most detail [14, 15]. It was selected as a bright object in the APM database identified with a steep-spectrum radio source that was not included in any known catalogs. The DSS2 survey resolved it into four objects (Fig. 4), two of which (A, B) were shown by spectroscopic observations (Table 4) to be interacting galaxies (A is a LINER and B is an HII galaxy; $z = 0.093$). Object D is a G star, and object C is an emission-line galaxy that is unrelated to the pair of interacting galaxies ($z = 0.186$). Data on the observed lines are presented in Table 4 (see also Figs. 6, 7). The relative intensities corrected for reddening are normalized to the Hβ flux. The uncertainties in the intensity ratios for all

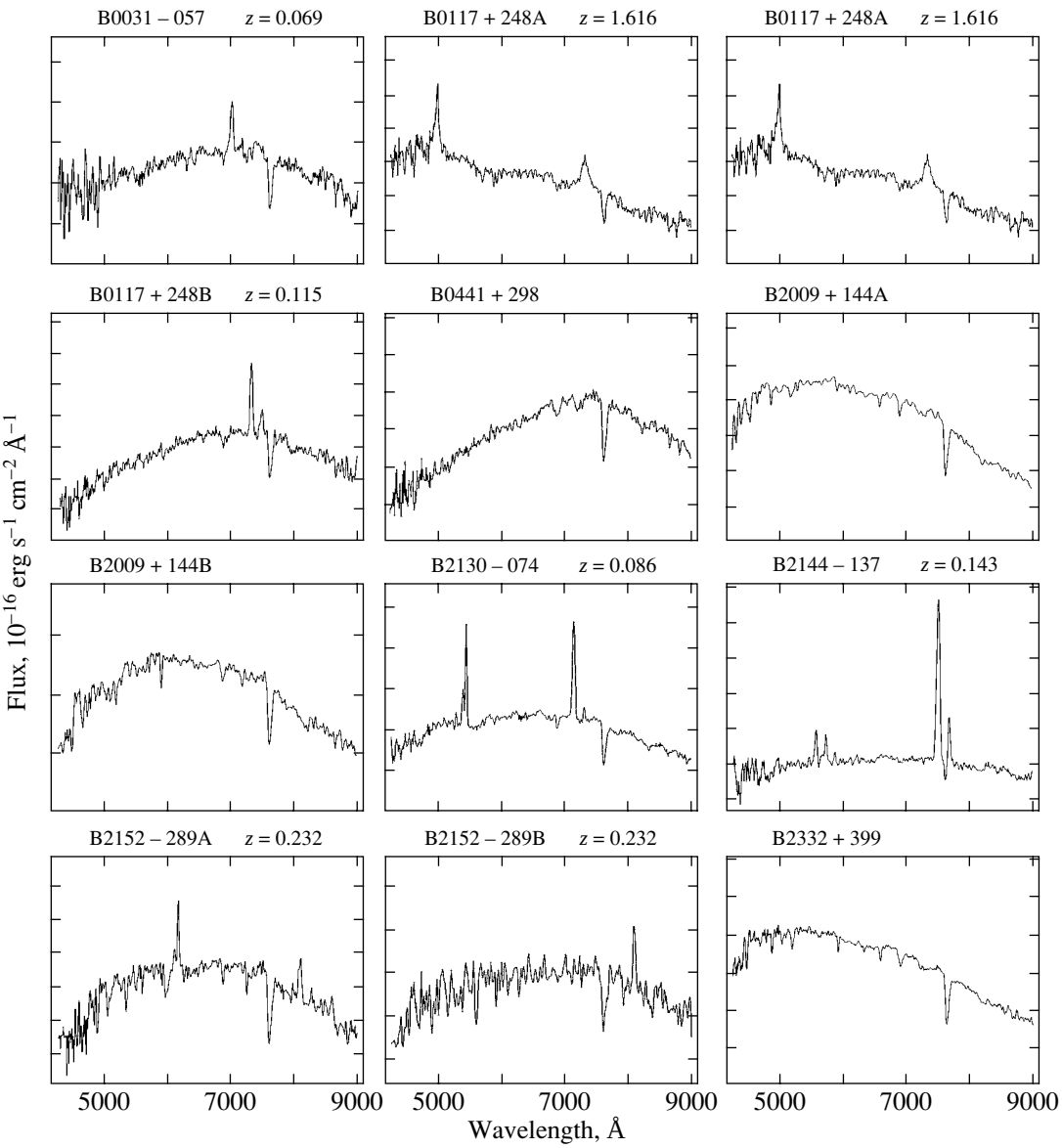

Fig. 5. Spectra of candidate optical counterparts obtained using the spectrograph of the 2.1-m telescope of the Guillermo Haro Observatory.

emission lines considered here are less than 30%, which corresponds to an error of about 0.1 in the logarithm of the intensity ratios. Data for the relative fluxes of objects C and E are not presented, since it was not possible to calculate the reddening coefficient in these cases. The spectrum of object C shows Hα in emission and Hβ in absorption. The spectrum of object E shows Hβ emission that is strongly suppressed by the continuum noise.

We calculated the likelihood function for the identification of the radio source LR [10] for object A, LR = 28.7, and object B, LR = 73.9. The values of this function for the infrared source are LR = 1.52 for A and LR = 1.56 for B. We consider identification with object B to be the most likely for both the radio and infrared sources.

Note that the radio emission of the pair AB has a steep spectrum, and that the total radio luminosity is $L = 9.381 \times 10^{34}$ erg s^{-1} cm^{-2} (for $H_0 =$ 64 km s^{-1} Mpc^{-1} and $q_0 = 0.8$). According to the standard hypothesis [16], the infrared emission of this system could be due to dust arising during the interaction of the galaxies, which enhanced star-formation activity.

The object IRAS F02044+0957 is also located 14.4′ from the center of the galaxy cluster ZwCL 0203.6+1008 (Zwicky 619) [17]. The radius of this cluster is about 12.6′. If this pair of galaxies belongs

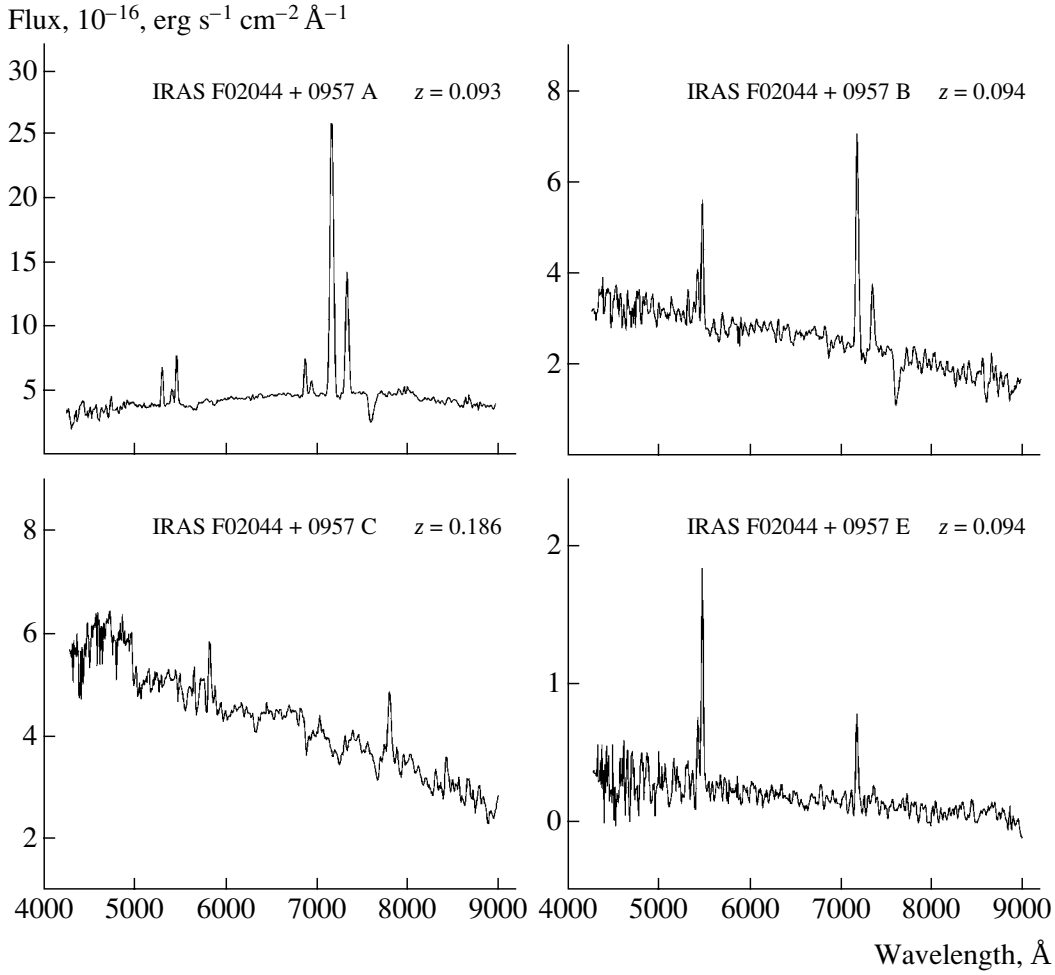

Fig. 6. Optical spectra for objects A, B, C, and E in the region of the source IRAS F02044+0957. The telluric bands at wavelengths λ6867, λ7186, and λ7594 have not been subtracted.

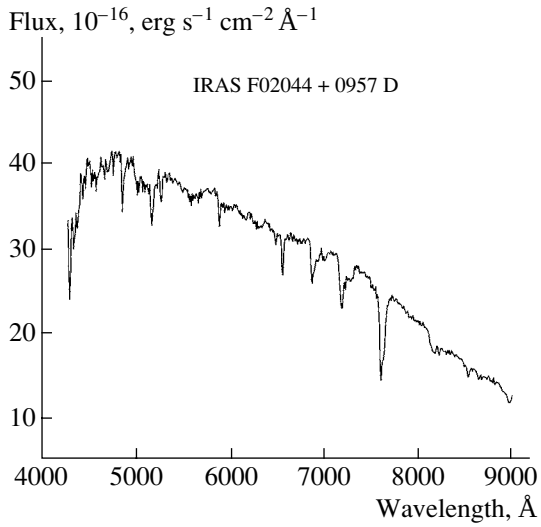

Fig. 7. Spectrum of the G star (object D) near IRAS F02044+0957.

to the cluster, its distance from the cluster center is about 1.6 Mpc ($\Omega_0 = 1$). In addition, object E has the same redshift as the pair AB, suggesting that all three galaxies may belong to the cluster Zwicky 619.

5. CONCLUSION

We have studied two subsamples derived from a cross-identification of the IRAS and low-frequency radio (365 MHz) Texas catalogs. RATAN-600 radio observations were used to confirm the steep ($\alpha < -0.85$, $S \sim \nu^{\alpha}$) spectral indices for sources in the first subsample.

Objects in the second subsample were studied using spectroscopic observations obtained on the 2.1-m telescope of the Guillermo Haro Observatory in Cananea. The list of candidate optical counterparts includes a quasar, interacting galaxies, an infrared galaxy, two emission-line galaxies, a candidate BL Lac object, and two stars. The results of our identifications suggest that roughly a third

of the objects from this subsample are interacting galaxies, in which the infrared emission could be due to dust, and the low-frequency radio emission, which indicates a steep spectrum, is associated with the activity of the galactic nucleus.

6. ACKNOWLEDGMENTS

This work was partially supported by CONACyT grants 28499-E, J32178-E, and 32106-E and by the Russian Foundation for Basic Research (project no. 02-07-90038). The authors thank the staff of the GHO (Mexico) for support during the optical observations and N. N. Bursov for assistance with the RATAN-600 observations. O.V.V. thanks the INAOE staff for hospitality during his visit there.

REFERENCES

1. O. V. Verkhodanov, S. A. Trushkin, H. Andernach, and V. N. Chernenkov, in *Astronomical Data Analysis Software and Systems VI,* Ed. by G. Hunt and H. E. Payne, Astron. Soc. Pac. Conf. Ser. **125**, 322 (1997); http://cats.sao.ru.
2. S. A. Trushkin and O. V. Verkhodanov, Bull. SAO **39**, 150 (1995).
3. IRAS group, *IRAS Point source catalogue; Catalogs and Atlases, Explanatory Supplement* (Joint IRAS Science Working Group, 1987).
4. M. Moshir, *IRAS Faint Source Survey, Explanatory Supplement. Version 1 and Tape,* Ed. by M. Moshir (Infrared Processing and Analysis Center, California Institute of Technology, Pasadena, 1989).
5. S. G. Kleinmann, R. M. Cutri, E. T. Young, *et al.*, in *IRAS Serendipitous Survey Catalogue, Explanatory Supplement* (1986).
6. C. A. Beichman, G. Neugebauer, H. J. Habing, *et al.*, *NASA RP-1190, IRAS, Catalogs and Atlases, Explanatory Supplement* (1988), Vol. 1.
7. J. N. Douglas, F. N. Bash, F. A. Bozyan, *et al.*, Astron. J. **111**, 1945 (1996).
8. O. V. Verkhodanov and S. A. Trushkin, Bull. SAO **50**, 115 (2000).
9. O. V. Verkhodanov, V. O. Chavushyan, S. A. Trushkin, *et al.*, in *Proceedings of the All-Russia Astronomical Conference, St. Petersburg, 2001* [in Russian], p. 32.
10. H. R. de Ruiter, H. C. Arp, and A. G. Willis, Astron. Astrophys., Suppl. Ser. **28**, 211 (1977).
11. K. D. Aliakberov, M. G. Mingaliev, M. N. Naugol'naya, *et al.*, Astrofiz. Issled. (Izv. SAO RAN) **19**, 60 (1985).
12. O. V. Verkhodanov, in *Astronomical Data Analysis Software and Systems VI,* Ed. by G. Hunt and H. E. Payne, Astron. Soc. Pac. Conf. Ser. **125**, 46 (1997).
13. F.-J. Zickgraf, I. Thiering, J. Krautter, *et al.*, Astron. Astrophys., Suppl. Ser. **123**, 103 (1997).
14. O. V. Verkhodanov, V. H. Chavushyan, R. Mújica, *et al.*, in *IAU Colloq. 184: AGN Surveys*, 2001, Ed. by R. Green; astro-ph/0112140.
15. O. V. Verkhodanov, V. H. Chavushyan, R. Mújica, *et al.*, Publ. Astron. Soc. Pac. (2002) (in press).
16. D. B. Sanders, B. T. Soifer, J. H. Elias, *et al.*, Astrophys. J. **325**, 74 (1988).
17. F. Zwicky, E. Herzog, P. Wild, *et al.*, *Catalogue of Galaxies and of Clusters of Galaxies* (California Institute of Technology, Pasadena, 1961–1968), Vols. 1–6.

Translated by D. Gabuzda

Astronomy Reports, Vol. 47, No. 2, 2003, pp. 129–138. Translated from Astronomicheskiĭ Zhurnal, Vol. 80, No. 2, 2003, pp. 151–161.

Solar Millisecond Spikes Manifest Large- and Small-Scale Inhomogeneities of the Coronal Plasma

A. A. Kuznetsov and V. G. Vlasov

Irkutsk State Technical University, Irkutsk, Russia

Received March 22, 2002; in final form, June 26, 2002

Abstract—A model for the generation of solar millisecond radio spikes via a maser cyclotron resonance is proposed. The model takes into account the large-scale inhomogeneity of the magnetic field and small-scale inhomogeneities of the coronal plasma. The efficiency of the energy transformation from a electron beam into maser radiation is estimated. Appropriate parameters of the magnetic field inhomogeneity and the plasma turbulence are found. © *2003 MAIK "Nauka/Interperiodica"*.

1. INTRODUCTION

Solar radio emission is usually used for diagnostics of the solar coronal plasma. From this point of view, solar millisecond radio bursts (spikes) are of particular interest. These spikes are characterized by high brightness temperatures (up to 10^{15} K or higher), short durations (<100 ms), and narrow spectral bandwidths (not exceeding several hundredths of the carrier frequency) [1, 2]. As a rule, spikes appear in large groups containing several thousand individual radio spikes, often drifting in frequency. It is most probable that the maser cyclotron resonance in unstable electron beams is responsible for the generation of spikes [3].

There have been numerous studies of the maser generation of emission in the solar corona. In particular, the growth rate of electromagnetic waves as functions of the parameters of the plasma and electron beam, as well as the relaxation of unstable electron distributions affecting the temporal profiles of spikes, have been studied in detail (see review [4] and references therein). However, there is no universal agreement about the mechanism for the formation of the complex discrete dynamical spectra of spikes; that is, the process giving rise to numerous local sources of radiation in an active region of the solar corona has not been identified. Initially, this fragmentation of the source was associated with the fragmentation of the energy release in solar flares [1], with each spike corresponding to an individual region of energy release and electron acceleration. In [5], the spectra of spikes are explained on the basis of complex nonlinear processes for the formation and relaxation of unstable electron distributions. Paper [4] proposes a model that attributes the spectrum of spikes to small-scale inhomogeneities of the coronal magnetic field: these inhomogeneities give rise to individual local magnetic traps with an unstable electron distribution formed in each, in turn giving rise to the generation of radio emission.

All these models attribute the variability of the temporal and spectral features of spikes to the electron fluxes generating the spikes. We have proposed

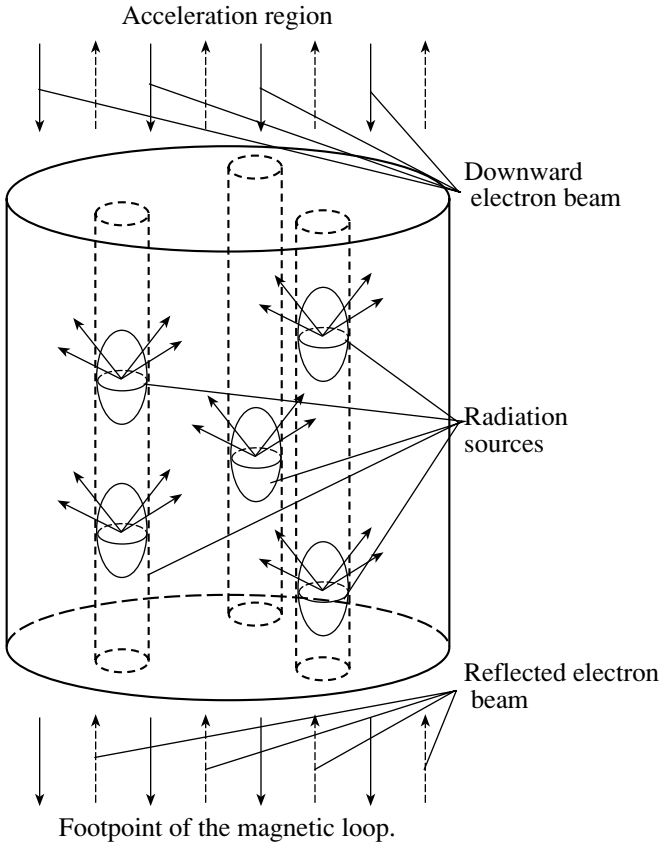

Fig. 1. Schematic of a region of spike generation.

1063-7729/03/4702-0129$24.00

that the formation of spike spectra is mainly associated with inhomogeneities of the coronal plasma that determine the times and places where emission is generated [6]. It turns out that each monotonic large-scale inhomogeneity of the magnetic field with a scale length of the order of the sizes of coronal magnetic loops gives rise to a rapid breakdown of the resonance between electromagnetic waves and the electron beam, drastically shortening the amplification time of the radiation. As a result, electron beams, whose intensity does not exceed a certain limit, become stabilized in the regions of both their formation and propagation through the corona. This stabilization by the varying magnetic field makes possible the formation of an unstable electron distribution due to comparatively slow (compared to the duration of spikes) processes, since there is no immediate relaxation of this distribution and its free energy can be accumulated. On the other hand, when propagating through the corona, the stabilized electron beam does not generate radio emission and can propagate to large distances without appreciable energy losses. The generation of radiation becomes possible only in those local regions where the small-scale plasma inhomogeneities compensate the effect of the varying magnetic field, resulting in a retardation of the resonance breakdown and disruption of the stabilization. Under such conditions, the electron beam becomes long-lived, with its lifetime significantly exceeding the duration of an individual spike and corresponding to that of a spike series; the spatial scale of the region with the unstable electron distribution also considerably exceeds the scales of the radiation sources. In this case, the structure and dynamics of the small-scale plasma inhomogeneities determine the temporal and spectral features of spikes, while the slowly varying parameters of the beam determine the average features of the radio emission (as well as those of the X-ray emission generated by the electrons penetrating deeper in the solar corona). This proposed model for the generation of spikes is presented in Fig. 1, where we have assumed that the unstable electron beam arises when a downward electron flux is partially reflected from the magnetic-field gradient.

Here, we develop this model for the generation of spikes in an inhomogeneous medium. In contrast to the preceding work [6], we will study the relaxation of the electron beam and its effects on the radio emission in more detail. Particular attention is paid to finding the intervals of parameters of the inhomogeneities that can bring about the generation of emission similar to the observed spikes. Based on the detected spectra of spike series, we determine the scale of the magnetic-field inhomogeneity and the parameters of small-scale plasma inhomogeneities in the active region of the solar corona.

2. GENERATION OF RADIO EMISSION IN THE INHOMOGENEOUS MEDIUM

We will study the generation of the first harmonic of the extraordinary wave (X1 mode); i.e., the case when the radiation frequency ω is close to the electron cyclotron frequency ω_H in the source. We will assume that the source is a longitudinal (hollow) electron beam with the following distribution [7]:

$$f_b(v,\theta) = \frac{1}{2\pi^{3/2} v_b^2 \Delta v_b (\Delta\theta_b)^2} \exp\left[-\left(\frac{v-v_b}{\Delta v_b}\right)^2\right] \times \begin{cases} \theta/\Delta\theta_b, & 0 < \theta \le \Delta\theta_b, \\ 2-\theta/\Delta\theta_b, & \Delta\theta_b < \theta \le 2\Delta\theta_b, \\ 0, & \theta > 2\Delta\theta_b, \end{cases} \quad (1)$$

where v and θ are the velocity and pitch angle of the electrons. This distribution has its maximum at $v = v_b$ and $\theta = \Delta\theta_b$. The longitudinal electron beam (1) can amplify electromagnetic waves in the following interval of parameters [6]:

$$\varepsilon_0 > \varepsilon \ge \varepsilon_0\left[1-(\Delta\theta_b)^2\right], \quad (2)$$
$$\varepsilon_0 = \frac{1}{2}\frac{v_b^2}{c^2}\left(1-\frac{v_b^2}{c^2}\right) \le \frac{1}{8},$$

where $\varepsilon = \omega_p^2/\omega_H^2$ and ω_p is the Langmuir frequency. In the presence of the longitudinal beam (1), the maximum growth rate of the X1-mode is [6]

$$\gamma_{\max} \simeq \frac{n_b}{n}\omega\Delta_1 V \frac{c^2}{v_b^2}\frac{v_b}{\Delta v_b \Delta\theta_b}, \quad (3)$$

where n_b and n are the densities of the accelerated particles and background plasma, respectively, $\Delta_1 = (\omega-\omega_H)/\omega$, and $V = \omega_p^2/\omega^2$. Near the X1-mode cutoff, $\Delta_1 \simeq V$.

The radiation intensity is determined by both the growth rate γ and the time Δt during which the electromagnetic wave is in resonance with the electron beam. In a linear approximation, the spectral density W_f of the radiation energy is

$$W_f = W_{f0}\exp(2\gamma\Delta t), \quad (4)$$

where W_{f0} is the spectral energy density of thermal oscillations. The duration of the amplification of the electromagnetic waves is mainly limited by the breaking down of their resonance with the beam in wave-vector space. It was noted in [6, 7] that one can estimate the duration Δt of the resonance as the smaller of two intervals Δt_1 and Δt_2, which, in turn, are determined by the inhomogeneity of the magnetic field and the plasma in the source of radiation. Let us assume that the magnetic field H and plasma

density n have constant scale lengths for their inhomogeneities $L_{H||}$, $L_{H\perp}$ and $L_{p||}$, $L_{p\perp}$, respectively:

$$L_{p||,\perp} = \frac{n}{\partial n/\partial r_{||,\perp}}, \qquad L_{H||,\perp} = \frac{H}{\partial H/\partial r_{||,\perp}}, \quad (5)$$

where $r_{||}$ and $r_{\perp}$ are the spatial coordinates in the directions parallel and perpendicular to the magnetic field. With the longitudinal beam (1), the resonance time Δt_1 then equals [7]

$$\Delta t_1 \simeq \frac{L_{H||}}{c}\frac{v_b}{c}\frac{(\Delta\theta_b)^2}{\delta_{||}}, \quad (6)$$

where $\delta_{||} = 1 + \Delta_1 L_{H||}/L_{p||}$. For a longitudinal beam with energy $E_b = 20$ keV and pitch angle dispersion $\Delta\theta_b = 1/3$, with the longitudinal scale for inhomogeneity of the magnetic field being $L_{H||} = 10^4$ km and without small-scale plasma inhomogeneities ($L_{p||} \to \infty$), we obtain $\Delta t_1 \simeq 1$ ms. It is this quantity that determines the resonance time. The generation of appreciable radio emission requires an amplification factor no lower than e^{20} with respect to the thermal oscillations; i.e., $2\gamma\Delta t > 20$. Consequently, under the specified conditions, the magnetic-field inhomogeneity prevents the generation of radio emission with growth rates $\gamma < 10^4$ Hz.

The duration of the resonance can significantly increase for $\delta_{||} \simeq 0$ or

$$L_{p||} \simeq -\Delta_1 L_{H||}. \quad (7)$$

Here, Δt_1 tends to infinity and the duration of the resonance is determined by Δt_2, which equals [6]

$$\Delta t_2 \simeq \frac{L_{H||}}{c}\Delta\theta_b\left(1 + \frac{1}{4}\frac{L_{H||}^2}{L_{H\perp}^2}\right)^{-1/2}, \quad (8)$$

when condition (7) is satisfied. For the parameters specified above and $L_{H\perp} \simeq L_{H||}$, the time $\Delta t_2 \simeq 10$ ms; that is, stabilized electron beams with growth rates from 10^3 to 10^4 Hz will generate radiation in plasma density depletion satisfying (7).

Expression (7) shows that the plasma-density inhomogeneities must be considerably smaller-scale (since $\Delta_1 \ll 1$) to compensate the effect of the inhomogeneous magnetic field. In addition, the gradient of the plasma density must be opposite to that of the magnetic field. Such conditions can be satisfied only in fairly narrow altitude intervals, where the generation of radio emission will occur. Let us estimate the size of the emission region. We introduce the following model for the small-scale plasma inhomogeneities:

$$n = n_0\left(1 + \frac{\Delta n}{n_0}\sin\frac{2\pi r_{||}}{d}\right) \text{ for } -\frac{d}{2} < r_{||} < \frac{d}{2}. \quad (9)$$

The inhomogeneities are characterized by the amplitude $\Delta n/n_0 \ll 1$ and size $d \ll L_{H||}$. Beyond the interval $-d/2 < r_{||} < d/2$, the plasma density changes much more slowly, with the scale length being $L_{p||0} \sim L_{H||}$, though periodic small-scale inhomogeneities are also possible.

The emission region reaches its maximum size if the compensation of inhomogeneities (7) is precisely fulfilled at $r_{||} = 0$, which requires an inhomogeneity wavelength of

$$d = -2\pi\Delta_1 L_{H||}\frac{\Delta n}{n_0}. \quad (10)$$

We define the emission region as the region where $\Delta t_1 > \Delta t_2$. From (5)–(10), we obtain the following longitudinal size for this region:

$$\Delta r_{||\max} \simeq \frac{d}{\pi}\sqrt{\frac{2v_b\Delta\theta_b}{c}} \simeq 2\Delta_1 L_{H||}\frac{\Delta n}{n_0}\sqrt{\frac{2v_b\Delta\theta_b}{c}}, \quad (11)$$

neglectingtransverseinhomogeneities($L_{H\perp} = L_{p\perp} = \infty$). This size represents an upper limit for the longitudinal emission interval. In reality, the relaxation of the electron beam can occur at distances smaller than $\Delta r_{||\max}$.

Further, we shall show that, for typical conditions in the solar corona, the transverse inhomogeneities of the magnetic field and plasma virtually do not affect the stabilization of electron beams (and the breakdown of the stabilization). Therefore, the determination of the transverse size of the generation region requires some additional assumptions about the parameters of small-scale inhomogeneities. We expect that the transverse and longitudinal dimensions are similar, namely

$$\frac{\Delta r_{\perp}}{\Delta r_{||}} \sim \frac{L_{H\perp}}{L_{H||}}. \quad (12)$$

Electromagnetic waves escape from the spatial emission region over the time $\Delta t_3 \simeq \Delta r_{||\max}/\dot{r}_{||}$, where $\dot{r}_{||}$ is the wave group velocity. Consequently, if $\Delta t_1 \to \infty$, the resonance time is determined by the smaller of Δt_2 and Δt_3. This effect can limit the intensity of the radiation when the size and amplitude of the small-scale inhomogeneities are smaller than a certain limit.

Note that, for extremely intense electron beams (with growth rates exceeding 10^4 Hz in the preceding example), the effect of medium inhomogeneities is less important. These beams will not stabilize, and the generation of radiation will essentially occur in the region of formation of the electron beam, with the particle-acceleration process determining the temporal profile of the radiation. Further, we assume that

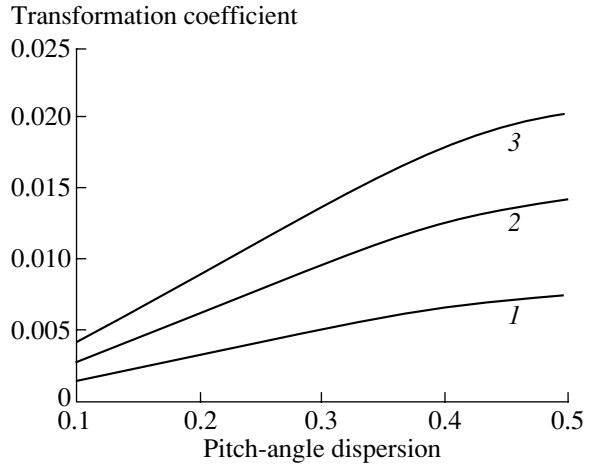

Fig. 2. Efficiency of the energy transformation as a function of the pitch-angle dispersion $\Delta\theta_b$ of the beam for various energy levels: $E_b = 10$ keV (1), $E_b = 20$ keV (2), and $E_b = 30$ keV (3).

the stabilization of the electron beam over most of its trajectory is a necessary condition.

The bandwidth $\Delta\omega$ of the radiation is determined by both the source size and the parameters of the electron beam. We can estimate the bandwidth as

$$\Delta\omega \simeq \Delta\omega_{\rm MCR} + \Delta\omega_{||} + \Delta\omega_{\perp}, \quad \frac{\Delta\omega_{||,\perp}}{\omega} \simeq \frac{\Delta r_{||,\perp}}{L_{H||,\perp}}, \tag{13}$$

where $\Delta\omega_{\rm MCR}$ is the minimum possible bandwidth associated with the spread of electron energies in the beam. For the longitudinal beam (1), we obtain [6, 7]

$$\frac{\Delta\omega_{\rm MCR}}{\omega} \simeq \left(\frac{v_b \Delta\theta_b}{c}\right)^2. \tag{14}$$

3. QUASI-LINEAR RELAXATION OF ELECTRON BEAMS

To estimate the efficiency of the transformation of energy from the electron beam into radiation via the maser cyclotron resonance, we use a model for this process that is similar to that proposed in [8, 9]. The equation describing electron diffusion in velocity space takes the form [8]

$$\frac{\partial f_b}{\partial t} = D\left(\frac{\partial^2 f_b}{\partial v_\perp^2} + \frac{1}{v_\perp}\frac{\partial f_b}{\partial v_\perp}\right), \tag{15}$$

where $f_b = f_b(t, v_{||}, v_\perp)$, $v_{||}$ and $v_\perp$ are the longitudinal and transverse (with respect to the magnetic field) particle velocities, and D is the diffusion coefficient

$$D = \frac{4\pi^2 e^2}{m_e^2}\int W_k \delta(\omega - k_{||}v_{||} - \omega_H/\Gamma)\mathrm{d}^3 k. \tag{16}$$

In (16), $\mathbf{k}$ is the wave vector of the electromagnetic waves, $\Gamma = (1 - v^2/c^2)^{-1/2}$ the Lorentz factor, and W_k the spectral density of the radiation energy. The diffusion coefficient is determined by the integral of the spectral energy density along the resonance curve. When the radiation energy is contained in a narrow interval of wave vectors at $k_{||} \simeq k_{||*}$, the diffusion coefficient is [9]

$$D \simeq \frac{4\pi^2 e^2}{m_e^2}\frac{W}{k_{||*} v_{||*}}, \tag{17}$$

where W is the total energy density of the electromagnetic waves (in the frequency interval $\Delta\omega_{\rm MCR}$) and $v_{||*}$ is the characteristic velocity of the particles participating in the resonance. The diffusion coefficient is virtually independent of the transverse velocity $v_\perp$ of the electrons.

Let us consider the stationary case; i.e., we assume that the properties of the source of the electron beam (acceleration region) remain constant for a fairly long time, and the physical conditions beyond the region of formation of the beam are also constant. A stationary state will then be established after some time, and the electron beam and radiation will depend solely on the spatial coordinate $r_{||}$ (parallel to the magnetic field) along the motion of the beam, that is, $\partial f_b/\partial t = v_{||}\partial f_b/\partial r_{||}$. Let us introduce the new variable

$$\tau(r_{||}) = \frac{1}{v_{||}}\int_0^{r_{||}} D(r'_{||})\mathrm{d}r'_{||}. \tag{18}$$

Equation (15) then takes the simple form

$$\frac{\partial f_b}{\partial \tau} = \frac{\partial^2 f_b}{\partial v_\perp^2} + \frac{1}{v_\perp}\frac{\partial f_b}{\partial v_\perp}. \tag{19}$$

Its solution is the following [9]:

$$f_b(\tau, v_{||}, v_\perp) \tag{20}$$
$$= \frac{1}{2\tau}\int_0^\infty f_{b0}(v_{||}, \xi) I_0\left(\frac{\xi v_\perp}{2\tau}\right)\exp\left(-\frac{\xi^2 + v_\perp^2}{4\tau}\right)\xi\mathrm{d}\xi,$$

where $f_{b0}(v_{||}, \xi) = f_b(\tau, v_{||}, v_\perp)\big|_{\tau=0,\, v_\perp=\xi}$ is the initial distribution of the electron beam (at $r_{||} = 0$), and $I_0(z)$ is the zeroth-order Bessel function with an imaginary argument.

The radiation of electromagnetic waves brings the distribution closer to equilibrium and stops the emission after a certain time. We will assume that the electron distribution becomes stable when [8]

$$\left.\frac{\partial f_b}{\partial v_\perp^2}\right|_{v_\perp=0} = 0. \tag{21}$$

We obtain from (20)

$$\left.\frac{\partial f_b}{\partial v_\perp^2}\right|_{v_\perp=0} = \frac{1}{8\tau^2}\int_0^\infty f_{b0}(v_{||},\xi)\left(\frac{\xi^2}{4\tau}-1\right)\exp\left(-\frac{\xi^2}{4\tau}\right)\xi d\xi. \quad (22)$$

Let us estimate the coefficient for the transformation of energy from the longitudinal electron beam into radiation. Substituting the expression for the model distribution (1) in place of f_{b0} in (22) and solving Eqs. (21)–(22) numerically, we obtain $\tau = \tau_s$ for the beam-relaxation parameter. Let us assume that the growth rate γ and the radiation energy density W remain approximately constant over some interval l_s that is equal to the relaxation length. We obtain from (17) and (18)

$$\tau_s = \frac{4\pi^2 e^2}{m_e^2}\frac{W l_s}{k_{||*} v_{||*}^2}. \quad (23)$$

For the longitudinal beam (1), $v_{||*} \simeq v_b$ and $k_{||*} \simeq \omega v_b/c^2$ [6].

The energy flux of the radiation from a region with length l and cross section S is

$$\Phi_e = \frac{\partial W}{\partial t} Sl = 2\gamma W Sl. \quad (24)$$

On the other hand, the energy flux of the electron beam through the area S is

$$\Phi_b = n_b E_b v_b S, \quad (25)$$

where E_b is the electron energy. We obtain for the coefficient η of the energy transformation the expression

$$\eta = \frac{\Phi_e}{\Phi_b} \simeq \frac{2}{\pi}\frac{\tau_s}{c^2}\frac{v_b}{\Delta v_b \Delta\theta_b}\varsigma, \quad (26)$$

$$\varsigma = \frac{1 - v_b^2/c^2}{1 - 0.5 v_b^2/c^2} \simeq 1$$

using (2)–(3) and (23).

Figure 2 presents the coefficient η for the energy transformation as a function of the pitch-angle dispersion $\Delta\theta_b$. The maser mechanism transforms into radiation that portion of the particle energy that corresponds to the transverse component of its velocity $v_\perp$. Therefore, increasing the pitch-angle dispersion increases the efficiency of the energy transformation. If the electron beam's energy is $E_b = 20$ keV and the distribution parameters are $\Delta v_b/v_b = \Delta\theta_b = 1/3$, we find from (26) that $\eta \simeq 1.06\%$. This estimate is close to those obtained in [8, 10] for the idealized case when the escape of waves and particles from the radiation-generation region was neglected.

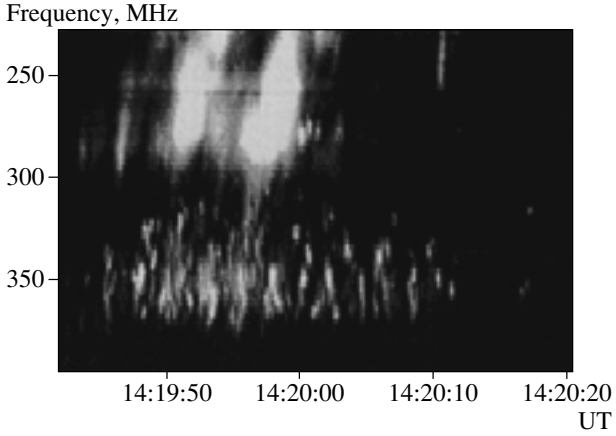

Fig. 3. The spectrogram of the solar radio emission detected January 1, 1981. A series of spikes was observed at frequencies exceeding 300 MHz (with type III bursts at lower frequencies). This plot was presented in [13].

4. IRREGULARITIES OF THE MAGNETIC FIELD AND PLASMA IN THE REGION OF SPIKE GENERATION

In this section, we estimate the physical conditions which can give rise to radio emission with the observed characteristics in active regions of the solar corona. The spectral density of the flux of radiation energy detected at the Earth is

$$I_f \simeq \frac{2\gamma W_f S \Delta r_{||}}{\chi \Omega R_0^2}, \quad (27)$$

where S is the cross section of the source; $\Delta r_{||}$ is the longitudinal size of the source, defined as the smaller of the length $\Delta r_{||\max}$ for the compensation between the plasma and magnetic-field inhomogeneities and the relaxation length l_s; χ is the absorption coefficient for the propagating radiation; Ω is the solid angle containing the radiation; and R_0 is an astronomical unit. The conditions in the second gyro-resonance layer (where the local electron cyclotron frequency is half that in the radiation source) exert a dominating influence on the absorption coefficient χ. The computations of [11, 12] show the following: (a) there are so-called windows of transparency where the absorption can be weak within certain very narrow intervals of parameters; (b) the X1-mode radiation is almost completely absorbed in the remaining cases; (c) some fraction of the radiation can penetrate through the second gyro-resonance layer due to nonlinear effects (absorption and subsequent re-radiation), with the efficiency of this process being about 1%. Thus, the absorption coefficient remains virtually completely unknown. We shall assume that this quantity is within the range $1 < \chi \leq 100$.

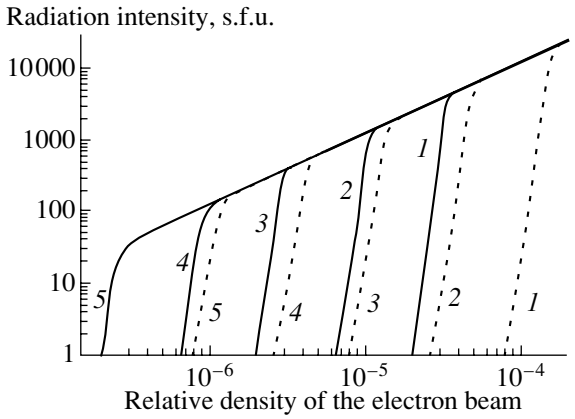

Fig. 4. The radiation intensity as a function of the relative density of the electron beam for various scale lengths of the longitudinal inhomogeneity of the magnetic field: $L_{H||} = 10^3$ km (*1*), $L_{H||} = 3 \times 10^3$ km (*2*), $L_{H||} = 10^4$ km (*3*), $L_{H||} = 3 \times 10^4$ km (*4*), and $L_{H||} = 10^5$ km (*5*). The solid and dashed curves correspond to $L_{H\perp} = L_{H||}$ and $L_{H\perp} = 0.1L_{H||}$, respectively. The amplitude of the small-scale plasma inhomogeneities is $\Delta n/n_0 = 0.2$.

Figure 3 presents an example of the dynamic spectrum of the solar radio emission. There is a typical group of spikes in the frequency interval 300–380 MHz. We assume that the spikes are bursts of X1 radiation, so that the radiation frequency uniquely determines the strength of the source magnetic field. In subsequent calculations, we shall use an electron cyclotron frequency of $f_H = 350$ MHz. Condition (2) limits the plasma density in the source of the spikes to $n < 1.9 \times 10^8$ cm^{-3}. However, if the plasma density is close to this limit, radiation can be generated only by electrons with energies about 200 keV. The generation of emission by electron beams with lower energies requires a lower plasma density. We then use the following parameters: plasma density $n = 5 \times 10^7$ cm^{-3}, plasma temperature $T = 10^6$ K, and electron beam energy $E_b = 20$ keV. The beam distribution has a pitch-angle dispersion $\Delta\theta_b = 1/3$ and thermal spread $\Delta v_b/v_b = 1/3$ (similar electron beams have been observed in the Earth's magnetosphere).

Let us first consider the effect of the intensity of the electron beam on the generation of radiation. Figure 4 shows the intensity I_f of the radiation observed at the Earth as a function of the relative density of the electron beam n_b/n. Here, we assume that the cross section of the source is $S = 100 \times 100$ km^2 and that there is no absorption; i.e., $\chi = 1$. We assume that the angle Ω describing the directivity pattern of the radiation is $\pi/2$ and also that there are small-scale plasma inhomogeneities with amplitude $\Delta n/n_0 = 0.2$ and size (10) in the corona (considering only radiation from a single interval for the compensation between the plasma and magnetic field inhomogeneities). Thus, the resonance time is determined by the intervals Δt_2 and Δt_3. When the density of the electron beam is comparatively low, the relaxation length exceeds the inhomogeneity-compensation length, and the radiation intensity grows exponentially with increasing beam density. Beginning with some critical n_b/n, the relaxation length becomes smaller than the compensation length, with the longitudinal size of the emission region being determined by the former. Here, the coefficient for the transformation of particle energy into radiation reaches its maximum, defined by (26), and the radiation intensity becomes proportional to the beam density. The larger the scale lengths (longitudinal and transverse) of the magnetic field inhomogeneity, the faster the beam saturation. To provide a typical spike intensity of 100 sfu, the relative electron beam density must be no lower than 10^{-6} without absorption ($\chi = 1$) and no lower than 10^{-4} with $\chi = 100$. We should also allow for the fact that the transverse source size may differ from our estimate.

This analysis shows that we cannot precisely determine the density of electron beams in the solar corona using energetic estimates (comparisons with the observed radio emission). Consequently, we likewise cannot determine whether the free energy of the beam is completely released in a single emission interval (in which the effects of the plasma and magnetic field inhomogeneities compensate each other) or, alternatively, whether a single beam can generate radiation in several appropriate regions situated above one other. Thus, we must analyze the effect of the relaxation of the electron beam on the temporal and spectral features of both individual spikes and spike series. Two alternatives are possible here.

(1) The electron beam loses only some of its free energy while passing through a region appropriate for the generation of spikes (this corresponds to the interval of exponential growth in Fig. 4, $\Delta r_{||\max} < l_s$). Small differences in the parameters of the electron beam and the plasma of the various sources of spikes result in considerable exponential differences in the radiation intensity. Consequently, the intensities of individual radio bursts will differ significantly.

(2) The electron beam becomes saturated in a single interval of the compensation between the plasma and magnetic-field inhomogeneities ($l_s < \Delta r_{||\max}$). Here, the radiation intensity is proportional to the beam density and the source cross section. We expect that the parameters of the electron beam and small-scale plasma inhomogeneities (and, consequently, the dimensions of spike sources) are approximately constant within a coronal magnetic loop. Hence, the

intensity of spikes in a series also becomes approximately constant (or at least the spread will be much smaller than in the preceding case). Changes in the cross section of the electron beam will result in proportional changes in the number of radiation sources, that is, in the number of spikes generated per unit time (the cross section of the electron beam is close to the diameter of a magnetic loop, and significantly exceeds the cross section of the source of an individual spike), and will simultaneously result in proportional changes in the X-ray intensity. Finally, there should be a correlation between the X-ray intensity and the mean radio intensity, with the intensity of individual spikes being virtually constant.

In [6], we examined the first alternative for the relaxation regime, when the energy losses of the electron beam over a single emission interval are neglected. However, Fig. 4 shows that the corresponding interval (in which the intensity depends exponentially on the electron beam density and other source parameters and simultaneously exceeds some minimum level) is comparatively narrow. Therefore, the second alternative for the relaxation regime seems more likely. A statistical analysis of a large number of observations [14, 15] shows that the second alternative for the relaxation regime is quite typical for solar millisecond spikes. Let us consider this regime in more detail; i.e., we will assume that, if the stabilization of the electron beam breaks down due to small-scale plasma inhomogeneities, the relaxation of the beam is very rapid; that is, it occurs within a single interval for the stabilization breakdown. This results in the condition $l_s < \Delta r_{||\max}$, which limits the scale length of the longitudinal inhomogeneity of the magnetic field from below.

Figure 5 shows the dependence of the relaxation length (or more precisely, the relative value $l_s/L_{H||}$) on the scale length $L_{H||}$ of the longitudinal inhomogeneity of the magnetic field. As for Fig. 4, we assume that the small-scale plasma inhomogeneities break down the stabilization of the electron beam, and the resonance time is determined by the intervals Δt_2 and Δt_3. The scale length for the transverse inhomogeneity of the magnetic field is $L_{H\perp} = L_{H||}$, while the amplitude of the small-scale plasma inhomogeneities is $\Delta n/n_0 = 0.2$. When the relaxation length calculated in this way becomes larger than $\Delta r_{||\max}$, the beam relaxation does not occur in a single emission interval (if there are no other regions for the compensation of the inhomogeneities in the subsequent motion of the beam, the relaxation does not occur at all). A conventional relaxation length for this case is shown by the dashed curve.

The minimum scale lengths for the longitudinal inhomogeneity of the magnetic field on which the

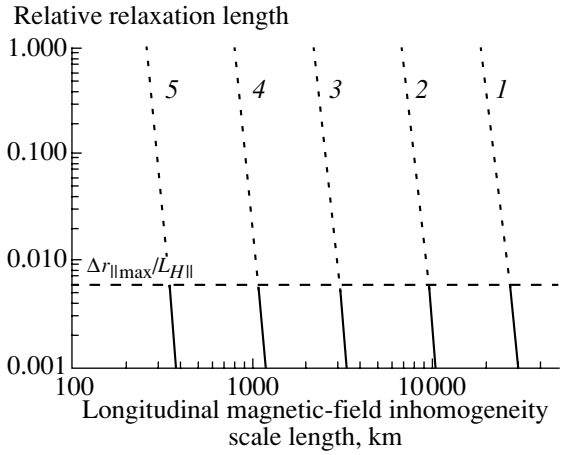

Fig. 5. The relative length $l_s/L_{H||}$ of the electron beam relaxation in the presence of small-scale plasma inhomogeneities as a function of the scale length for longitudinal inhomogeneity of the magnetic field for various electron beam densities: $n_b/n = 10^{-6}$ (*1*), $n_b/n = 3 \times 10^{-6}$ (*2*), $n_b/n = 10^{-5}$ (*3*), $n_b/n = 3 \times 10^{-5}$ (*4*), and $n_b/n = 10^{-4}$ (*5*). The amplitude of the small-scale plasma inhomogeneities is $\Delta n/n_0 = 0.2$.

electron beam relaxation occurs for distances smaller than $\Delta r_{||\max}$ are presented in the table. Obviously, the denser the beam, the smaller the minimum scale lengths. Sharp transverse gradients of the magnetic field exert a stabilizing effect on the beam, so that the requirements for homogeneity of the magnetic field are enhanced for $L_{H\perp} = 0.1 L_{H||}$ (compared to the situation in Fig. 5). A decrease in the amplitude of the small-scale plasma inhomogeneities exerts a similar effect and leads to a shortening of both the required wavelength of the inhomogeneities and the interval $\Delta r_{||\max}$. As a result, the spatial escape of the radiation from the emission region becomes appreciable.

Finally, the magnetic field in the solar corona must not exhibit large gradients in order not to prevent the efficient generation of radio emission in the presence of the appropriate small-scale plasma inhomogeneities. However, in the absence of such small-scale plasma inhomogeneities, the large-scale inhomogeneity of the magnetic field will stabilize the electron beam. We can see in Fig. 3 that the individual radio bursts (probably generated by a single beam) on the series of spikes are spread over a fairly large frequency interval (about 80 MHz for a typical frequency of 350 MHz). Consequently, we can estimate the longitudinal size $\Delta R_{||}$ of the emission region for a series of spikes as $\Delta R_{||}/L_{H||} \simeq 0.25$. To generate spikes throughout this region, the electron beam must traverse the distance $\Delta R_{||}$ without considerable energy losses. We will impose the condition that the electron beam must not lose more than half of its free

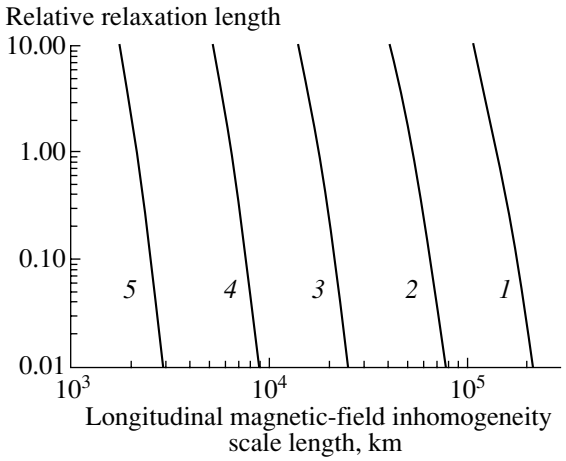

Fig. 6. The relative relaxation length $l_s/L_{H||}$ of the electron beam as a function of the scale length of the longitudinal inhomogeneity of the magnetic field for various electron beam densities and no small-scale plasma inhomogeneities. The notation is the same as in Fig. 5.

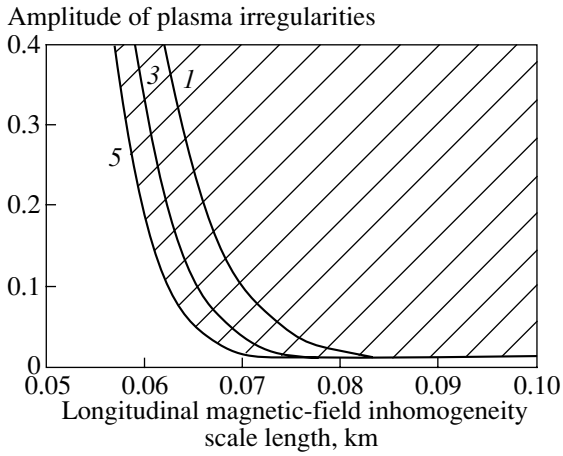

Fig. 7. Region of parameters of the large-scale inhomogeneity of the magnetic field and small-scale plasma inhomogeneities for which the generation of spikes is possible. Limiting curves are shown for various densities of the electron beam. The notation is the same as in Fig. 5.

energy at the distance $\Delta R_{||}$; that is, in the absence of small-scale plasma inhomogeneities, the relaxation length l_s must be at least twice the longitudinal length of the region in which the series of spikes is emitted ($l_s > 2\Delta R_{||}$). This condition limits the scale length of the longitudinal inhomogeneity of the magnetic field from above.

Figure 6 presents the dependence of the relaxation length l_s (more precisely, of the relative value $l_s/L_{H||}$) of the electron beam on the scale length $L_{H||}$ for the longitudinal inhomogeneity of the magnetic field. The plasma is assumed to be homogeneous ($L_{p||} \to \infty$), and the resonance time is determined by the time Δt_1. The generation of the spike series shown in Fig. 3 requires that $l_s/L_{H||} > 0.5$. We present in the table the maximum scale lengths $L_{H||\max}$ for the longitudinal inhomogeneity of the magnetic field that satisfy this condition. Like the resonance time Δt_1, they are independent of the transverse inhomogeneity of the magnetic field.

Intervals of appropriate scale lengths $L_{H||}$ of the longitudinal inhomogeneity of the magnetic field

Scale lengths $L_{H\|\|}$ of the inhomogeneity		n_b/n		
		10^{-6}	10^{-5}	10^{-4}
$L_{H\|\|\min}$, km	(1)	2.7×10^4	3.1×10^3	3.4×10^2
	(2)	1.1×10^5	1.2×10^4	1.4×10^3
	(3)	4.8×10^4	5.5×10^3	6.2×10^2
$L_{H\|\|\max}$, km		1.5×10^5	1.9×10^4	2.3×10^3

The minimum lengths $L_{H||\min}$ are presented for three cases: $L_{H\perp} = L_{H||}$ and $\Delta n/n_0 = 0.2$ (1); $L_{H\perp} = 0.1 L_{H||}$ and $\Delta n/n_0 = 0.2$ (2); $L_{H\perp} = L_{H||}$ and $\Delta n/n_0 = 0.1$ (3).

The table shows that the stabilization of electron beams with a relative density of $n_b/n \geq 10^{-4}$ requires comparatively large gradients of the magnetic field. Though such inhomogeneities can probably occur in the solar corona, those with $L_{H||} \simeq 10^4$–10^5 km are more typical. This corresponds to smaller densities for the electron beams ($n_b/n < 10^{-4}$).

Note that the stabilization of the electron beam in the absence of small-scale plasma inhomogeneities is still required for both alternative scenarios for the beam relaxation. Therefore, the calculated maximum scale lengths $L_{H||\max}$ for the longitudinal inhomogeneity of the magnetic field will coincide in these cases. However, the minimum length $L_{H||\min}$ corresponds only to the complete relaxation of the electron beam within a single wavelength of the small-scale plasma inhomogeneity. The observations show that the frequency spread of the spikes within each series is comparable to the typical spike frequency [1, 16], i.e., $\Delta R_{||} \sim L_{H||}$. Here, the conditions for the stabilization of the electron beam become somewhat more rigorous than in the case considered.

A decrease in either the scale length for the transverse inhomogeneity of the magnetic field or the amplitude of the small-scale plasma inhomogeneities narrows the interval of appropriate scale lengths for the longitudinal inhomogeneity of the magnetic field. If this interval tends to zero, the generation of spikes becomes impossible, since either the breakdown of

the resonance in phase space (due to the transverse inhomogeneity of the magnetic field) or the escape of the wave from the emission region in coordinate space (due to the small dimensions of this region) will prevent the required amplification of the radiation, even when the stabilizing effect of the magnetic field inhomogeneity is compensated by the plasma inhomogeneities.

The curves in Fig. 7 present solutions of the equation $L_{H||\min} = L_{H||\max}$. The horizontal axis shows the ratio $L_{H\perp}/L_{H||}$ of the scale lengths of the transverse and longitudinal inhomogeneities of the magnetic field, while the vertical axis shows the amplitude $\Delta n/n_0$ of the small-scale plasma inhomogeneities. The efficient generation of radio emission becomes possible when the parameters of the medium are to the right and above the curves indicated in Fig. 7. If $L_{H\perp}/L_{H||}$ is of the order of 0.1 or more, the presence of plasma inhomogeneities with amplitudes of 1–2% in the active region is sufficient for the generation of spikes. The transverse inhomogeneity of the magnetic field prevents spike generation only for extremely small scale lengths $L_{H\perp}/L_{H||} < 0.07$. The necessary parameters of the medium in the region of spike generation are virtually independent of the electron beam density.

Let us estimate the scale length of the plasma inhomogeneities and the size of the spike sources. If the longitudinal scale length of the magnetic field inhomogeneity is $L_{H||} = 10^4$ km and the amplitude of the small-scale plasma inhomogeneities is $\Delta n/n_0 = 0.01$ (the minimum amplitude required for the spike generation), the compensation of the stabilizing effect of the magnetic field inhomogeneity requires a plasma inhomogeneity wavelength of $d \simeq 21$ km, and the maximum interval for spike generation becomes $\Delta r_{||\max} \simeq 3$ km. The longitudinal size of the source contributes to the formation of the spectral band of radiation at a level of $\Delta\omega_{||}/\omega \simeq 0.03\%$ (or lower if the electron beam relaxation occurs in an interval smaller than $\Delta r_{||\max}$). The effect of the transverse size of the source on the radiation spectrum $\Delta\omega_\perp$ is probably of the same order of magnitude, and the minimum bandwidth $\Delta\omega_{\rm MCR}$ of the radiation is $\Delta\omega_{\rm MCR}/\omega \simeq 0.8\%$. There are observations of spikes with relative bandwidths not exceeding 0.17% [17]. Radiation with these spectral characteristics can be generated by an electron beam with a pitch-angle dispersion of $\Delta\theta_b \simeq 0.12$ and an energy of $E_b = 20$ keV with the parameters for the small-scale plasma inhomogeneities specified above.

CONCLUSIONS

One of the characteristic features of solar millisecond spikes is the high correlation between the total energy flux of the radio emission and the X-ray intensity. The intensity of individual radio bursts remains virtually constant while the total radio intensity changes due to changes in the number of spikes per unit time [14, 15]. Our study has shown that this can easily be explained by taking into account the effect of the magnetic field and plasma inhomogeneities (both large- and small-scale) on the generation of radiation via the maser cyclotron resonance. The proposed model for spike generation in an inhomogeneous medium can put constraints on the required intervals for parameters of the medium in the active region, first and foremost, the parameters of the inhomogeneities. A longitudinal large-scale inhomogeneity of the magnetic field with a scale length of $L_{H||} \simeq 10^4$–10^5 km, of the order of the size of a coronal magnetic loop, stabilizes electron beams over most of their trajectories but does not prevent the generation of radiation in some local regions where its stabilizing effect is partially compensated by the plasma inhomogeneities. The observed transverse sizes of magnetic loops correspond to ratios of the inhomogeneity scale lengths $L_{H\perp}/L_{H||} \simeq 0.1$–$0.5$. Under these conditions, the transverse magnetic-field inhomogeneity also limits the amplification of the radiation and relaxation of the electron beam, but this effect is not as important as that produced by the longitudinal inhomogeneity. The generation of spikes requires small-scale plasma inhomogeneities with an amplitude of several per cent and typical sizes of tens of kilometers. The observations (see [2, 12] and references therein) verify the presence of such turbulence.

ACKNOWLEDGMENTS

This work was previously presented in electronic journal [18]. This work was supported by the Russian Ministry of Education (E00-8.0-71).

REFERENCES

1. A. O. Benz, Sol. Phys. **104**, 99 (1986).
2. T. S. Bastian, A. O. Benz, and D. E. Gary, Ann. Rev. Astron. Astrophys. **36**, 131 (1998).
3. D. B. Melrose and G. A. Dulk, Astrophys. J. **259**, 844 (1982).
4. G. D. Fleĭshman and V. F. Mel'nikov, Usp. Fiz. Nauk **168**, 1265 (1998) [Phys. Usp. **41**, 1157 (1998)].
5. P. A. Robinson, Sol. Phys. **134**, 299 (1991).
6. V. G. Vlasov, A. A. Kuznetsov, and A. T. Altyntsev, Astron. Astrophys. **382**, 1061 (2002).
7. V. G. Vlasov, Fiz. Plazmy **17**, 165 (1991) [Sov. J. Plasma Phys. **17**, 96 (1991)].

8. C. S. Wu, S. T. Tsai, M. J. Xu, and J. W. Shen, Astrophys. J. **248**, 384 (1981).
9. H.-W. Li, Sol. Phys. **111**, 167 (1987).
10. R. R. Sharma, L. Vlahos, and K. Papadopoulos, Astron. Astrophys. **112**, 377 (1982).
11. M. E. McKean, R. M. Winglee, and G. A. Dulk, Sol. Phys. **122**, 53 (1989).
12. P. A. Robinson, Sol. Phys. **136**, 343 (1991).
13. A. O. Benz, A. Csillaghy, and M. J. Aschwanden, Astron. Astrophys. **309**, 291 (1996).
14. M. Güdel, M. J. Aschwanden, and A. O. Benz, Astron. Astrophys. **251**, 285 (1991).
15. M. J. Aschwanden and M. Güdel, Astrophys. J. **401**, 736 (1992).
16. H. Isliker and A. O. Benz, Astron. Astrophys., Suppl. Ser. **104**, 145 (1994).
17. P. Messmer and A. O. Benz, Astron. Astrophys. **354**, 287 (2000).
18. A. A. Kuznetsov and V. G. Vlasov, Electronic Journal "Issledovano v Rossii," No. 20, 212 (2002), http://zhurnal.ape.relarn.ru/articles/2002/020.pdf.

Translated by V. Badin

Astronomy Reports, Vol. 47, No. 2, 2003, pp. 139–150. Translated from Astronomicheskiĭ Zhurnal, Vol. 80, No. 2, 2003, pp. 162–174.

Solar Large-Scale Channeled Dimmings Produced by Coronal Mass Ejections

I. M. Chertok and V. V. Grechnev

Institute of Terrestrial Magnetism, Ionosphere, and Radiowave Propagation, Russian Academy of Sciences, Troitsk, Moscow oblast, 142190 Russia
Institute for Solar–Terrestrial Physics, P.O. Box 4026, Irkutsk, 664033 Russia

Received June 13, 2002; in final form, August 21, 2002

Abstract—A new type of dimmings, or transient coronal holes (i.e., regions of reduced soft-X-ray and EUV emission), is revealed in analyses of difference solar images obtained with the SOHO EIT ultraviolet telescope at 195 Å. Such features can be observed on the solar disk after halo-type coronal mass ejections (CMEs). If several active regions, filaments, and other structures are present on the disk during a major eruptive event, then strongly anisotropic, channel-shaped ("channeled") dimmings coexist with relatively compact dimmings adjacent to the eruption center. The channeled dimmings are comparable to the compact dimmings in terms of their contrast; stretch along several narrow, extended features (channels); and can span nearly the entire visible disk. Coronal waves, which appear as fronts of enhanced brightness traveling ahead of the dimmings in some halo CME events, are also anisotropic. We argue that such transient phenomena are closely related to the strong disturbance and restructuring of large-scale magnetic fields involved in CMEs, and the channeled character of the dimmings reflects the complexity of the global solar magnetosphere, in particular, near the solar-activity maximum. © *2003 MAIK "Nauka/Interperiodica"*.

1. INTRODUCTION

Coronal mass ejections (CMEs) are the largest-scale phenomena of sporadic solar activity, which play an important, and frequently determining, role in various solar, interplanetary, and geophysical events (see, e.g., reviews [1–6] and references therein). While flares release energy stored in the local magnetic fields of active regions, the origin of CMEs is most likely rooted in the dynamics of large-scale magnetic fields, the global evolution of the solar magnetosphere, and the instabilities of individual magnetospheric structures, such as coronal streamers, prominences (filaments), large arcades, etc. Considerable progress in studying CMEs has been achieved in recent years, primarily due to Yohkoh [7] and SOHO [8] observations.

CMEs rising in the corona at velocities of up to 2000 km/s are observed in white light with the SOHO LASCO coronagraph [9] over the limb, at heliocentric distances of up to $30R_S$ (where R_S is the solar radius), due to the scattering of photospheric radiation by free electrons, whose density is substantially increased in the ejected material. In many cases, the CMEs far exceed the optical solar disk in size, even at small heliocentric distances. The transequatorial character and global scale of CMEs are visible, for example, in the association of the footpoints of loop transients observed in many big events with structures located in opposite (northern and southern) hemispheres of the Sun.

Observations of disk processes before, during, and after the eruption are very informative for studies of CMEs. High-quality images obtained with the Yohkoh SXT [10] and SOHO EIT [11] telescopes indicate that CME-related substantial restructurings and large-scale magnetic-field disturbances are most clearly manifest in so-called dimmings and coronal waves. Dimmings, or transient coronal holes [12–17], are regions of reduced soft X-ray and EUV intensity with lifetimes of several to several tens of hours that are formed after the CMEs near the eruption center—e.g, at the periphery of the sigmoid structure—and can cover a large portion of the solar disk. Analyses show [15, 16] that the most intense dimmings are observed simultaneously in several UV lines (FeIX/X 171 Å, FeXII 195 Å, FeXV 284 Å) that are sensitive to coronal plasma at temperatures of $(1.2–2.0) \times 10^6$ K, as well as in soft X-rays, corresponding to temperatures $>2.5 \times 10^6$ K. Therefore, dimmings can be interpreted as a result of the complete or partial opening of the magnetic fields in these structures, with the evacuation of material and a corresponding reduction in their intensity. Fairly frequently, a bright front can be observed ahead of the developing dimmings, indicative of a coronal or EIT wave traveling from the eruption center at a speed

1063-7729/03/4702-0139$24.00

of several hundred km/s [15,18–20]. According to one point of view [19, 21, 22], the EIT wave is a CME-initiated MHD disturbance—a coronal analog of the chromospheric Moreton wave observable in the H_α line [23]. Another interpretation [24, 25] is that the coronal wave is associated with the evolution of magnetic structures involved in the CME, in particular, with the compression of plasma at the advancing boundary of the dimming—a region of opening magnetic field lines.

It is currently believed that dimmings and coronal waves are mainly quasi-isotropic and propagate in a wide-angle sector more or less symmetrically with respect to the eruption center [15, 19, 21, 22]. At the same time, coronal waves are known to be reflected and refracted as they interact with the strong magnetic fields of active regions [26]; a dimming may encompass separate large-scale (including transequatorial) loops anchored in the eruption region [17–29]. In some cases, so-called twin dimmings are observed, with the strongest intensity decreases occurring in two regions adjacent to the eruption center and located symmetrically with respect to the polarity-reversal line and the posteruptive arcade [15, 16]. Such twin dimmings appear to be the footpoints of large-scale flux lope structures erupting during the CME. The eruptive events accompanied by coronal waves and dimmings currently described in the literature occurred primarily in 1997 and 1998, during the growth phase of the current activity cycle—a period when the global solar magnetosphere had a relatively simple structure.

We present here our analyses of the spatial structure of UV dimmings observed near the activity-cycle maximum, when the solar magnetosphere was fairly complex. Difference SOHO EIT heliograms obtained at 195 Å indicate that the eruption of a large CME against the background of several active regions and other features on the disk is accompanied by clearly defined, anisotropic, channel-shaped ("channeled") dimmings that develop along narrow, extended features (channels) and stretch between widely spaced activity centers that can cross the heliographic equator. Methodological questions connected with identifying dimmings are discussed in Section 2. Section 3 begins with a consideration of a quasi-isotropic coronal wave and dimming that are typical for a relatively simple large-scale magnetic-field structure. Further, we consider in detail the development and structure of dimmings observed during two halo CME events in January and February 2000 when the global solar magnetosphere had a complex structure. A discussion and concluding remarks are presented in Section 4.

2. METHODOLOGICAL NOTES

In analysis of the large-scale structure of dimmings, it is reasonable to consider halo CME events in which the eruption source is located in the central zone of the visible disk, and the earthward traveling CME is observed as a bright and expanding emitting region surrounding the entire occulting disk of the coronagraph [30]. It is reasonable to use SOHO EIT 195 Å data, because heliograms are taken with the highest cadence (normally, 12–20 min) just in this line [11]. Corresponding FITS files are available in the EIT cataloge at http://umbra.nascom.nasa.gov/eit/eit-catalog.html.

Studies of dynamic events on the solar disk, particularly events such as coronal waves and dimmings, are based on two types of difference images [15–18]. Running difference (RD) images are obtained by subtracting the preceding heliogram from the current heliogram. Fixed difference (FD) images are computed by subtracting a single pre-event image of the sun from all subsequent heliograms. In such difference images (Fig. 1), dimmings are manifest as dark features with reduced intensity, while coronal waves appear as bright advancing fronts.

There are substantial differences between the RD and FD images [in Fig. 1, panels (a) and (c) should be compared to (b) and (d)]. The RD images emphasize changes (in the brightness, localization, and structure of sources) that have occurred during the interval between contiguous frames. In particular, the front of the traveling coronal wave can be most clearly seen in the RD images. However, many artifacts unavoidably appear in the RD images. For example, dark features—spurious dimmings of a methodological origin—will be seen where there was a bright, advancing coronal-wave front and its fragments in the previous RD frame. A similar spurious dimming will appear in an RD image when the intensity of a bright feature decreases, in particular, if such a feature appears during a flare or posteruptive phase. Likewise, if the depth of a true dimming decreases with time, a spurious brightening will be seen in the next RD frame at the same place. If, however, the intensity of a true brightening or dimming remains nearly unchanged between contiguous frames, the corresponding feature will be completely missing from the RD image (the region will have the background intensity). The artifacts described above can be identified by scrutinizing the RD images in Figs 1a and 1c. In particular, many of the brightenings and dimmings visible behind the coronal-wave front in Figs 1a and 1c have a methodological origin and are due to the procedure used to obtain the RD images.

In FD images (Figs 1b, 1d), changes that occur during the event are clearly visible, in particular, those

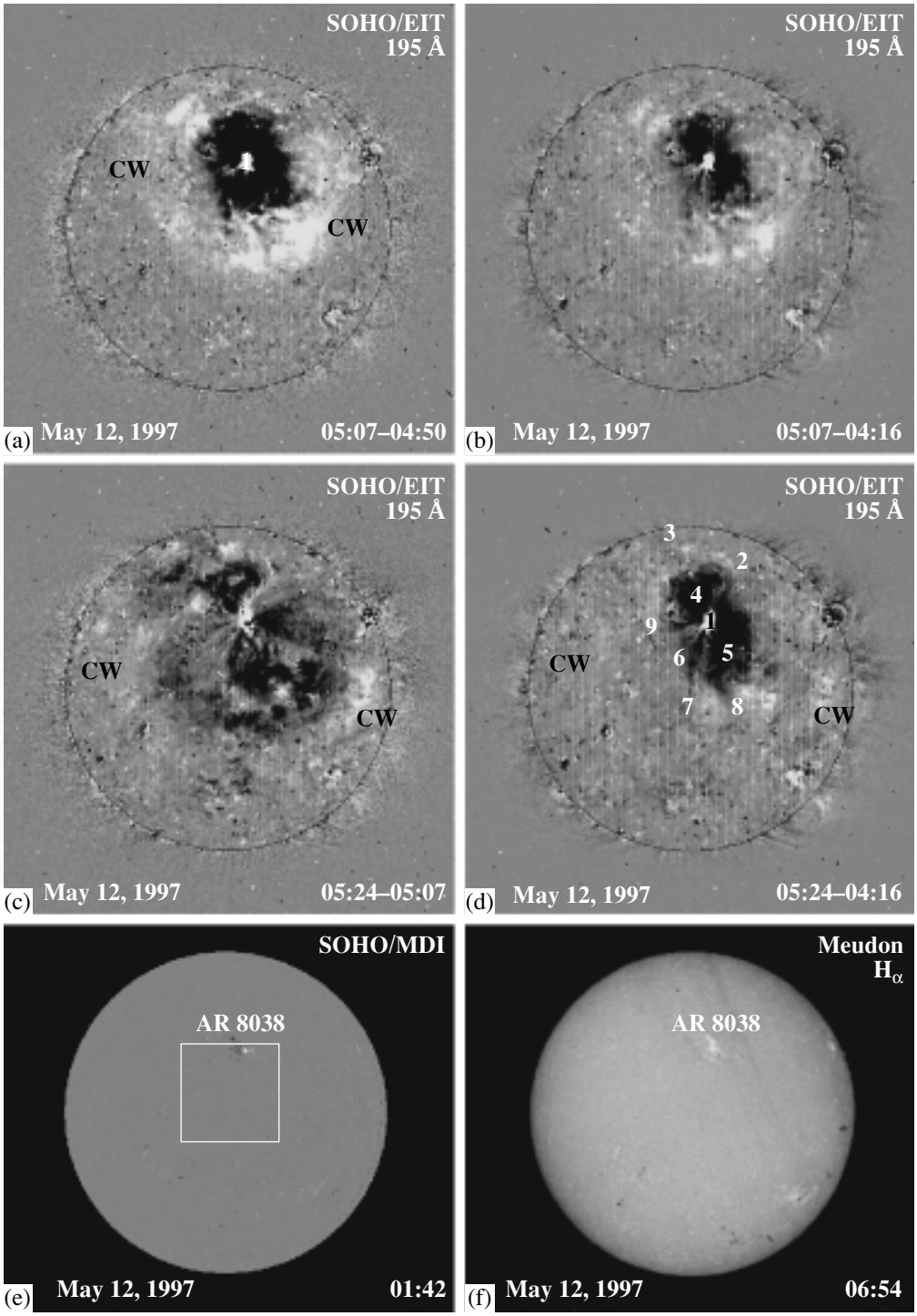

Fig. 1. (a, c) Running and (b, d) fixed difference images of the Sun in the 195 Å line (SOHO EIT). These illustrate the differences between the two image types and the quasi-isotropic character of the dimming and coronal wave (CW) after the halo CME of May 12, 1997. The (e) SOHO MDI magnetogram and (f) H_α heliogram demonstrate the presence of only one large active region on the disk.

related to coronal waves and dimmings (naturally, we mean here changes relative to the selected reference frame chosen before the event). However, the construction of FD images raises another problem, since solar rotation can also produce spurious features. In 512×512 SOHO EIT frames [11] with a pixel size of $5.24''$, the effect of rotation is virtually indistinguishable if the RD images are obtained by

subtracting images taken 12–20 min apart. However, the rotation of the solar surface becomes important if the interval between frames is several tens of minutes or several hours, as in the case of constructing FD images. In particular, it is clear that the angular displacement of a dark feature observed in absorption will give rise to a spurious bright edge in the difference image to the east of this feature. In contrast, a bright feature observed in emission will produce a dark eastern edge resembling a dimming. This effect is especially pronounced for narrow, meridionally stretched features, e.g., vertical filaments and transequatorial loops, when the longitudinal extent of the spurious edge is comparable to the size of the feature itself. To suppress the formation of spurious features, we introduced corrections to compensate for the solar rotation before constructing the difference images, aligned the heliograms, and reduced them to a unified calibration. As a rule, all the frames considered were rerotated to the time of the same reference (pre-event) heliogram, which was subtracted from the subsequent frames to obtain the FD images. For example, this time is 04:16 UT for Figs. 1b and 1d.

In this study, we will analyze dimmings using FD images with a preliminary compensation for solar rotation. We will use RD images as an additional source of information to examine some changes detected in the FD heliograms in more detail. In this context, the most effective tool for the analysis and representation of data is computer movies composed of difference images and viewed in JAVA format with adjustable frame rate and playing direction. Some examples of such movies, as well as other illustrations of CMEs related to the events considered, can be found at http://helios.izmiran.troitsk.ru/lars/Chertok/dimming/index.html.

The following important point deserves particular attention. The dimmings analyzed here and, especially, individual fragments of their large-scale structure, as well as many coronal waves, are relatively faint phenomena (see below). For this reason, we have limited the intensity range in the difference images in order to make these features sufficiently pronounced. As a result, the brightest sources (particularly those emerging during flares), which are not the subject of our analysis, are saturated. A similar approach has been used to identify large-scale emitting chains in microwave, UV, and X-ray heliograms [31]. For example, the brightness cutoffs for the RD and FD images shown in Fig. 1 are ± 75 and ± 150 count/pixel, respectively. Similar intensity ranges were used for the other events under study. Naturally, the outlines and some structural details of dimmings and coronal waves vary to some extent depending on the chosen intensity range. Finally, we note that, if the time interval between the current and reference heliograms is long, regular vertical strips of an instrumental origin can be detected in high-sensitivity FD images (Fig. 1d).

In the SOHO EIT images, periodic vertical and horizontal light strips due to the properties of the CCD matrix used are not uncommon [11]. Rotation of the solar image does not affect the positions of the horizontal strips but displaces the vertical strips. For this reason, the subtraction of images suppresses the horizontal strips and enhances the vertical ones. Since the rotation is performed only for a spherical surface, this instrumental and methodological effect, which is exaggerated by the intensity cutoff, is present only on the solar disk.

3. ANALYSES OF PARTICULAR EVENTS

3.1. Event of May 12, 1997

We restrict ourselves to brief remarks about this event, since it is well known and is described in detail in the literature [15, 17, 32, 33]. We present it here as an illustration of CME-related disturbances that occur under relatively simple conditions in the global solar magnetosphere; Fig. 1, which refers to this event, was already used in the discussion of the analysis techniques (Section 2).

The eruption source was located in AR 8038 (N21 W09), which was essentially the only active region on the solar disk at that time. This can be seen from the SOHO MDI magnetogram and H_α heliogram of the Observatoire de Paris shown in Figs 1e and 1f. As far as other significant features are concerned, only the northern and southern coronal holes (CHs) could be observed on the disk in soft X rays with the Yohkoh SXT telescope and were present in the original UV heliograms taken in the 195 and 284 Å lines [15]. This event was associated with a long-duration flare of class 1F/C1.3 with its maximum near 04:50 UT. The CME recorded by the SOHO LASCO coronagraph was classified as a full halo emitting everywhere around the occulting disk, but its brightness was maximum over the eastern, western, and northern limb sectors [32].

The eruption of the CME was accompanied by pronounced, large-scale transient disturbances on the disk, in particular, a coronal wave and dimmings [13]. The difference heliograms obtained at 195 Å (Fig. 1) show that the coronal-wave front had a fragmentary structure but traveled more or less isotropically with respect to the eruption center 1. The front's propagation decelerated only as the northern polar CH was approached, and the interaction of the front with the CH gave rise to the long emitting chain 2–3 (Fig. 1d), which gradually encompassed the entire CH boundary and was observed over several

hours. Before its interaction with the CH, the coronal wave propagated over the solar surface at nearly the same velocity, 240 km/s, in all directions [15]. The halo CME had a similar velocity in the plane of the image [32].

The two deepest, symmetric twin dimmings with similar sizes and shapes (4, 5) formed northeast and southwest of the eruption center and were clearly visible in at least three UV lines—171, 195, and 284 Å—as well as in soft X rays [15]. It is important that, during the entire event, these intense dimmings were surrounded by a much weaker dimming region, which completely filled the space between the dimmings (4, 5) and the traveling quasi-isotropic coronal wave. Therefore, the weak dimming was also quasi-isotropic. It can be distinguished in two UV images (Figs. 1b, 1d), but is most pronounced in Fig. 5c in [17].

Thus, in this case, both the coronal wave and the dimmings were quasi-isotropic and covered the visible hemisphere almost entirely. It is likely that this character for the transient disturbances was due to the fact that only one active region was present on the disk at that time, so that the structure of the solar magnetosphere was fairly simple. In any case, as will be shown below, dimmings observed under more complex conditions are appreciably anisotropic and take the form of long, narrow features (channels). In fact, some signatures of such channels can be detected in the May 12, 1997 event; in particular, short dimming branches (1–6–7, 6–8, 1–9) can be distinguished in Fig. 1d.

3.2. Event of January 18, 2000

This event occurred when several active centers, filaments, and CHs were observed on the disk (Figs. 2e, 2f), so that the structure of the global solar magnetosphere was fairly complex. The event included a long-duration class 1N/M3.9 flare in region AR 8831 (S19 E11), with a maximum at 17:27 UT and a structured halo CME, which initially developed over the eastern limb and subsequently extended to all position angles.

The FD images at 195 Å obtained using a reference heliogram of 16:48 UT and shown in Figs 2a–2d demonstrate that, by 17:24 UT (Fig. 2a), a narrow transequatorial strip dimming formed along with an annular dimming surrounding the eruption center 1; the strip extended to region 2 in the southern half of the disk near the central meridian. In the next frame at 17:36 UT (Fig. 2b), this strip extends further westward to point 3. The dimming channel 1–4 going from the eruption center to the southeastern limb also becomes visible. A relatively faint branch of the dimming 5–6–7 forms to the west of AR 8831 and is linked by the brightened loop 6–8 to the southwestern region, where another remote dimming center can be distinguished. The faint dimming 6–9 stretches to the southern limb region.

Subsequent frames, including the frame of 18:12 UT (Fig. 2c), clearly demonstrate the southeastern dimming loop 1–10, which may extend to limb 11. Furthermore, another, eastern, transequatorial dimming feature 12–13–14 can be distinguished, extending toward the active region located in the northeastern quadrant. The main eastern and western transequatorial dimming branches are linked by additional dimming features: one or two narrow strips of the dimming 2–14 pass near the central and northeastern activity complexes of the northern hemisphere (having extensions from region 14 in the form of narrow eastward and southeastward offshoots); another, more diffuse and possibly looplike dimming system 13–15 is located near the central meridian and joins the bright dimming 15–6, which fringes the eruption center from the north and northwest.

Virtually all these elements of channeled dimmings are also present in the last frame presented, of 18:36 UT (Fig. 2d). Note also the emergence of the relatively faint dimmings 14–16 and 17–18 stretching to the northeastern limb. The narrow dimming 10–11 going southward from the southeastern dimming loop can also be seen.

The relative depths and temporal changes in different portions of the channeled dimmings can be seen in Fig. 3. Selected $53'' \times 53''$ areas of various structures of dimming features (1–5) are marked in the heliogram (Fig. 3a), together with the region of the southern CH (6) for comparison. The corresponding time-variation profiles shown in Fig. 3b indicate that the intensity reduction in main dimmings that are both adjacent to the eruption center and channel-shaped is 25–80%. In area 4, some increase in intensity can be noted after a relatively brief, deep dimming. Curve 6 confirms that the dimming does not involve the southern polar CH. As can be seen from Fig. 3b, the development time for dimmings, including channeled dimmings, is several tens of minutes. The total lifetime of channeled dimmings can reach several hours.

We can note the following in connection with the identification of these large-scale channeled dimmings with observed coronal and photospheric features, based on a comparison of the difference images in Fig. 2a–2d with the H_α heliogram (Fig. 2e) and the original background (negative) image at 195 Å (Fig. 2f). The two main transequatorial dimming channels, 1–2 and 12–13–14, seem to coincide with the looplike transequatorial features observed at

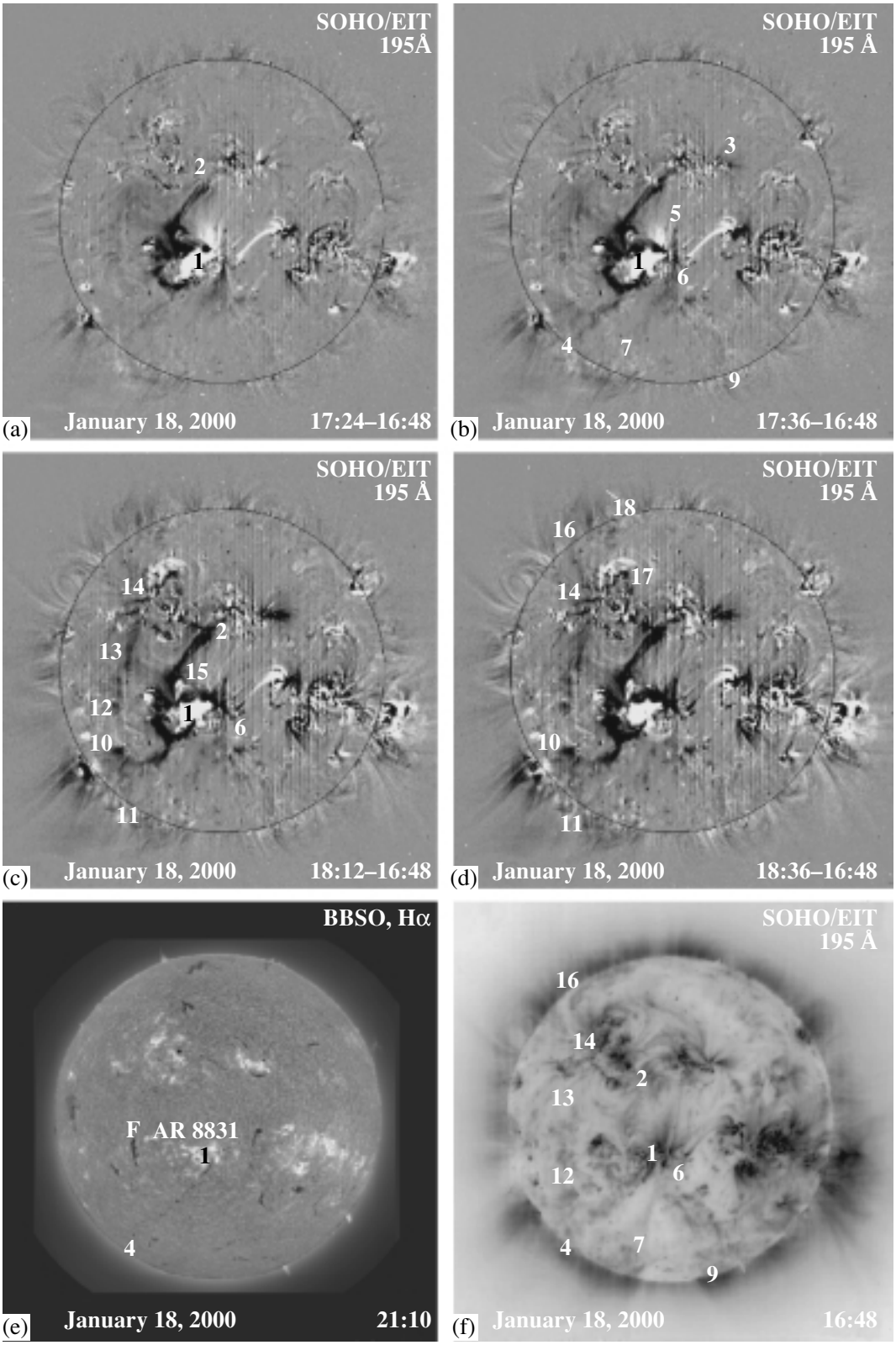

Fig. 2. (a–d) Fixed difference solar images in the 195 Å line for January 18, 2000 (SOHO EIT) obtained by subtracting the heliogram of 16:48 UT. These illustrate the halo-CME-related development of channeled dimmings with the presence of several activity centers on the disk. Bottom panels: (e) H_α heliogram; (f) original base (negative) image at 195 Å.

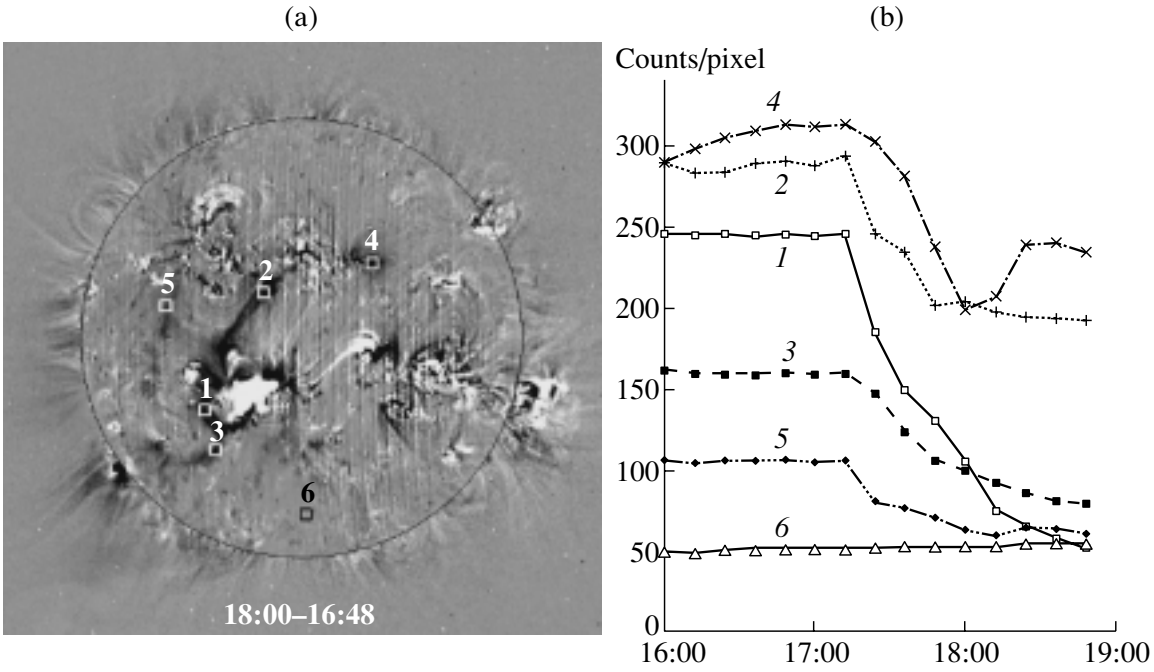

Fig. 3. (b) Time variation of the intensity in the 195 Å line during the event of January 18, 2000, for several 53″ × 53″ areas shown in panel (a): (*1–5*) in channeled dimmings and (*6*) in the southern coronal hole. The instrumental background has been subtracted.

195 Å and labeled by the same numbers in Fig. 2f. In addition, dimming 1–4 corresponds to the channel of the southeastern H_α filament (Fig. 2e), while dimmings 6–7, 6–9, and 14–16 are located along the western and eastern boundaries of the southern polar CH and the western boundary of the northeastern CH, respectively. Note that the H_α filament F (Fig. 2e), which is closest to the eruption center and is surrounded by dimming channels, did not exhibit obvious signatures of a disturbance related to this eruptive event.

It is characteristic of this event that no extended and bright coronal-wave front (in the usual sense) can be seen in either the FD or the RD movies, much less in the corresponding images. Instead, something like a dimming wave is observed: individual dimming channels and the entire region covered by dimmings become more extended with time. As this takes place, a few irregular, transient brightenings with small areas and intensities adjoin the dimming features. Estimates that can be obtained with a large interval between frame rate indicate that the propagation speed of this dimming wave is several hundred km/s, typical of classic bright coronal waves (see Section 3.1). It is important that the dimming wave in this event spread from the eruption center mainly eastward, northward, and southward, but essentially did not intersect the central meridian; i.e., it was not spherically symmetric.

3.3. Event of February 17, 2000

Among other things, this event is interesting because it occurred one solar rotation after the preceding one and at nearly the same site on the solar surface (Section 3.2), with the same complexity of the global solar magnetosphere. It developed against the background of two sympathetic flares of classes M2.5/1B and M1.3/2N, which occurred in the nearby active regions in the southern hemisphere AR 8869 and AR 8872 (S25 W16 and S29 E07; Fig. 4e) and reached their maxima in soft X rays at 18:52 and 20:35 UT, respectively. A number of arguments based on the optical, magnetic, UV, and X-ray data [34] suggest that the first flare initiated the second and that the two active regions were interconnected by magnetic structures. The annular transequatorial system of emitting chains 1–5–3–7–8–9–10–6, which can be seen in the processed SOHO EIT heliogram at 195 Å (Fig. 4f; a negative), indicates that this connection had a global character and encompassed all active regions located in the central sector of the disk [31]. According to the SOHO LASCO coronagraph data, the first manifestations of a CME were observed over the southwestern limb at 19:31 UT, and a symmetric halo CME developed around the entire occulting disk after 20:06 UT. This symmetric CME configuration seems to reflect the fact that, as will be shown below, the eruption process involved a similarly shaped, circular central region of

the disk depicted by the chain 1–5–3–7–8–9–10–6, together with the system of channeled dimmings that can be seen in the FD images (Figs. 4a–4d) and corresponding movies.

During the first flare, the connection between regions AR 8869 and AR 8872 was marked by two dimming structures (Fig. 4a). One was relatively wide and connected the western extremity of dimming 1, flare brightening 2, and the eastern region 3, and extended to the southeast in the form of the narrow channel 3–4. The other was a narrow arc, 1–5–3, and curved around the flare region from the south. Furthermore, at this stage, a faint dimming encompassed the entire central region of the disk between regions 2, 3, 7, 8, 9, 10, and 6. The somewhat deeper but nevertheless faint transequatorial dimming channels 1–9, 3–9, and 6–10 stood out against this background. Channels 1–9, 6–10, and dimmings 7–8, 8–9 were seen at a late stage of the first flare (Fig. 4b). By that time, flare brightening 2 increased its longitudinal extent, and the first signs of the second flare appeared in region 3; the wide dimming 2–3 between the interacting active regions almost vanished, while channel 2–11 connecting the brightening 2 with the southern arclike dimming 1–5–3 became more pronounced.

The second flare was accompanied by the emergence of new dimmings around the bright feature 3 (Fig. 4c). The looplike dimming systems 12 and 13 formed to the northeast and south of this feature. The western base of these dimming systems abutted on region 11, through which passed the narrow channel related to the first flare 2 and the enhanced eastern branch 3–5 of the arclike dimming 1–5–3. The well-defined dimming channel 3–14 with several branches formed north of the flare region, in the direction of region 9. Substantial enhancements were observed in many channeled dimmings localized in the central zone of the disk, including areas between the regions 3–8, 8–9, 1–9, and 1–10. All these dimming features developed further in the final stage of the event (Fig. 4d). In particular, the continuation of the brightest transequatorial channel 3–14 toward region 9 became quite prominent. The depth of the dimmings situated to the south of this region and those stretching to the eastern region 8 increased substantially. The emergence of dimmings going from the second flare brightening 3 to the southeastern limb 15 (with branching from point 16 to region 7) and to the southern limb 17 (with a deep dimming center observable outside the solar disk) was noted. Toward this same region, dimming 5–17 stretched from the area of the first flare through the western part of the arclike channel 1–5. Channeled dimmings formed east of regions 7 and 8, reaching points 18, 19, and 20. Narrow dimmings can also be seen between regions 1, 10 and 7, 8. Dimming fragments are visible between region 9 and the northern limb 21.

Curves describing the development and depth of the dimmings within several key $53'' \times 53''$ areas are shown in Fig. 5. We can clearly see a time lag between the emergence of the dimmings related to the first and second flares. The first flare was accompanied by the onset of dimmings at about 19 UT in areas 1, 2, and, partially, 3. Significant dimmings are related to the second event, beginning at 20:20–20:40 UT in areas 5 and 6 related to the meridional channel, in the southern area 4, and again in area 3. The onset of the dimming in the northern area 6 was appreciably delayed. Curve 7, which is shown for comparison and verification purposes, demonstrates a smooth intensity decrease in the area over the southwestern limb, which does not seem to be related to the dimmings considered here. As in the preceding event, the depths of the main and channeled dimmings are tens of per cent, while the development time comprises several tens of minutes.

A comparison of the dimmings described above (Figs. 4a–4d) and the background heliogram at 195 Å (Fig. 4f; a negative) shows that the locations and configurations of most of the channeled dimmings correspond to elements of the annular system of emitting chains 1–5–3–8–9–10–6, which was observed prior to the event in the central portion of the disk. The deepest dimmings appeared precisely in the regions where the preflare UV features had been brightest. For example, the southern arclike dimming channel 1–5–3 coincided with the corresponding bright chain between two flare regions. The deepest portions of the transequatorial dimming 3–9 and adjacent branches can be identified with features of increased intensity in the neighborhood of the southern and northern active regions. The diagonal dimming 1–9, as well as the eastern and western meridional dimmings 7–8 and 1–10, were located at the sites of corresponding UV features. The dimming fragments localized outside the central zone and extending southward from the flare regions 2 and 3, eastward from regions 7 and 8, and northward from region 9 also had counterparts in the background heliogram, in the form of features of increased intensity.

It is clear from these data that, as in the preceding case, the disturbances related to the halo CME under consideration were global and anisotropic. This is true not only of the dimmings, but also of the coronal wave. As indicated by the movies of the FD and RD images, some manifestations of the coronal wave and traveling dimmings can be detected only within the southern sector bounded by elements 3–16–15 and 5–17 (Fig. 4d). In addition, modest-sized, fragmentary brightenings accompanied the development of

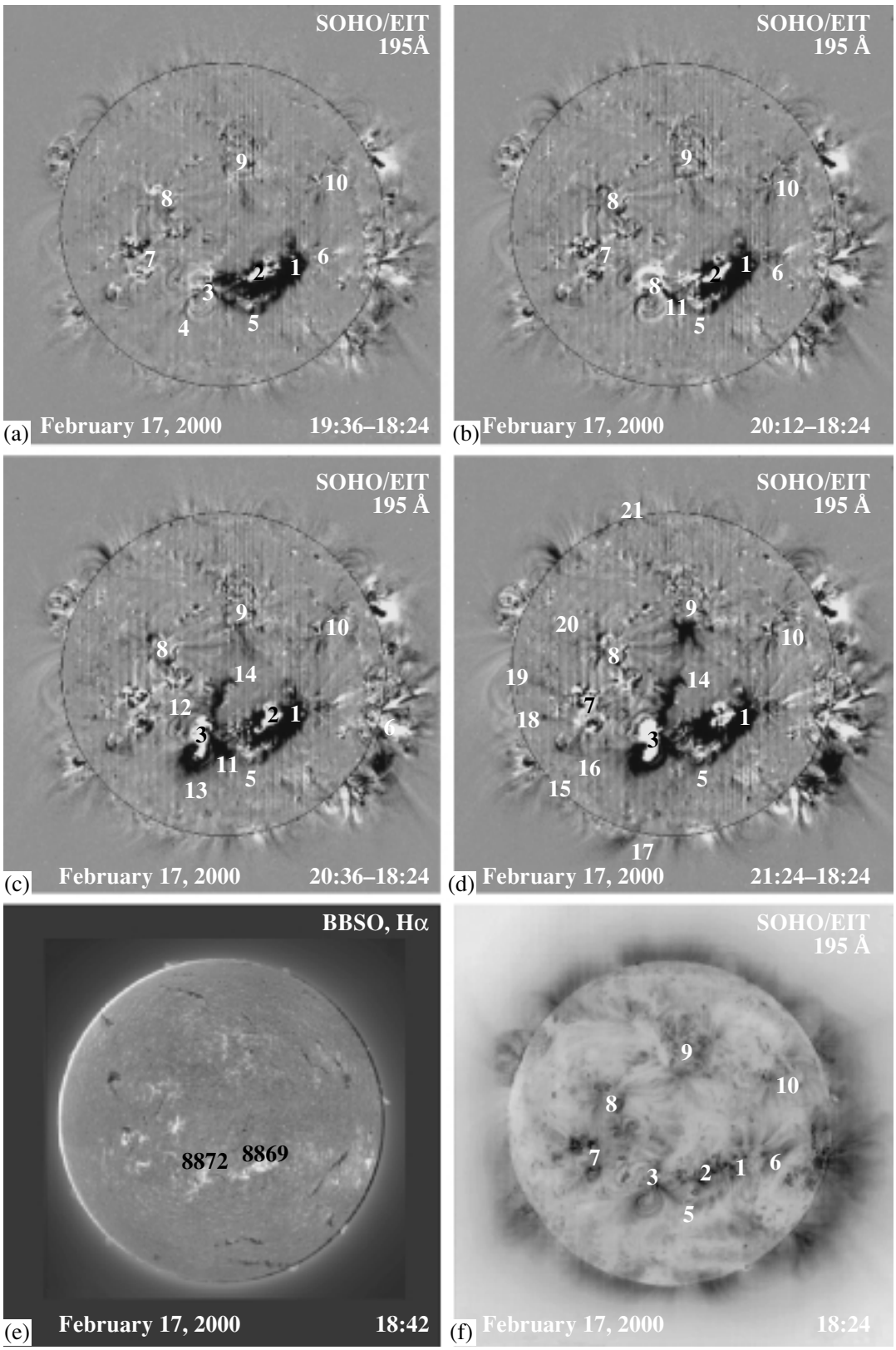

Fig. 4. (a–d) Fixed difference solar images in the 195 Å line for February 17, 2000 (SOHO EIT) obtained by subtracting the heliogram of 18:24 UT. These illustrate the development of channeled dimmings after the halo CME and two sympathetic flares. Bottom panels: (e) H_α heliogram; (f) original base (negative) image at 195 Å.

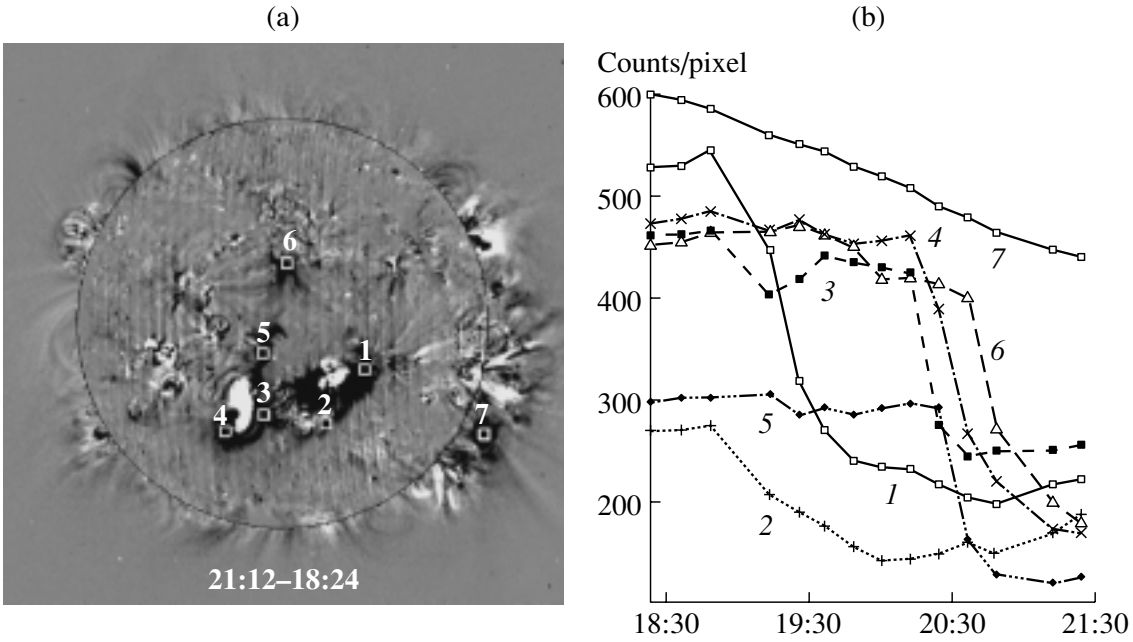

Fig. 5. (b) Time variation of the emission intensity in the 195 Å line during the event of February 17, 2000, for several 53″ × 53″ areas shown in panel (a): (*1*, *3*, *4*) in dimmings adjacent to the flare centers and (*2*, *5*, *6*) in channeled dimmings. For comparison and verification purposes, the intensity variation in region (*7*) over the southwestern limb is also shown. The instrumental background has been subtracted.

the transequatorial dimmings 1–9 and 3–9 in the central zone of the disk.

4. DISCUSSION AND CONCLUSION

Our analysis of the difference UV SOHO EIT heliograms (primarily the FD images) at 195 Å suggests the following properties of halo-CME-related, large-scale solar dimmings and coronal waves.

There are events in which isotropic dimmings and coronal waves are observed developing more or less symmetrically in all directions from the eruption center [15, 17].

Here, we have identified events with pronounced anisotropic dimmings localized along a number of narrow, extended structures—channels.

Such channeled dimmings extend between widely separated activity centers, including those located on either side of the heliographic equator, and cover the visible solar disk almost entirely; in other words, they are global disturbances.

The reduction in the intensity of EUV emission in many dimming channels is comparable to that in isotropic dimmings and reaches several tens of per cent.

Channeled dimmings develop within several tens of minutes and can exist for several hours, as do dimming elements around eruption centers.

In channeled-dimming events, bright coronal waves are either not observed at all or are also anisotropic and propagate within a restricted sector of the disk. In some cases, a wave of dark dimmings is observed instead of a bright coronal wave.

Estimates based on the available data indicate that the propagation speeds of both channeled dimmings and coronal waves are several hundred km/s.

The appearance of isotropic or channeled dimmings apparently depends on the level of complexity of the global solar magnetosphere.

Isotropic dimmings and coronal waves are observed when the structure of large-scale magnetic fields is simple, when only one activity center present on the solar disk.

In contrast, channeled dimmings and anisotropic coronal waves are typical of complex structures of the global solar magnetosphere, with the presence of several active regions, filaments, coronal holes, etc. on the disk.

Only preliminary remarks about the identification of dimming channels with coronal structures can be made at this time. It is obvious that channeled dimmings outline or curve around existing large-scale coronal structures. Some dimming channels appear to coincide with pre-CME looplike transequatorial emission features observed in the same line, 195 Å, between widely separated active regions. A similar halo-CME-related reduction in the intensity

of transequatorial X-ray and UV loops was noted in [27] (see also [22, 28, 29]). In some cases, channeled dimmings arise at the scene of large-scale emitting UV chains [31]. Such channeled dimmings can probably be regarded as transient chains in absorption. Extended dimmings may also be aligned with the H_α filament channel. Just as coronal waves avoid active regions [26] and stop in front of CHs [15], channeled dimmings do not penetrate into CHs, and remain localized along their boundaries.

The detected channeled dimmings provide additional evidence that widely separated active regions and other features, including those situated in different solar hemispheres, are integrated into a single, complex system that forms the global solar magnetosphere. Large-scale emission chains also provide evidence for this idea, and some seem to trace out quasi-separatrix layers between different interacting magnetic fluxes in the global solar magnetosphere (see [31]).

The observations clearly indicate that, during a major CME, a substantial portion of the global solar magnetosphere becomes involved in the eruption process within several tens of minutes. This probably refers first and foremost to structures that are directly magnetically linked to the eruption center [29]. It is also not ruled out that these phenomena are induced by an MHD disturbance that spreads from the eruption center and is identified as a coronal wave.

It is obvious that the deepest dimmings affect structures that had fairly high emission measures and were sources of enhanced emission before the eruption. Dimmings and dimming channels demonstrate the presence of well defined coronal features and extended structures in the complex global solar magnetosphere, which exhibit the most pronounced CME-related intensity decreases. Such decreases could result from a partial or complete opening of the magnetic field lines in the process of the CME, with an associated evacuation of material. Another possibility is that an originally isotropic MHD disturbance affects these structures. It is likely that one or the other (or both) of these factors—the opening of field lines or an MHD disturbance—operate in specific events or in specific regions of the global solar magnetosphere.

On the whole, we can conclude that channeled dimmings are an important consequence and indicator of strong disturbances and substantial restructurings of large-scale features of the global solar magnetosphere in the corona during and after a CME. Further analyses are needed to gain a more comprehensive understanding of the nature of channeled dimmings and their role in CME processes.

5. ACKNOWLEDGMENTS

We are grateful to the SOHO EIT and LASCO teams, as well as the staffs of the Big Bear and Meudon observatories, for making available the data used for the analyses. This work was supported by the Russian Foundation for Basic Research (project nos. 00-15-96661, 00-15-96710, 00-02-16090, and 00-02-16819) and partially supported by the Ministry of Industry, Science, and Technologies of the Russian Federation.

REFERENCES

1. I. M. Chertok, Astron. Zh. **70**, 165 (1993) [Astron. Rep. **37**, 87 (1993)].
2. A. J. Hundhausen, in *The Many Faces of the Sun,* Ed. by K. Strong *et al.* (Springer-Verlag, New York, 1999), p. 143.
3. D. F. Webb, J. Atmos. Sol.-Terr. Phys. **62**, 1415 (2000).
4. M. D. Andrews and R. A. Howard, Space Sci. Rev. **95**, 147 (2001).
5. H. S. Hudson and E. W. Cliver, J. Geophys. Res. **106**, 25199 (2001).
6. J. A. Klimchuk, in *Space Weather,* Ed. by P. Song, H. Singer, and G. Siscoe (AGU, Washington, 2001), Geophysical Monograph, No. 125, p. 143.
7. Y. Ogawara, T. Takano, T. Kato, *et al.*, Sol. Phys. **136**, 1 (1991).
8. V. Domongo, B. Fleck, A. I. Poland, *et al.*, Sol. Phys. **162**, 1 (1995).
9. G. E. Brueckner, R. A. Howard, M. J. Koomen, *et al.*, Sol. Phys. **162**, 357 (1995).
10. S. Tsuneta, L. Acton, M. Bruner, *et al.*, Sol. Phys. **136**, 37 (1991).
11. J.-P. Delaboudinière, G. E. Artzner, J. Brunaud, *et al.*, Sol. Phys. **162**, 291 (1995).
12. D. M. Rust, Space Sci. Rev. **34**, 21 (1983).
13. A. C. Sterling and H. S. Hudson, Astrophys. J. **491**, L55 (1997).
14. H. S. Hudson and D. F. Webb, in *Coronal Mass Ejections,* Ed. by N. Crooker, J. Joselyn, and J. Feynman, AGU Geophysical Monograph Series, No. 99, 27 (1997).
15. B. J. Thompson, S. P. Plunkett, J. B. Gurman, *et al.*, Geophys. Res. Lett. **25**, 2465 (1998).
16. D. M. Zarro, A. C. Sterling, B. J. Thompson, *et al.*, Astrophys. J. **520**, L139 (1999).
17. N. Gopalswamy and B. J. Thompson, J. Atmos. Sol.-Terr. Phys. **62**, 1427 (2000).
18. B. J. Thompson, J. B. Gurman, W. M. Neupert, *et al.*, Astrophys. J. **517**, L151 (1999).
19. A. Klassen, H. Aurass, G. Mann, *et al.*, Astron. Astrophys. **141**, 357 (2000).
20. D. A. Biesecker, D. C. Myers, B. J. Thompson, *et al.*, Astrophys. J. **569**, 1009 (2002).
21. B. J. Thompson, B. Reynolds, H. Aurass, *et al.*, Sol. Phys. **193**, 161 (2000).
22. A. Warmuth, B. Vršnak, H. Aurass, *et al.*, Astrophys. J. **560**, L105 (2001).

23. G. E. Moreton and H. E. Ramsey, Publ. Astron. Soc. Pac. **72**, 357 (1960).
24. C. Delannée and G. Aulanier, Sol. Phys. **190**, 107 (1999).
25. C. Delannée, Astrophys. J. **545**, 512 (2000).
26. L. Ofman and B. J. Thompson, Astrophys. J. **574**, 440 (2002).
27. J. I. Khan and H. S. Hudson, Geophys. Res. Lett. **27**, 1083 (2000).
28. S. Pohjolainen, D. Maia, M. Pick, *et al.*, Astrophys. J. **556**, 421 (2001).
29. T. Wang, Y. Yan, J. Wang, *et al.*, Astrophys. J. **572**, 580 (2002).
30. G. E. Brueckner, J.-P. Delaboudinière, R. A. Howard, *et al.*, Geophys. Res. Lett. **25**, 3019 (1998).
31. I. M. Chertok, Sol. Phys. **198**, 367 (2001).
32. S. P. Plunkett, B. J. Thompson, R. A. Howard, *et al.*, Geophys. Res. Lett. **25**, 2477 (1998).
33. D. F. Webb, R. P. Lepping, L. Burlaga, *et al.*, J. Geophys. Res. **105**, 27251 (2000).
34. H. Wang, V. Yurchyshyn, J. Chae, *et al.*, Astrophys. J. **559**, 1171 (2001).

Translated by A. Getling

Astronomy Reports, Vol. 47, No. 2, 2003, pp. 151–160. Translated from Astronomicheskiĭ Zhurnal, Vol. 80, No. 2, 2003, pp. 175–185.

Pre-Flare Changes in the Turbulence Regime for the Photospheric Magnetic Field in a Solar Active Region

V. I. Abramenko

Crimean Astrophysical Observatory, National Academy of Sciences of Ukraine, p/o Nauchnyi, Crimea, 334413 Ukraine

Received June 4, 2002; in fianl form, August 21, 2002

Abstract—Observations of the total magnetic field in the active region NOAA 6757 have been used to study the turbulence regime from 2.5 h before the onset of a 2B/X1.5 flare until two minutes after its maximum. The curvature of the exponent $\zeta(q)$ for the structure functions of the B_z field increases monotonically before the flare (i.e., the multifractal character of the B_z field becomes more complex) but straightens at the flare maximum and coincides with a linear Kolmogorov dependence (implying a monofractal structure for the B_z field). The observed deviations of $\zeta(q)$ from a Kolmogorov line can be used for short-term forecasting of strong flares. Analysis of the power spectra of the B_z field and the dissipation of magnetic-energy fluctuations shows that the beginning of the flare is associated with the onset of a new turbulence regime, which is closer to a classical Kolmogorov regime. The scaling parameter (cancellation index) of the current helicity of the magnetic field, k_h, remains at a high level right up until the last recording of the field just before the flare but decreases considerably at the flare maximum. The variations detected in the statistical characteristics of the turbulence can be explained by the formation and amplification of small-scale flux tubes with strong fields before the flare. The dissipation of magnetic energy before the flare is primarily due to reconnection at tangential discontinuities of the field, while the dissipation after the flare maximum is due to the anomalous plasma resistance. Thus, the flare represents an avalanche dissipation of tangential discontinuities. © *2003 MAIK "Nauka/Interperiodica"*.

1. INTRODUCTION

The energetic basis for nonstationary processes in the solar atmosphere—flares, giant mass ejections, explosions of filaments, and so on—is the transformation of magnetic-field energy into the kinetic energy of accelerated charged particles [1, 2]. The reconstruction of the magnetic-field structure results in instabilities in the atmosphere, magnetic reconnection, and explosions. Precursors of nonstationary phenomena associated with changes in the structure of the magnetic field have been sought for many years. Large-scale processes in active regions, such as the rising of new magnetic flux [3, 4] and shear motions in the photosphere [5, 6], are often followed by flares. On the other hand, the small-scale structure of the magnetic field in the active region probably also experiences some characteristic variations before a flare. The magnetized photospheric plasma is in a state of well-developed turbulence, since the corresponding Reynolds number is very large, on the order of 10^8 [7]. If, in accordance with the hypothesis of Parker [8–10], chaotic motions of the feet of magnetic tubes at the photospheric level are related to flare processes, then the parameters of the turbulence of the photospheric fields should be sensitive to the onset of flares.

As was shown in [11–14], increased flare activity of a group is followed by a decrease in the coefficient k_h characterizing the mutual compensation of the opposite polarities of the current helicity. Furthermore, we demonstrated in [15] that certain turbulence parameters of the longitudinal magnetic field in the photosphere are closely related to the level of flare activity of a group. In particular, we found for the eight active regions studied in [15] that, the higher the magnitude of the most powerful flare in the group (during the

Table. Parameters of the magnetic-field turbulence and characteristics of the flare in NOAA 6757 on August 2, 1991.

UT	$\zeta(6)$	Δh	β	τ	α	k_h
00:36	2.40	0.080	−1.40	−1.09	−2.49	0.788
02:00	2.17	0.073	−1.17	−0.76	−2.31	0.741
02:39	1.75	0.193	−0.75	−0.55	−2.22	0.750
03:07	Beginning of the flare 2B/X1.5					
03:15	Maximum of the flare 2B/X1.5					
03:17	1.99	0.035	−0.99	−0.65	−1.98	0.677

1063-7729/03/4702-0151$24.00

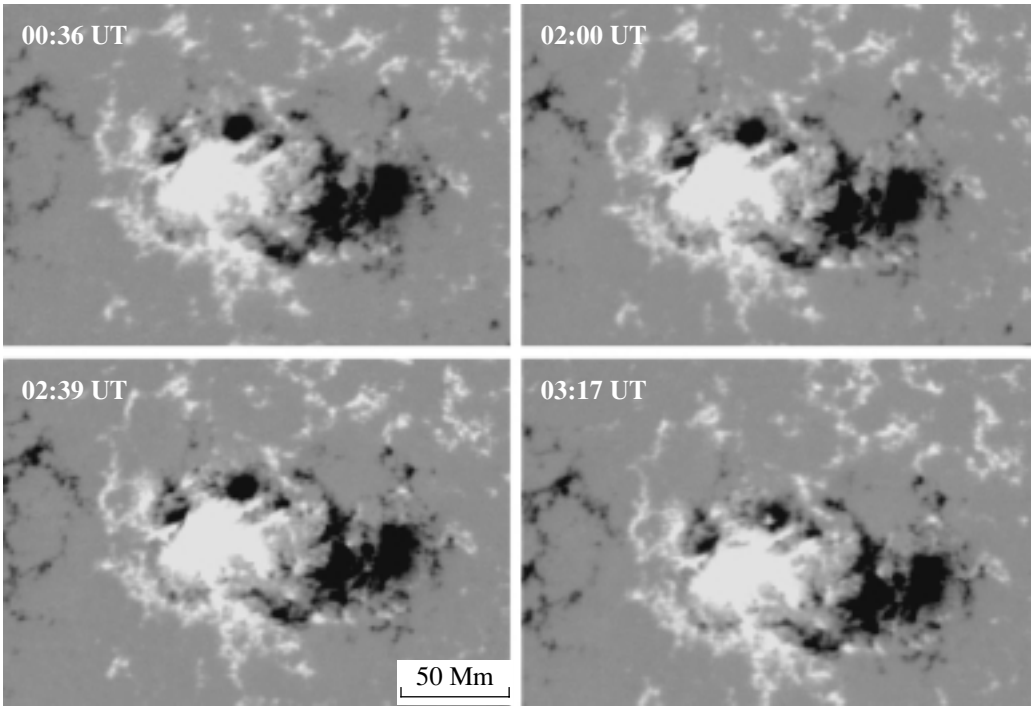

Fig. 1. Magnetograms of the B_z field in the active region NOAA 6757 on August 2, 1991, obtained by the Huairou Solar Observing Station of the Beijing Astronomical Observatory. North is at the top and west is to the right.

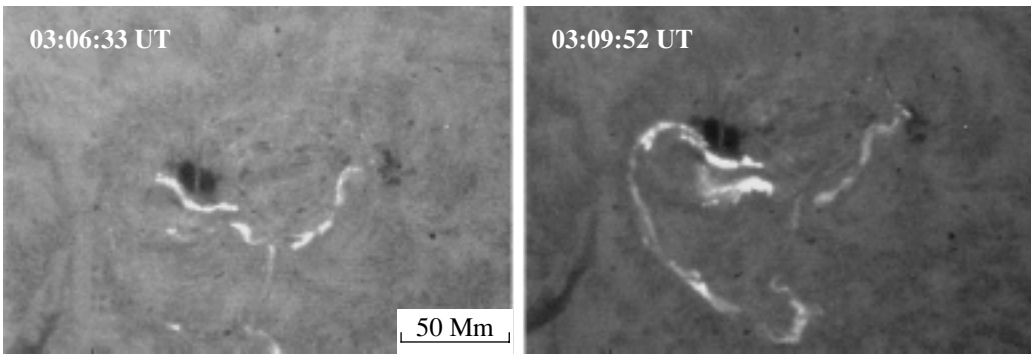

Fig. 2. Flare of magnitude 2B/X1.5 detected by the Huairou Solar Observing Station in the H_β line.

period of its motion over the disk), the greater the curvature of the plot of the structure-function exponent derived from the longitudinal magnetic field. This conclusion has stimulated us to study variations in the structure function for an active region before the flare, as well as corresponding variations of other parameters of the turbulence. This task can be formulated more generally: do the approach and onset of a powerful flare affect the turbulence characteristics of the photospheric magnetic field? Precisely this is the subject of the current paper.

We shall use the method for calculating and analyzing the structure functions of the B_z magnetic-field component developed in [15], the method for calculating power spectra and their exponents of [16, 17], and the method for calculating the coefficient k_h (the cancellation index) of the current helicity of the magnetic field described in [11, 18].

2. OBSERVATIONAL DATA ON THE ACTIVE REGION NOAA 6757

The active region NOAA 6757 was located near the disk center (N18, E18.7) on August 2, 1991. Measurements of the total magnetic-field vector were obtained by the Huairou Solar Observing Station (HSOS) of the Beijing Astronomical Observatory (China) using a videomagnetograph [19] in the FeI 532.4 nm line. The resolution of the CCD camera

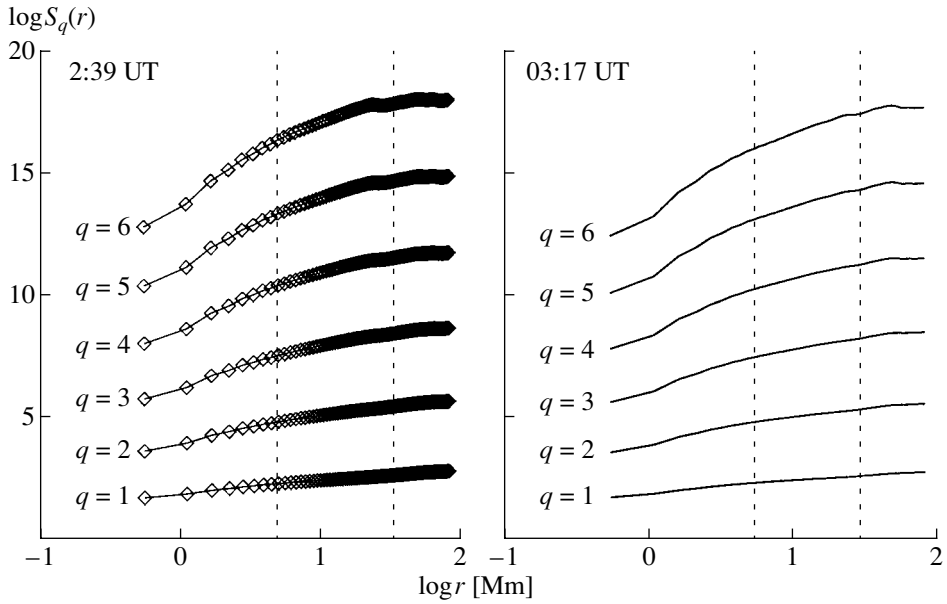

Fig. 3. Logarithms of the structure functions as functions of the scale, calculated using the last two B_z maps for August 2, 1991. The vertical dotted lines denote the boundaries of the inertial interval.

used was $0.62'' \times 0.43''$, and the size of the field mapped was 512×512 cells. The calibration and other characteristics of these magnetic-field observations are described in detail in [20].

A powerful flare of magnitude 2B/X1.5 began in NOAA 6757 on August 2, 1991, at 03:07 UT, reached its maximum at 03:15 UT, and ended at 04:07 UT. Three records of the total magnetic-field vector were obtained by the HSOS during the 2.5 h before the flare, and another record was obtained 10 min after the onset of the flare (2 min after its maximum). Data outlining the chronological sequence of the events are presented in the table.

The magnetograms of NOAA 6757 are presented in Fig. 1. The images are of good quality and stable. Figure 2 shows a photograph of the 2B/X1.5 flare obtained by the HSOS in the H_β line. The flare covered a large part of the active region.

Since the group was located near the disk center, correction of $B_{||}$ for the effects of projection did not appreciably change the field structure, only increased slightly the noise level. (The recalculation of $B_{||}$ to B_z was carried out taking into account B_x and B_y [20], and the noise level in the HSOS measurements of the transverse field was approximately three times the noise level for the longitudinal field [19]). To avoid introducing noise associated with the transverse field into the structure of B_z, we assumed that the measured longitudinal field $B_{||}$ corresponds to the vertical component B_z. The structure functions (Section 3), magnetic-energy dissipation field (Section 4), and power spectra of B_z (Section 5) were calculated using the maps of $B_{||}$.

3. VARIATIONS IN THE PARAMETERS DERIVED FROM THE STRUCTURE FUNCTIONS OF B_z

We calculated the structure functions $S_q(r)$ of B_z for each magnetogram in the table as follows [15]:

$$S_q(r) = \langle |B_z(\mathbf{x}+\mathbf{r}) - B_z(\mathbf{x})|^q \rangle. \qquad (1)$$

Here, q is any real number and $\mathbf{r}$ is the vector separating two arbitrary points $\mathbf{x} \equiv (x, y)$ in the two-dimensional magnetogram. The angular brackets denote averaging over the magnetogram. The following power law is valid for the structure functions in the case of large Reynolds numbers in the inertial interval [21, 22]:

$$S_q(r) \sim (r)^{\zeta(q)}. \qquad (2)$$

We calculated the structure functions for several values of q from 0.5 to 6.0 in steps of 0.5. The $S_q(r)$ dependences for integer values of q for two magnetograms are presented in Fig. 3. Our choice of the linear inertial interval (5–30 Mm) was based on the following considerations. The magnetic structures of the active region at $r > 30$ Mm are related to regular, large-scale motions rather than turbulent motions. The lower boundary of the interval corresponds to three times the telescope resolution (about $2''$), which is determined by the influence of the Earth's atmosphere. It was shown in [16, 17] that the decrease in

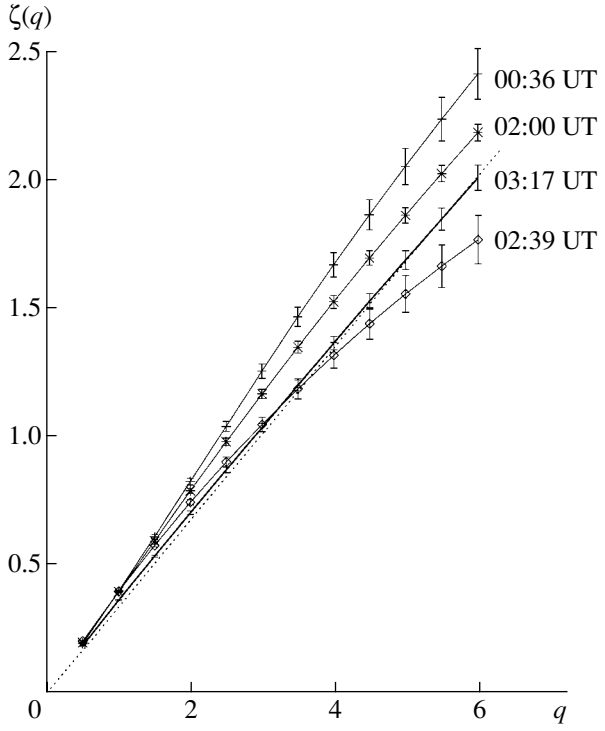

Fig. 4. The functions $\zeta(q)$ calculated as slopes (on logarithmic scales) of the structure functions $S_q(r)$ in the inertial interval using the magnetograms for August 2, 1991. The dotted line represents the classical (K41) Kolmogorov line with slope 1/3. The plot of $\zeta(q)$ after the flare maximum (at 03:17 UT) is shown by the thick curve.

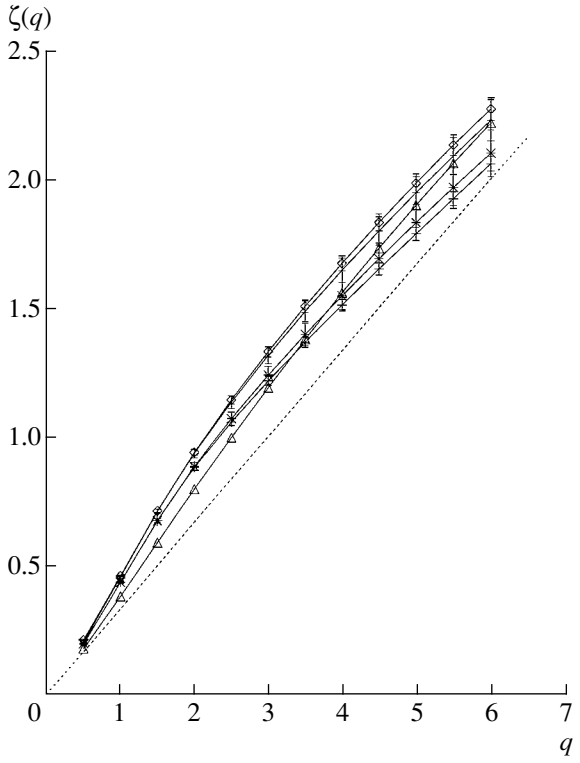

Fig. 5. Same as Fig. 4 for the five magnetograms of August 1, 1991, i.e., during an 8 h period without flares.

the spectra at the corresponding frequencies is associated with the influence of a characteristic function corresponding to the telescope resolution.

The exponents of the structure functions $\zeta(q)$ calculated as slopes of the $\log S_q(r)$—$\log r$ plots [15] for the four magnetograms of NOAA 6757 in the inertial interval are presented in Fig. 4. As in [15], the dotted line corresponds to a slope of 1/3 (i.e., the K41 line). This is the behavior of structure functions in the classical turbulence theory of Kolmogorov, when the parameters of the scale invariance of the medium depend only on the average energy dissipation and the turbulent medium itself does not display intermittency; i.e., it represents a monofractal with a Gaussian distribution (see, for example, [7, 15, 22]).

A decrease in $\zeta(q)$ at large q and an increase in the curvature of $\zeta(q)$ are clearly visible in Fig. 4 before the flare. The $\zeta(q)$ curve enters the region under the K41 line at $q > 3$ just before the flare. This tendency is traced especially well by ζ at $q = 6$, and the values of $\zeta(6)$ are presented in the second column of the table. Note that $\zeta(6) = 2.0$ in the classical Kolmogorov theory. For comparison, we present in Fig. 5 plots of the structure-function exponents $\zeta(q)$ calculated using five magnetograms of the same active region on the previous day (August 1, 1991) recorded during an 8 h interval without flares. All the plots in this figure are located quite close to each other and above the K41 line.

Such variations in $\zeta(q)$ agree well with the results of [15], in which we studied groups with different flare activity. Namely, the plots of $\zeta(q)$ for groups with low activity were located above the K41 line, and the higher the magnitude of the most powerful flare in a group, the lower its location in the $\zeta(q)$ plot with respect to the K41 line. This demonstrates that the shape of $\zeta(q)$ is associated with the flare activity of the group and the proximity of its state to a flare state.

In our opinion, the most interesting result is the straightening of $\zeta(q)$ 2 min after the flare maximum: at 03:17 UT, $\zeta(q)$ coincides perfectly with the Kolmogorov K41 line within the measurement errors, with the value of $\zeta(6)$ being very close to 2.0. This clear transition from multifractal to monofractal behavior points toward substantial qualitative changes in the structure of B_z associated with the onset of the flare.

The multifractal character (i.e., degree of intermittency) of the field can be probed using the derivative

of $\zeta(q)$:

$$h(q) = \frac{d\zeta(q)}{dq}. \quad (3)$$

The values of $h(q)$ usually fill some interval Δh [22]. Each value of $h(q)$ from this interval corresponds to a subset of dimensionality $D(h)$. The field under investigation represents a population of subsets with dimensionalities $D(h)$ and thereby forms a multifractal. The broader Δh, the more complex the multifractal structure of the field. In the case of classical Kolmogorov turbulence (K41), only the single value $h = 1/3$ is allowed, so that the corresponding structure represents a monofractal. On the other hand, the multifractal behavior is manifest as a tendency for the small-scale turbulence to be concentrated in separate, high-intensity bunches surrounded by extended regions with smooth large-scale perturbations.

Plots of $h(q)$ are presented in Fig. 6, and the values of Δh are given in the third column of the table. We can see that the interval Δh increases just before the flare. The function $h(q)$ is maximum 2.5 h before the flare (the magnetogram at 00:36 UT), as is characteristic of regions of low flare activity (see Fig. 4 in [15]). Further, the function $h(q)$ moves downward, below the K41 line, 28 min before the flare, and its shape becomes similar to that for regions of high flare activity.

The pattern changes abruptly just after the flare maximum: $h(q)$ becomes nearly linear and lies along the K41 line. The B_z field behaves like a monofractal with h close to 1/3. Thus, the entire multifractal pattern disappeared over less than 36 min; i.e., in the time interval in which the 2B/X1.5 flare began and reached its maximum. This suggests that the flare stimulated a transition to another turbulence regime.

The deviation of $\zeta(q)$ from the Kolmogorov K41 line is due to the character of the intermittency, i.e., to the fractal characteristics of the field $\varepsilon_r(\mathbf{x})$ of the energy-dissipation fluctuations for the structure considered [21, 22]. The monofractal structure of the energy-dissipation fluctuation field in the turbulent flow results in the linear dependence of $\zeta(q)$ on q. The deviation of $\zeta(q)$ below the K41 line at $q > 3$ implies an intermittent character for the energy-dissipation field. This follows from the historical critical comment by Landau concerning the classical Kolmogorov theory of turbulence (see, for example, [22]).

Using the function $\zeta(q)$ derived from (1) and (2) and its value at $q = 6$, we can determine the exponent β of the one-dimensional spectrum of the fluctuations in the dissipation of the magnetic energy [21]:

$$E^{(\varepsilon)}(k) \sim k^{-1+\mu} \equiv k^{\beta}, \quad (4)$$

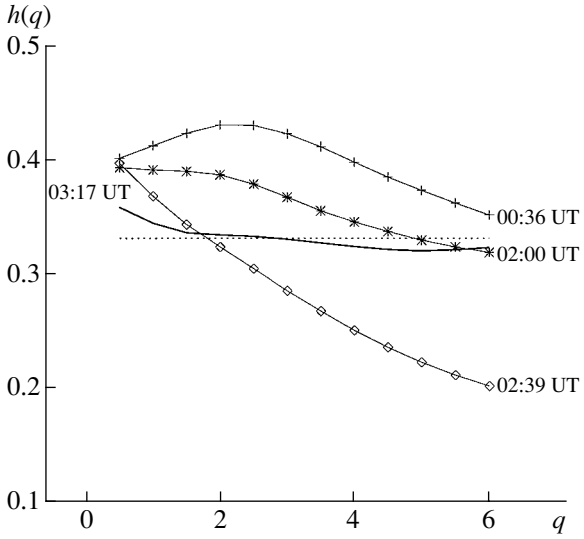

Fig. 6. Functions $h(q)$ calculated as the derivatives $d\zeta/dq$. The dotted line corresponds to the value $h = 1/3$ for the classical Kolmogorov K41 theory. The notation is the same as in Fig. 4.

where $\mu = 2 - \zeta(6)$; i.e., $\beta = 1 - \zeta(6)$. The values of β are presented in the fourth column of table. We can see that the absolute value of β decreases before the flare; i.e., the spectrum $E^{(\varepsilon)}(k)$ flattens. This corresponds to an increase in the relative contribution of the power of the energy-dissipation fluctuations on small scales; i.e., to an enhancement of the small-scale irregularities.

After the flare, the value of β almost coincides with -1. This corresponds to a situation in which all the statistical parameters of the field $\varepsilon_r(\mathbf{x})$ are specified by its average value $\bar{\varepsilon}$ and dispersion [21]. In other words, it is reasonable to suppose that the dissipation field, as well as the B_z field, are no longer multifractal after the flare.

4. VARIATIONS IN THE DISSIPATION FIELDS FOR B_z AND $\mathbf{B}_\perp$

The dissipation of the energy of the turbulent flow per unit mass per unit time is defined as [21]

$$\varepsilon(\mathbf{x}) = \frac{\nu}{2}\sum\left(\frac{du_i}{dx_j} + \frac{du_j}{dx_i}\right)^2, \quad (5)$$

where ν is the viscosity coefficient.

It follows from (5) that the calculation of the magnetic-energy dissipation field in the photosphere $\varepsilon(\mathbf{x})$ requires simultaneous measurements of the total field vector in some volume, which are not available. Therefore, we shall study only the dissipation fields for the longitudinal B_z and transverse $\mathbf{B}_\perp$ components of the magnetic field in the photosphere.

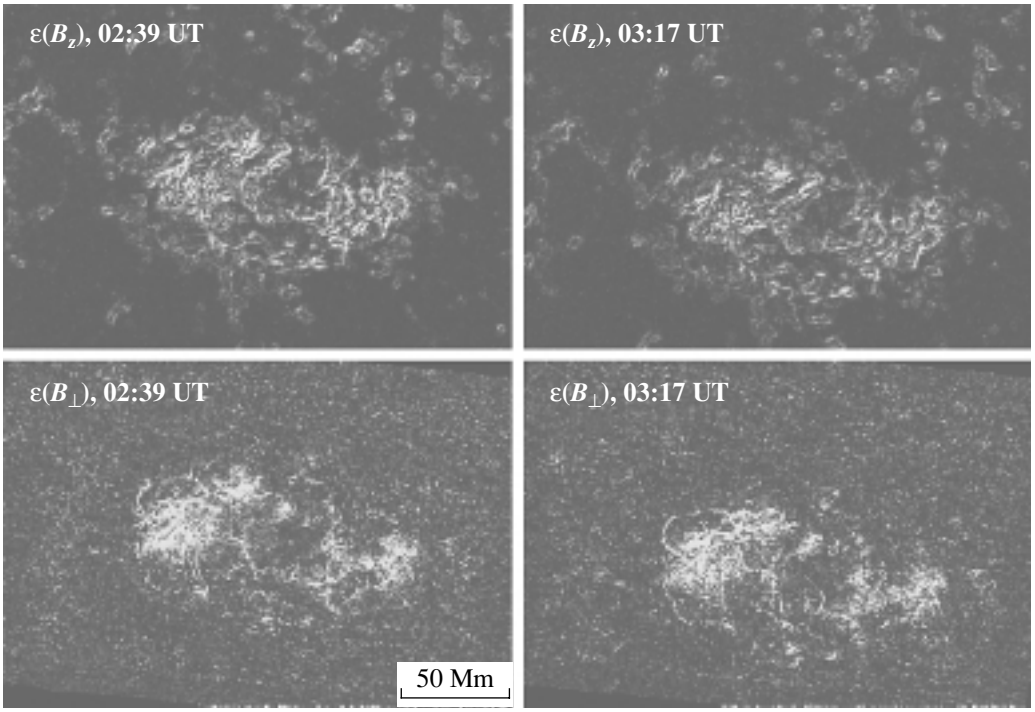

Fig. 7. Structures of the dissipation of the magnetic energy for the longitudinal and transverse components of the magnetic field calculated using the magnetograms for August 2, 1991.

Expression (5) can be transformed into the following form for the longitudinal and transverse magnetic-field components:

$$\varepsilon(B_z) = \nu\left(4\left(\left(\frac{dB_z}{dx}\right)^2 + \left(\frac{dB_z}{dy}\right)^2\right) + 2\left(\frac{dB_z}{dx} + \frac{dB_z}{dy}\right)^2\right), \quad (6)$$

$$\varepsilon(\mathbf{B}_\perp) = \nu\left(4\left(\left(\frac{dB_x}{dx}\right)^2 + \left(\frac{dB_y}{dy}\right)^2\right) + 2\left(\frac{dB_x}{dy} + \frac{dB_y}{dx}\right)^2\right), \quad (7)$$

(where x, y are the coordinates in the plane of the magnetogram).

Taking the viscosity coefficient ν to be uniform and equal to unity, we calculated the structures of $\varepsilon(B_z)$ and $\varepsilon(\mathbf{B}_\perp)$. These are presented in Fig. 7 for two recordings of the field (before and after the flare). Using these structures, we calculated the power spectra $E^{(\varepsilon)}(B_z)$ and $E^{(\varepsilon)}(\mathbf{B}_\perp)$ using the method described in [16, 17]. The spectra (in arbitrary units) are shown in Figs. 8 and 9. Before the flare, these spectra are irregular, have many maxima, and do not show any easily distinguishable linear intervals. This is especially true of the $E^{(\varepsilon)}(\mathbf{B}_\perp)$ spectra in Fig. 9. It is known [21, 23] that the presence of maxima in a power spectrum indicates the nonuniformity and instability of the structure, a supplemental input of energy to the system within separate frequency intervals distributed throughout the entire frequency range, and the deviation of the turbulence regime from a classical Kolmogorov regime. After the flare, the $E^{(\varepsilon)}(\mathbf{B}_\perp)$ spectrum becomes almost linear in the interval 4–40 Mm (Fig. 9), and the $E^{(\varepsilon)}(B_z)$ spectrum becomes smoother in the interval 3–18 Mm (Fig. 8).

These calculations (which were independent of the structure-function calculations) demonstrate that a new statistical turbulence regime for the magnetic field (closer to a classical Kolmogorov regime) was established after the onset of the flare. The energy-dissipation fields for B_z and $\mathbf{B}_\perp$ became considerably simpler. This can also be traced by comparing the structures of $\varepsilon(B_z)$ before and after the flare in Fig. 7.

We used the $E^{(\varepsilon)}(B_z)$ spectra to estimate the spectral exponent—the parameter $\tau(q)$ in the expression $E^{(\varepsilon)}(B_z) \sim k^{\tau(q)}$—in the interval 3–18 Mm. The values of $\tau(q)$ are given in the fifth column of the table. We can see that $\tau(q)$ varies synchronously with the exponent β, providing independent confirmation of the tendency for β to vary during the flare, as was found earlier in Section 3.

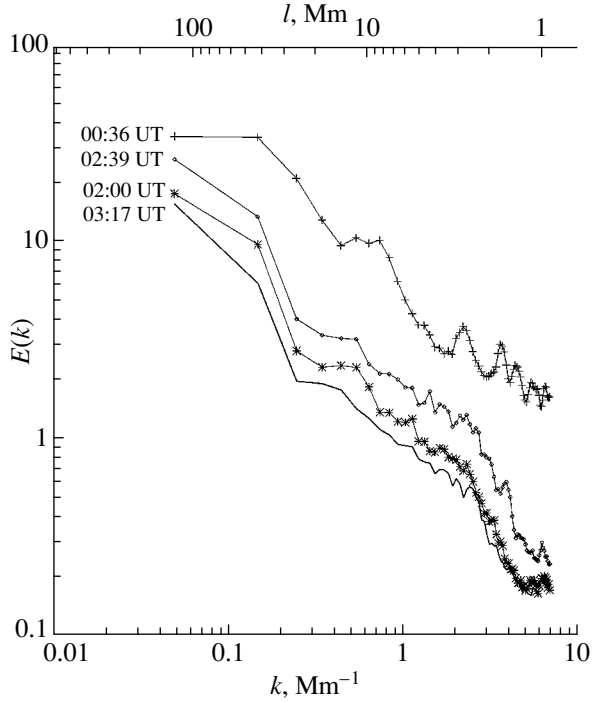

Fig. 8. Energy dissipation power spectra for B_z calculated using the magnetograms for August 2, 1991. The power is plotted along the vertical axis in arbitrary units. The notation for the magnetograms is the same as in Fig. 4. The spectrum after the flare maximum is shown by the thick curve.

5. VARIATIONS IN THE POWER SPECTRA OF B_z

Using the procedure presented in [16, 17], we calculated one-dimensional power spectra for the four magnetograms of the B_z magnetic-field component presented in Fig. 1. The results are shown in Fig. 10. We have not corrected these spectra for the noise level or the instrumental function [16, 17]. The errors are smaller than the size of the symbols. The spectrum of the earliest recording (00:36 UT) is considerably higher than the others in the high-frequency range ($k > 4$ Mm^{-1}), which suggests that it has a higher noise level. The spectra nearly coincide in the low-frequency range (i.e., on large scales, $r > 20$ Mm) before the flare, but the power on these scales decreases appreciably after the flare (i.e., 2 min after the flare maximum).

A fragment of Fig. 10 depicting the spectra in the interval 6.7–43 Mm, covering the linear inertial interval 7–25 Mm, is shown separately in Fig. 11. Strictly speaking, this is not the entire physical inertial interval but only the part that was observable with our resolution [16, 17]. The spectral exponents α calculated in the inertial interval are presented in the sixth column of the table.

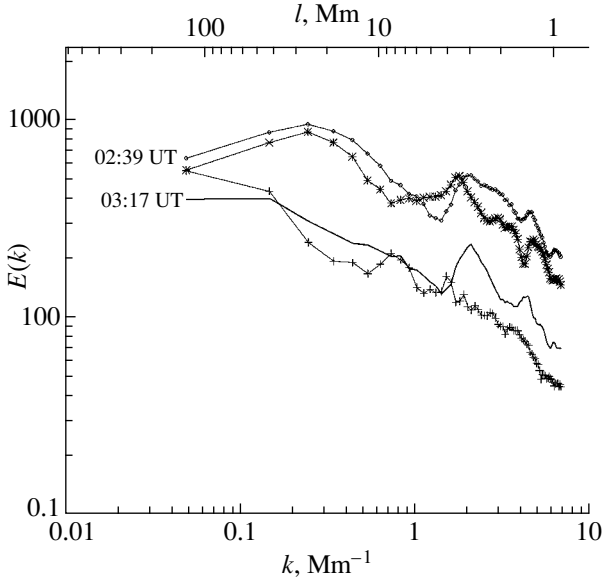

Fig. 9. Same as Fig. 8 for the energy of the $\mathbf{B}_\perp$ field.

Figure 11 shows that the power increases on all scales below 18 Mm as the onset of the flare approaches. (Note that the same tendency is seen on scales below 7 Mm, but the corresponding spectra are distorted by the unknown instrumental function.) The changes noted above can be explained by a pre-flare amplification of the fluctuations of B_z on scales

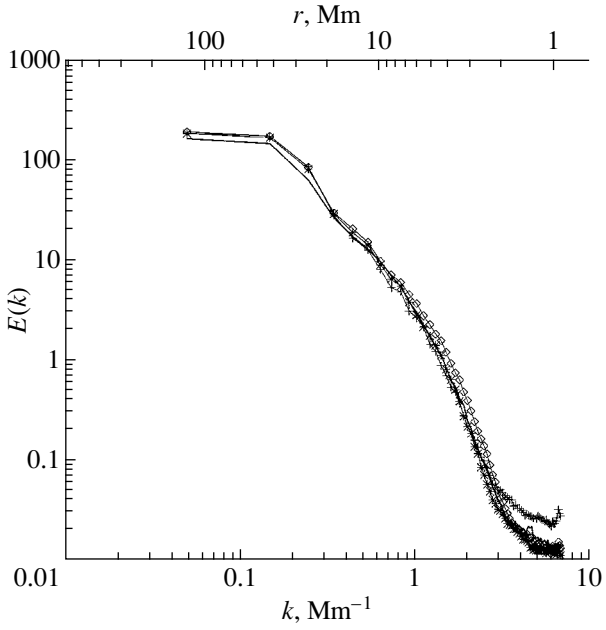

Fig. 10. Power spectra of B_z calculated using the magnetograms for August 2, 1991. The logarithm of the normalized power spectrum in units of 10^{10} J/m is plotted along the vertical axis. The notation for the magnetograms is the same as in Fig. 4.

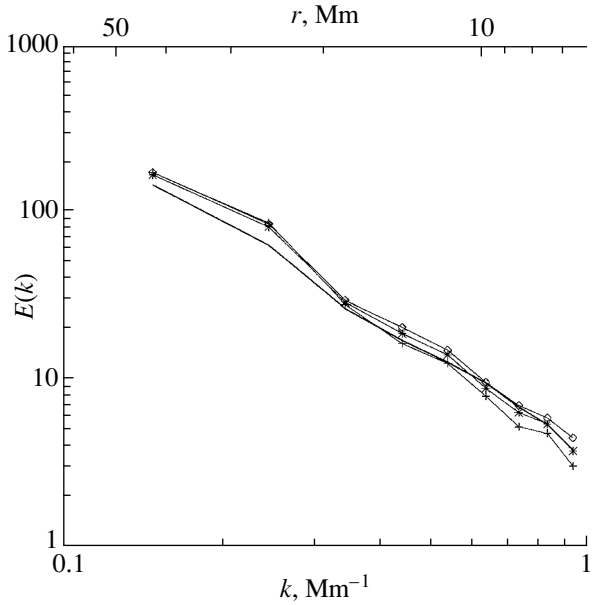

Fig. 11. Fragment of the spectra presented in Fig. 10 for the scale interval 6.7–43 Mm.

below 18 Mm, in agreement with the conclusion of Section 3 about the origin of the decreasing exponent β in the spectrum of the magnetic-energy dissipation fluctuations. The absolute values of α decrease (i.e. the preflare spectra becomes flatter) and do not correspond to the Kolmogorov value $-5/3$.

After the flare, the power was nearly constant in the high-frequency part of the inertial interval but decreased appreciably in the low-frequency region (Fig. 11). This can be explained by the development of a direct cascade in the turbulent flow (i.e., the transfer of energy from larger to smaller scales). In general, the spectrum became more linear, and its slope decreased; i.e., α became closer to the Kolmogorov value than it was before the flare.

The changes revealed in the power spectrum of B_z imply a gradual, monotonic variation in the turbulent state of the B_z field before the flare and an abrupt change in the character of the turbulence associated with the onset of the flare.

6. VARIATIONS IN FRACTAL PARAMETERS OF THE TOTAL MAGNETIC-FIELD VECTOR

In [11–14], we studied the behavior of the coefficient for the mutual compensation of opposite polarities, k_h (the cancellation index), for structures of the current helicity of the magnetic field.

The current helicity $h_c = \nabla \times \mathbf{B}_\perp \cdot B_z$ can be interpreted as the vorticity of the transverse field weighted by B_z: its structures follow the patterns of the electric currents in those parts of an active region where B_z is not small [12]. The quantity k_h is calculated as a scaling index of the signed measure of the current helicity [11, 18] and characterizes the degree of smoothness (the Hölder index) of the transverse magnetic field: the lower k_h, the smoother the field.

The coefficient k_h is fairly large during periods of low flare activity of a group and decreases substantially in periods of high activity [13, 14]. However, it had not been possible to establish the behavior of k_h within a few hours of the onset of a flare (due to incompleteness in measurements of the total field vector and the rare availability of magnetograms recorded just before powerful flares). From this point of view, the active region NOAA 6757 studied here represents a valuable example. We calculated the structures of the current helicity and the coefficients k_h using the four recordings of the total field vector listed in the table; the resulting coefficients k_h are presented in the seventh column of the table.

We can see that k_h remains at the same level (about 0.76) up until the recording 28 min before the flare and has decreased to 0.68 in the recording 2 min after the flare maximum. It is possible that this decrease actually occurred in the period from the onset to the maximum of the flare and that the number of tangential discontinuities of the field decreased sharply in this same period.

7. CONCLUSION

We have considered the following two problems. First, does the character of the turbulence of the photospheric magnetic field change within a few hours before a flare, and does it differ from the character of the turbulence just after the flare maximum? Second, if the answer to the first question is positive, what turbulent parameters are most well suited for short-term forecasting of flares?

The results presented here clearly indicate that the statistical regime of the magnetic-field turbulence in the photosphere of an active region changes smoothly before the flare and is completely different from the turbulent regime at the flare maximum.

The degree of intermittency of B_z increases within several hours before the flare. This behavior implies a broadening of the multifractal spectrum of the structure of B_z or, in other words, the formation of subsets of strong narrow peaks of the same polarity and abrupt changes in sign, whose distribution is not Gaussian.

The appearance of narrow peaks of the same polarity can be explained by the emergence and amplification of small-scale tubes of strong magnetic field just before the flare. The dimensions of these flux tubes are apparently considerably smaller than

the resolution of the field measurements. As a result, they do not contribute appreciably to the detected flux and cannot be identified visually in magnetograms. Nevertheless, they must inevitably substantially affect the higher moments of the statistical characteristics of the field, as we have found. The existence and role of these solar magnetic-flux tubes with field intensities of several kG and dimensions less than 100 km have been discussed in detail, for example, in review [24].

Abrupt changes in the sign of B_z correspond to tangential discontinuities of the field. The increase in the intermittency of B_z and the magnetic-energy dissipation field before the flare appear to be a photospheric manifestation of the increase in the number of tangential field discontinuities in a global "plasma + magnetic field" system encompassing the active region from subphotospheric layers to the corona. This system reaches a critical state when a breakdown of some sort occurs (in the form of a flare or an avalanche of nanoflares). A new turbulence regime forms after the breakdown of this avalanche. This new regime is characterized by a more uniform distribution of the energy-dissipation fluctuations; i.e., the turbulence becomes less intermittent and more similar to classical Kolmogorov turbulence with a Gaussian distribution.

After preparing this manuscript, we became aware that this behavior can be explained by the results of numerical modeling [25] of an avalanche of nanoflares in the SOC model (see review [26]). If we assume, following [25], that the process of magnetic-energy dissipation before the flare is due primarily to reconnection at tangential discontinuities [27, 28], the statistical characteristics of the field will exhibit evident deviations from Gaussian distributions, i.e., intermittency. As an avalanche (corresponding observationally to a flare) approaches, the number of tangential discontinuities and the deviation from a Gaussian distribution increase. After the breakdown of the avalanche (i.e., the flare maximum), the number of discontinuities sharply decreases, the statistical characteristics become Gaussian, and there is dissipation due to the anomalous plasma resistance [29].

Let us summarize the response of the parameters of the photospheric turbulence used here during the approach and onset of a flare, so that the most convenient of them for forecasting can be identified.

(1) The preflare changes in the shape of $\zeta(q)$—the exponent of the structure function of the longitudinal field B_z—are the most reliable, visually striking, and simple (computationally) manifestations. The shape of $\zeta(q)$ begins to vary within 1–2 h before a flare: its curvature increases, and the values of $\zeta(q)$ for high moments ($q > 3$) become lower than the classical Kolmogorov values within 28 min before the flare. The absolute value of the exponent of the magnetic-energy dissipation spectrum β, derived from $\zeta(6)$, decreases, and the rate at which it varies increases as the flare approaches. Two minutes after the flare maximum, $\zeta(q)$ becomes nearly linear and coincides with the classical Kolmogorov line within the observational errors.

Data on the longitudinal magnetic fields of active regions are now widely available, and the computation of structure functions takes only a few minutes on a PC. Therefore, the parameters derived directly from the structure-function plots (Δh and β) can easily be used for short-term forecasting of powerful flares.

(2) Quantities derived from the slope of the power spectra of both B_z (α, see table) and the dissipation field $\varepsilon(B_z)$ (τ) are less reliable and convenient for short-term forecasting. They suffer from considerable computational errors due to the nonlinear character of the spectra, especially just before the flare. On the other hand, the general shapes of the power spectra for B_z and $\varepsilon(B_z)$ (rather than their slopes) are rather informative. The spectra of the longitudinal field exhibit a preflare, continuous (along the spectrum) accumulation of power in fluctuations of B_z on scales below 18 Mm; the smaller the scale, the more intense the accumulation. (This is in good agreement with the results of [30] for the transverse magnetic-field component.) The spectra of the dissipations of the longitudinal and transverse fields indicate the presence of irregularities and supplementary energy input on various scales prior to the flare [21, 23]. This implies a transformation of the turbulence to a qualitatively new regime that is closer to a classical Kolmogorov regime after the flare maximum.

(3) The scaling parameter k_h of the signed measure of the current helicity, derived from the total magnetic-field vector, certainly reacts to the flare, but probably too quickly: it remains high and does not exhibit any stable, monotonic variations up to 28 min before the flare. Its value had decreased substantially by 2 min after the flare maximum. This result is in agreement with the single case of variations in k_h during a flare that was detected in our previous investigations of the current helicity [30]. Namely, there was a large value of k_h 12 min before the flare and a considerably lower value within 3 min after the flare onset in the active region NOAA 7315. Unfortunately, we were not able to trace variations in k_h before this flare. The decrease in k_h implies an increase in the smoothness of the photospheric transverse field (i.e., in the Hölder index), suppression of small-scale fluctuations, and a decrease in the intensity of tangential discontinuities of the transverse field [10, 30]. It cannot be ruled out that the sharp drop of k_h begins just at the flare onset. In that case, this can be considered

evidence for an avalanche dissipation of the small-scale tangential discontinuities in the transverse field, i.e., a nanoflare avalanche [8–10, 25, 26].

Therefore, our conclusions suggest that the conditions for a flare at the photospheric level are prepared within several hours before its onset: the multifractal structure of both the magnetic field and the energy-dissipation fluctuation field acquire a more complex character. Moreover, this preparation is not local and encompasses the entire active region on all scales. The onset of the flare is associated with a transition to a new turbulence regime: intermittent turbulence is replaced by a classical Kolmogorov regime without intermittency.

REFERENCES

1. E. N. Parker, *Cosmical Magnetic Fields: Their Origin and Their Activity* (Clarendon, Oxford, 1979; Mir, Moscow, 1982), Part 2.
2. E. R. Priest, *Solar Magnetohydrodynamics* (Reidel, Dordrecht, 1982; Mir, Moscow, 1985).
3. R. C. Canfield, E. R. Priest, and D. M. Rust, in *Flare-related Magnetic Field Dynamics,* Ed. by Y. Nakagawa and D. M. Rust (NCAR, Boulder, 1974).
4. J. Heyvaerts, E. R. Priest, and D. M. Rust, Astrophys. J. **216**, 123 (1977).
5. M. J. Hagyard, D. Teuber, E. A. West, and J. B. Smith, Sol. Phys. **91**, 115 (1984).
6. T. Sakurai, K. Shibata, K. Ichimoto, *et al.*, Publ. Astron. Soc. Jpn. **44** (5), L123 (1992).
7. Ya. B. Zel'dovich, S. A. Molchanov, A. A. Ruzmaĭkin, and D. D. Sokolov, Usp. Fiz. Nauk **152** (1), 3 (1987) [Sov. Phys. Usp. **30**, 353 (1987)].
8. E. N. Parker, Sol. Phys. **111** (2), 297 (1987).
9. E. N. Parker, Astrophys. J. **330** (1), 474 (1988).
10. E. N. Parker, Sol. Phys. **121** (1/2), 271 (1989).
11. V. I. Abramenko, V. B. Yurchishin, and V. Carbone, Kin. Fiz. Neb. Tel **14** (2), 99 (1998).
12. V. I. Abramenko, Astron. Zh. **76** (9), 712 (1999) [Astron. Rep. **43**, 622 (1999)].
13. V. I. Abramenko, V. B. Yurchishin, and V. Carbone, in *Magnetic Fields and Solar Processes,* ESA SP-448, Vol. 1, p. 679 (1999).
14. V. B. Yurchyshyn, V. I. Abramenko, and V. Carbone, Astrophys. J. **538**, 968 (2000).
15. V. I. Abramenko, Astron. Zh. **79** (2), 182 (2002) (Astron. Rep. **46**, 161 (2002)].
16. V. I. Abramenko, V. B. Yurchishin, H. Wang, and P. R. Goode, Astron. Zh. **78** (10), 942 (2001) [Astron. Rep. **45**, 824 (2001)].
17. V. I. Abramenko, V. B. Yurchishin, H. Wang, and P. R. Goode, Sol. Phys. **201**, 225 (2001).
18. V. I. Abramenko, V. B. Yurchishin, and V. Carbone, Sol. Phys. **178**, 35 (1998).
19. J. Wang, Z. Shi, H. Wang, and Y. Lu, Astrophys. J. **456**, 861 (1996).
20. V. I. Abramenko, T. J. Wang, and V. B. Yurchishin, Sol. Phys. **168**, 75 (1996).
21. A. S. Monin and A. M. Yaglom, *Statistical Fluid Mechanics* (Nauka, Moscow, 1967; MIT Press, Cambridge, 1975), Vol. 2.
22. U. Frisch, *Turbulence. The Legacy of A.N. Kolmogorov* (Cambridge Univ. Press, Cambridge, 1995).
23. J. A. Eilek, Astron. J. **98** (1), 256 (1989).
24. J. O. Stenflo, Astron. Astrophys. Rev. **1**, 3 (1989).
25. O. V. Podladchikova, V. Krasnoselskikh, and B. Lefevre, in *Magnetic Fields and Solar Processes,* ESA SP-448, Vol. 1, p. 553 (1999).
26. P. Charbonneau, S. W. McIntosh, H. L. Liu, and T. J. Bogdan, Sol. Phys. **203** (2), 322 (2001).
27. S. I. Syrovatskiĭ, Izv. Akad. Nauk SSSR **43** (4), 695 (1979).
28. S. I. Syrovatsky, Sol. Phys. **76** (1), 3 (1982).
29. B. B. Kadomtsev, *Collective Phenomena in Plasmas* [in Russian] (Nauka, Moscow, 1976).
30. V. I. Abramenko, V. B. Yurchishin, and V. Carbone, Kin. Fiz. Neb. Tel **14** (3), 210 (1998).

Translated by Yu. Dumin

Astronomy Reports, Vol. 47, No. 2, 2003, pp. 161–167. Translated from Astronomicheskiĭ Zhurnal, Vol. 80, No. 2, 2003, pp. 186–192.

Nonlinear Stochastic Correlation Models for the Pole's Motion of a Deformable Earth

Yu. G. Markov[1] and I. N. Sinitsyn[2]

[1] *Moscow State Aviation Institute, Moscow, Russia*
[2] *Institute for Problems of Informatics, Moscow, Russia*

Received April 15, 2002; in final form, June 26, 2002

Abstract—A combined stochastic correlation model for the pole's motion of a deformable Earth is constructed using the data of the International Earth Rotation Service and dynamical Euler equations taking into account tidal deformations. The deterministic component of the model describes the main regular dynamical effects, while its stochastic component describes irregular effects obeying statistical laws. Linear differential (requiring solutions of ordinary differential equations), and finite (assuming integrated characteristics) correlation models are constructed for both Gaussian and non-Gaussian random parameters. The stochastic oscillations and trend of the Earth's proper angular velocity are analyzed, as well as nonlinear stochastic oscillations and the trend of the pole. This approach can be considered quite novel. © *2003 MAIK "Nauka/Interperiodica"*.

1. INTRODUCTION

At the present time, mathematical models of the Earth's polar motions that adequately describe observations and measurements carried out by the International Earth Rotation Service (IERS) are of both scientific and practical importance [1–4]. According to IERS data, the complex polar motions contain, first, the Chandler wobble (free nutation), with an amplitude of $0.20''$–$0.25''$ and a period of 433 ± 2 sidereal days [3]. The characteristic features of the Chandler component are related to the inertia tensor of the deformable Earth [4]. The second component of the polar motions is the annual oscillation, with an amplitude of $\sim 0.07''$–$0.08''$ and a period of one year (365 sidereal days). The reasons for the excitation of the annual oscillation remain unknown. It is usually associated with seasonal geophysical phenomena (atmospheric processes and oceanic tides) [1, 2]. According to [4, 5], the annual oscillations of the Earth's axis can be attributed to the solar gravitational moment, the orbital motion of the spinning Earth, and diurnal tides in the mantle.

The trend of the Earth's pole ($\sim 0.5''$, 90° westward from Greenwich), which, in our opinion, is associated with the centrifugal moments of inertia of the deformable Earth, is of fundamental importance for any mathematical models of the Earth's polar motions on long time intervals (~ 50 years or more). The construction of linear stochastic models for the polar motions of the deformable Earth taking into account the tidal humps and bulges was presented in [6]. In the present work, we construct nonlinear stochastic correlation models.

This article contains six sections. The first derives the equations of motion based on celestial mechanics and the IERS data [3]. In the second section, we compose linear differential and finite correlation models for the non-Gaussian random parameters. Sections 4 and 5 present the equivalent Gaussian nonlinear correlation models. The stochastic oscillations and trend of the proper angular velocity, as well as nonlinear stochastic oscillations of the pole, are analyzed. Finally, Section 6 contains the results of our analytical modeling and discussions of these results.

2. EQUATIONS OF MOTION

We proceed from the following three-dimensional nonlinear differential system with nine random parameters [6]:

$$\dot{p} + N_* q = 3V_1 b\omega_*^2 \cos\omega_* t - V_4 r^2 + P(t, p, q, r, \mathbf{V}), \quad p(t_0) = p_0, \tag{1}$$

$$\dot{q} - N_* p = -3V_2 b\omega_*^2 \cos\omega_* t + V_5 r^2 + Q(t, p, q, r, \mathbf{V}), \quad q(t_0) = q_0, \tag{2}$$

$$\dot{r} = -3V_3\omega_*^2(b' + b''\cos 2\omega_* t) + R(t, p, q, r, \mathbf{V}), \quad r(t_0) = r_0, \tag{3}$$

where

$$P = P(t, p, q, r, \mathbf{V}) = -3V_2V_6d_1b\omega_*^2\cos\omega_* t - 3V_3V_5d_1\omega_*^2(b' + b''\cos 2\omega_* t), \tag{4}$$

1063-7729/03/4702-0161$24.00

$$Q = Q(t,p,q,r,\mathbf{V}) = -3V_1V_6d_2b\omega_*^2\cos\omega_*t - 3V_3V_4d_2\omega_*^2(b' + b''\cos 2\omega_*t),$$
$$R = R(t,p,q,r,\mathbf{V}) = -3V_1V_2d_3b\omega_*^2\cos\omega_*t + 3V_1V_5d_3b\omega_*^2\cos\omega_*t$$

are the small specific moments of the perturbing forces. Here, p, q, and r are the projections of the Earth's angular velocity onto the fixed axes [2, 5], and the quantities

$$V_1 = \frac{1}{T_*}\int\limits_t^{t+T_*}\frac{\tilde C(\tau)-\tilde B(\tau)}{A^*}\cos r_*\tau d\tau, \qquad (5)$$
$$V_2 = \frac{1}{T_*}\int\limits_t^{t+T_*}\frac{\tilde C(\tau)-\tilde A(\tau)}{B^*}\sin r_*\tau d\tau,$$
$$V_3 = \frac{1}{T_*}\int\limits_t^{t+T_*}\frac{\tilde B(\tau)-\tilde A(\tau)}{C^*}\sin 2r_*\tau d\tau$$

are random parameters obtained by averaging the axial moments of inertia of the deformable Earth over the diurnal interval $T_* = 2\pi r_*^{-1}$ of the running time and characterize the effective diurnal humps of the solar tides, while

$$V_4 = \frac{J^*_{qr}}{A^*} + \frac{1}{T_*}\int\limits_t^{t+T_*}\frac{\tilde J_{qr}(\tau)}{A^*}d\tau, \qquad (6)$$
$$V_5 = \frac{J^*_{pr}}{B^*} + \frac{1}{T_*}\int\limits_t^{t+T_*}\frac{\tilde J_{pr}(\tau)}{B^*}d\tau,$$
$$V_6 = \frac{J^*_{pq}}{C^*} + \frac{1}{T_*}\int\limits_t^{t+T_*}\frac{\tilde J_{pq}(\tau)}{C^*}d\tau$$

are random parameters related to the centrifugal moments of inertia of the deformable Earth and determine the effective tidal bulges. $A^* + \tilde A(t)$, $B^* + \tilde B(t)$, $C^* + \tilde C(t)$ and $J^*_{pq} + \tilde J_{pq}(t)$, $J^*_{qr} + \tilde J_{qr}(t)$, $J^*_{rp} + \tilde J_{rp}(t)$ are the Earth's axial and centrifugal moments of inertia, with the component marked by the asterisk being constant while the one marked by the tilde varies due to the solar diurnal tides. V_7, V_8, and V_9 denote the random initial conditions

$$V_7 = p_0, \qquad V_8 = q_0, \qquad V_9 = r_0. \qquad (7)$$

In addition, we introduce the following notation:

$$N_* = (C^* - B^*)A^{*-1}\omega_*, \quad r_* = 365\omega_*, \qquad (8)$$
$$2b' = (1 - b^2/2), \qquad 2b'' = -b^2,$$
$$d_1 = \frac{B^*C^*}{A^*}, \quad d_2 = \frac{A^*C^*}{B^*}, \quad d_3 = \frac{A^*B^*}{C^*},$$
$$A^* = 8.0912\times 10^{37}\ \mathrm{kgm}^2,$$
$$B^* = 8.0914\times 10^{37}\ \mathrm{kgm}^2,$$
$$C^* = 8.11\times 10^{37}\ \mathrm{kgm}^2,$$

where ω_* is a constant determined by the gravitational and focal parameters and b ($0.4 < b < 4/3\pi^{-1}$) is a dimensionless coefficient [5].

When deriving Eqs. (1)–(3), we used the dynamical Euler equations taking into account the variations of the inertia tensor. We assumed that the lunar gravitational moments can be neglected due to their weak effect on the oscillations (the lunar effect gives rise to monthly amplitudes that are smaller than the annual amplitudes by a factor of 15–20). We have also taken into account the fact that the terms containing r, r^2, ω_*, and ω_*^2 significantly exceed the corresponding terms with squares of these quantities and products of p, q, $\dot{\tilde C}/C^*$, $\dot{\tilde J}_{pr}/A^*$, $\dot{\tilde J}_{rq}/B^*$, etc.

3. LINEAR DIFFERENTIAL AND FINITE CORRELATION MODELS

Let us examine first the case when we can neglect the nonlinear functions (4) and substitute r_0 (the axial speed of the Earth's rotation, $r_0 = 7.27\times 10^{-5}\ \mathrm{s}^{-1}$) for r in functions V_4r^2 and V_5r^2 of (1) and (2). This results in the following linear stochastic differential system:

$$\dot p_t + N_*q_t = 3V_1b\omega_*^2\cos\omega_*t - V_4r_0^2, \qquad (9)$$
$$p(t_0) = p_0 = V_7,$$
$$\dot q_t - N_*p_t = -3V_2b\omega_*^2\cos\omega_*t + V_5r_0^2,$$
$$q(t_0) = q_0 = V_8,$$
$$\dot r_t = -3V_3\omega_*^2(b' + b''\cos 2\omega_*t),$$
$$r(t_0) = r_0 = V_9$$

split on $p_t = p(t)$, $q_t = q(t)$, and $r_t = r(t)$.

Let us start with Eqs. (9) with the parameters V_i being real, random (not necessarily Gaussian) quantities with the mathematical expectations m_i^V, variances D_i^V, and covariances K_{ij}^V. We introduce the following notation for the mathematical expectations, variances, covariance functions, and covariances:

$$m_t^p = Mp_t, \quad m_t^q = Mq_t, \quad m_t^r = Mr_t, \qquad (10)$$
$$D_t^p = Mp_t^{02}, \quad D_t^q = Mq_t^{02}, \quad D_t^r = Mr_t^{02}, \qquad (11)$$
$$K^p_{t,t'} = Mp_t^0p_{t'}^0, \quad K^q_{t,t'} = Mq_t^0q_{t'}^0, \quad K^r_{t,t'} = Mr_t^0r_{t'}^0, \qquad (12)$$

$$K^{rp}_{t,t'} = Mr^0_t p^0_{t'}, \quad K^{qr}_{t,t'} = Mq^0_t r^0_{t'}, \quad K^{pq}_{t,t'} = Mp^0_t q^0_{t'}, \tag{13}$$

where M denotes the mathematical expectation (statistical averaging) and zero superscripts denote the centered random components p_t, q_t, and r_t.

Employing the linear theory of stochastic systems [7, 8] for $t = t'$, we obtain ordinary differential equations for the mathematical expectations, variances, and covariances of p_t and q_t:

$$\begin{aligned} \dot m^p_t &= -N_* m^q_t + m^V_1 F_{1t} - m^V_4 F_{2t}, \\ \dot m^q_t &= N_* m^p_t - m^V_2 F_{1t} + m^V_5 F_{2t}, \end{aligned} \tag{14}$$

$$\begin{aligned} \dot D^p_t &= 2N_* K^{pq}_t + 2F_{1t} K^{pV_1} - 2F_{2t} K^{pV_4}, \\ \dot D^q_t &= 2N_* K^{pq}_t - 2F_{1t} K^{qV_2} + 2F_{2t} K^{qV_5}, \\ \dot K^{pq}_t &= -N_* D^q_t + F_{1t} K^{qV_1} - F_{2t} K^{qV_4}, \end{aligned} \tag{15}$$

$$\begin{aligned} \dot K^{pV_1} &= -N_* K^{qV_1} + F_{1t} D^V_1 - F_{2t} K^{VV}_{14}, \\ \dot K^{pV_4} &= -N_* K^{qV_4} + F_{1t} K^{VV}_{14} - F_{2t} D^V_4, \\ \dot K^{pV_5} &= -N_* K^{qV_5} + F_{1t} K^{VV}_{15} - F_{2t} K^{VV}_{45}, \\ \dot K^{qV_1} &= N_* K^{pV_1} - F_{1t} K^{VV}_{12} + F_{2t} K^{VV}_{15}, \\ \dot K^{qV_2} &= N_* K^{qV_2} - F_{1t} D^V_2 + F_{2t} K^{VV}_{25}, \\ \dot K^{qV_5} &= N_* K^{pV_5} - F_{1t} K^{VV}_{25} + F_{2t} D^V_5, \end{aligned} \tag{16}$$

and

$$\begin{aligned} \dot m^r_t &= -m^V_3 F_{3t}, \quad \dot D^r_t = -F_{3t} K^{rV_3}, \\ \dot K^{rV_3} &= -D^V_3 F_{3t} \end{aligned} \tag{17}$$

for r_t, where

$$\begin{aligned} F_{1t} &= 3b\omega_*^2 \cos\omega_* t, \quad F_{2t} = r_0^2, \\ F_{3t} &= 3\omega_*^2 (b' + b'' \cos 2\omega_* t). \end{aligned} \tag{18}$$

We use the mathematical expectations $m^{p,q,r}_{t_0}$ as the initial conditions for p^0_t, q^0_t, and r^0_t. The ordinary differential equations for the covariance functions and covariances at $t' > t$ are obtained similarly. The ordinary differential equations (14)–(17) and corresponding initial conditions supply us with the desired linear differential correlation model for p_t, q_t, and r_t.

In accordance with [7, 8], we can derive finite linear correlation models, first, by integrating (14)–(17) and, second, by integrating Eqs. (9), in order to obtain the functions

$$p_t = p(t, \mathbf{V}), \quad q_t = q(t, \mathbf{V}), \quad r_t = r(t, \mathbf{V}) \tag{19}$$

followed by the application of the known formulas for the correlation characteristics of the angular velocities p_t, q_t, and r_t.

In the second case, we obtain for t and t' $(t' > t)$ the following finite expressions for the mathematical expectations, variances, covariances, and covariance functions of p_t, q_t, and r_t:

$$m^{p,q,r}_t = \sum_{i=1}^{9}{}^{(6)} \psi^{p,q,r}_{i,t} m^V_i, \tag{20}$$

$$D^{p,q,r}_t = \sum_{i=1}^{9}\sum_{j=1}^{9}{}^{(6)} \psi^{p,q,r}_{i,t} \psi^{p,q,r}_{j,t} K^V_{ij}, \tag{21}$$

$$K^{p,q,r}_{t,t'} = \sum_{i=1}^{9}\sum_{j=1}^{9}{}^{(6)} \psi^{p,q,r}_{i,t} \psi^{p,q,r}_{j,t'} K^V_{ij}, \tag{22}$$

$$K^{pq}_{t,t'} = \sum_{i=1}^{9}\sum_{j=1}^{9}{}^{(6)} \psi^{p}_{i,t} \psi^{q}_{j,t'} K^V_{ij},$$

$$K^{qr}_{t,t'} = \sum_{i=1}^{9}\sum_{j=1}^{9}{}^{(6)} \psi^{q}_{i,t} \psi^{r}_{j,t'} K^V_{ij},$$

$$K^{rp}_{t,t'} = \sum_{i=1}^{9}\sum_{j=1}^{9}{}^{(6)} \psi^{r}_{i,t} \psi^{p}_{j,t'} K^V_{ij}.$$

Here, the symbol "6" in the summations in (20)–(22) signifies that the summation over $i = \overline{1,9}$ eliminates the parameter V_6. The functions $\psi^{p,q,r}_{i,t}$ $(i = \overline{1,9})$ are the influence functions of the parameters V_i, which we obtain by solving (1)–(3) for $P = Q = R = 0$ and substituting $\psi^{p,q,r}_{i,t}$ for p, q, and r

$$\begin{aligned} \psi^p_{1,t} &= -\psi^q_{2,t} = b_0 \omega_* \sin\omega_* t, \\ \psi^p_{2,t} &= \psi^q_{1,t} = -b_0 N_* \cos\omega_* t, \\ \psi^r_{3,t} &= -3b'\omega_*^2 (t - t_0) - \frac{3}{2} b'' \omega_* \\ &\quad \times (\sin 2\omega_* t - \sin 2\omega_* t_0), \\ \psi^q_{4,t} &= \psi^p_{5,t} = -r_0^2 N_*^{-1}, \\ \psi^p_{7,t} &= \psi^q_{8,t} = \cos N_* (t - t_0), \\ \psi^p_{8,t} &= -\sin N_* (t - t_0) = -\psi^q_{7,t}, \quad \psi^r_{9,t} = 1, \\ \psi^p_{9,t} &= \psi^q_{9,t} = \psi^r_{7,t} = \psi^r_{8,t} = 0, \\ b_0 &= 3b\omega_*^2 (\omega_*^2 - N_*^2)^{-1}. \end{aligned} \tag{23}$$

The resulting equations show that the averaged (over the time $2\pi\omega_*^{-1}$) statistical trends in the vari-

ables p_t and q_t and the average variances and covariances for $t' = t$ are constant and equal to

$$\langle m_t^p \rangle = -r_0^2 m_5^V N_*^{-1}, \langle m_t^q \rangle = -r_0^2 m_4^V N_*^{-1}, \quad (24)$$
$$\langle D_t^p \rangle = \frac{1}{2} b_0^2 (\omega_*^2 D_1^V + N_*^2 D_2^V) + (r_0^2 N_*^{-1})^2 D_5^V,$$
$$\langle D_t^q \rangle = \frac{1}{2} b_0^2 (N_*^2 D_1^V + \omega_*^2 D_2^V) + (r_0^2 N_*^{-1})^2 D_4^V,$$
$$\langle K_{t,t}^{pq} \rangle = 0,$$

where $\langle \ldots \rangle$ denotes averaging over $2\pi\omega_*^{-1}$, with the covariance functions $K_{t,t'}^{p,q}$ being proportional to $\cos 2\omega_*(t' - t)$.

The nonstationary trend and variance in the variable r_t are

$$\langle m_t^r \rangle = r_0 - 3b'(t - t_0)\omega_*^2 m_3^V, \quad (25)$$
$$\langle D_t^r \rangle = \left\{ \left[3b\omega_*^2 (t - t_0) \right]^2 + \frac{1}{2} \left(\frac{3}{2} b'' \omega_* \right)^2 \right\} D_3^V,$$
$$\langle K_{t,t}^{qr} \rangle = \langle K_{t,t}^{rp} \rangle = 0.$$

By virtue of the linearity of Eqs. (9) in the variables p_t, q_t, and r_t and the parameters $V_1, \ldots, V_5$, the results remain valid for both real Gaussian and non-Gaussian random parameters.

4. NONLINEAR DIFFERENTIAL AND FINITE STOCHASTIC CORRELATION MODELS

Applying the theory of nonlinear, stochastic, differential systems based on the stochastic expansions [7, 8], we arrive at the following finite mathematical expectations, variances, covariances, and covariance functions of p_t, q_t, and r_t for times $t, t' > t$:

$$m_t^{p,q,r} = \sum_{i=1}^{9} \psi_{i,t}^{p,q,r} m_i^V + \Delta m_t^{p,q,r}, \quad (26)$$
$$D_t^{p,q,r} = \sum_{i=1}^{9} \sum_{j=1}^{9} \psi_{i,t}^{p,q,r} \psi_{j,t}^{p,q,r} K_{ij}^V + \Delta D_t^{p,q,r},$$
$$K_{t,t'}^{p,q,r} = \sum_{i=1}^{9} \sum_{j=1}^{9} \psi_{i,t}^{p,q,r} \psi_{j,t'}^{p,q,r} K_{ij}^V + \Delta K_{t,t'}^{p,q,r}, \quad (27)$$
$$K_{t,t'}^{pq} = \sum_{i=1}^{9} \sum_{j=1}^{9} \psi_{i,t}^{p} \psi_{j,t'}^{q} K_{ij}^V + \Delta K_{t,t'}^{pq}, \quad (28)$$
$$K_{t,t'}^{qr} = \sum_{i=1}^{9} \sum_{j=1}^{9} \psi_{i,t}^{q} \psi_{j,t'}^{r} K_{ij}^V + \Delta K_{t,t'}^{qr},$$
$$K_{t,t'}^{rp} = \sum_{i=1}^{9} \sum_{j=1}^{9} \psi_{i,t}^{r} \psi_{j,t'}^{p} K_{ij}^V + \Delta K_{t,t'}^{rp}.$$

Here, the functions $\Delta m_t^{p,q,r}$, $\Delta D_t^{p,q,r}$, $\Delta K_{t,t}^{p,q,r}$, $\Delta K_{t,t'}^{pq}$, $\Delta K_{t,t'}^{qr}$, and $\Delta K_{t,t'}^{pr}$ are the components of the mathematical expectations, variances, and covariances taking into account the nonlinear functions P, Q, and R. For arbitrary distributions of random parameters $\mathbf{V}$, we can find the mathematical expectations and covariance characteristics using the known formulae [7, 8] upon solving Eqs. (1)–(3) analogously to (19).

For the random Gaussian (normally distributed) parameters $\mathbf{V}$, we can obtain approximate ordinary differential equations for the equivalent Gaussian mathematical expectations, variances, and covariances using the method of normal approximations [7, 8].

5. EQUIVALENT GAUSSIAN NONLINEAR CORRELATION MODELS

In the correlation theory for nonlinear stochastic systems [7, 8], (1)–(4) are equivalent to the Gaussian stochastic differential equations, with the nonlinear functions $V_{4,\,5} r^2$, P, Q, and R replaced by the linearly normalized functions

$$V_i V_j \approx m_i^V m_j^V + K_{ij}^V + m_i^V V_j^0 + m_j^V V_i^0 \quad (29)$$
$$(i, j = \overline{1, 5}),$$
$$V_i r^2 \approx m_i^V (m_t^r)^2 + m_i^V D_t^r + 2 m_t^r K_{it}^{Vr}$$
$$+ \left[(m_t^r)^2 + D_t^r \right] V_i^0 + 2 \left(m_i^V m_t^r + K_{it}^{Vr} \right) r_t^0$$
$$(i = 4, 5).$$

In addition to (18), we introduce the following notation:

$$F_{4t} = F_{4t}(m, K) = -\left\{ m_4^V \left[(m_t^r)^2 - r_0^2 \right] + m_4^V D_t^r \right.$$
$$+ 2 m_t^r K_{4t}^{Vr} + 3 (m_2^V m_6^V + K_{26}^V) d_1 b \omega_*^2 \cos \omega_* t$$
$$\left. + 3 (m_3^V m_5^V + K_{35}^V) d_1 \omega_*^2 (b' + b'' \cos 2\omega_* t) \right\},$$
$$F_{5t} = F_{5t}(m, K) = m_5^V \left[(m_t^r)^2 - r_0^2 \right] + m_5^V D_t^r$$
$$+ 2 m_t^r K_{5t}^{Vr} - 3 (m_1^V m_6^V + K_{16}^V) d_2 b \omega_*^2 \cos \omega_* t$$
$$- 3 (m_3^V m_4^V + K_{34}^V) d_2 \omega_*^2 (b' + b'' \cos 2\omega_* t),$$
$$F_{6t} = F_{6t}(m, K) = -3 (m_1^V m_2^V + K_{12}^V) d_3 b \omega_*^2 \cos \omega_* t$$
$$+ 3 (m_1^V m_5^V + K_{15}^V) d_3 b \omega_*^2 \cos \omega_* t,$$
$$F_{7t} = F_{7t}(m, K) = 2 (m_4^V m_t^r + K_{4t}^{Vr}),$$
$$F_{8t} = F_{8t}(m, K) = (m_t^r)^2 + D_t^r,$$

$$F_{9t} = F_{9t}(m, K) = 3 m_6^V d_1 b \omega_*^2 \cos \omega_* t, \quad (30)$$

$$F_{10t} = F_{10t}(m,K) = 3m_2^V d_1 b\omega_*^2 \cos 2\omega_* t,$$
$$F_{11t} = F_{11t}(m,K) = 3m_5^V d_1\omega_*^2(b' + b''\cos 2\omega_* t),$$
$$F_{12t} = F_{12t}(m,K) = 3m_3^V d_1\omega_*^2(b' + b''\cos 2\omega_* t),$$
$$F_{13t} = F_{13t}(m,K) = 2(m_5^V m_t^r + K_{5t}^{Vr}),$$
$$F_{14t} = F_{14t}(m,K) = 3m_6^V d_2 b\omega_*^2 \cos\omega_* t,$$
$$F_{15t} = F_{15t}(m,K) = 3m_1^V d_2 b\omega_*^2 \cos 2\omega_* t,$$
$$F_{16t} = F_{16t}(m,K) = 3m_4^V d_2\omega_*^2(b' + b''\cos 2\omega_* t),$$
$$F_{17t} = F_{17t}(m,K) = 3m_3^V d_2\omega_*^2(b' + b''\cos 2\omega_* t),$$
$$F_{18t} = F_{18t}(m,K) = 3(m_2^V - m_5^V)d_3 b\omega_*^2 \cos\omega_* t,$$
$$F_{19t} = F_{19t}(m,K) = 3m_1^V d_3 b\omega_*^2 \cos 2\omega_* t,$$
$$F_{20t} = F_{20t}(m,K) = 3m_1^V d_3 b\omega_*^2 \cos 2\omega_* t.$$

We finally obtain the desired equivalent Gaussian system

$$\dot m_t^p = -N_* m_t^q + m_1^V F_{1t} - m_4^V F_{2t} + F_{4t}, \qquad (31)$$
$$m_{t_0}^p = m_0^p = Mp_0,$$
$$\dot m_t^q = N_* m_t^p - m_2^V F_{1t} + m_5^V F_{2t} + F_{5t},$$
$$m_{t_0}^q = m_0^q = Mq_0,$$
$$\dot m_t^r = -m_3^V F_{3t} + F_{6t}, \quad m_{t_0}^r = m_0^r = Mr_0,$$

$$\dot p_t^0 = -N_* q_t^0 + F_{1t}V_1^0 - F_{7t}r_t^0 - F_{8t}V_4^0 \qquad (32)$$
$$- F_{9t}V_2^0 - F_{10t}V_6^0 - F_{11t}V_3^0 - F_{12t}V_5^0, \quad p_{t_0}^0 = p_0^0,$$
$$\dot q_t^0 = N_* p_t^0 - F_{1t}V_2^0 + F_{13t}r_t^0 - F_{8t}V_5^0 - F_{14t}V_1^0$$
$$+ F_{15t}V_6^0 - F_{16t}V_3^0 - F_{17t}V_4^0, \quad q_{t_0}^0 = q_0^0,$$
$$\dot r_t^0 = -F_{3t}V_3^0 - F_{18t}V_1^0 + F_{19t}V_2^0 + F_{20t}V_5^0,$$
$$r_{t_0}^0 = r_0^0.$$

Let us analyze in detail the main dynamical effects of the nonlinear components in the correlation model (26)–(28).

6. ANALYSIS OF NONLINEAR STOCHASTIC OSCILLATIONS AND TRENDS

Let us continue our analysis of the stochastic oscillations and trend of the angular velocity r_t (Section 2) for the nonlinear case and the fixed initial condition $m_0^r = r_0$. Direct integration of (31) and (32) enables us to calculate the mathematical expectations and correlation characteristics for the angular velocity of the proper rotation r_t using (26)–(28). Here, the nonlinear components Δm_t^r and ΔD_t^r and their averages over the time $2\pi\omega_*^{-1}$ are

$$\Delta m_t^r = -3b\omega_* d_3\left[m_1^V(m_2^V - m_5^V) - (K_{12}^V \qquad (33)$$

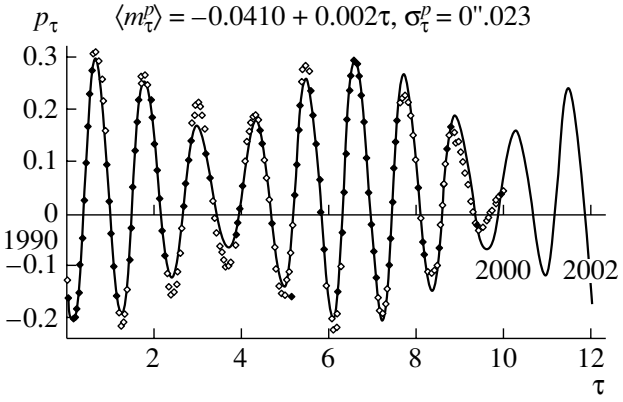

Fig. 1.

$$-K_{15}^V)\big]\sin\omega_* t, \quad \langle\Delta m_t^r\rangle = 0,$$

$$\Delta D_t^r = (3b\omega_* d_3)^2\big[D_1^V(m_5^V - m_2^V)^2 \qquad (34)$$
$$+ (D_2^V + D_5^V - 2K_{25}^V)(m_1^V)^2$$
$$- (K_{12}^V - K_{15}^V)m_1^V(m_5^V - m_2^V)\big]\sin^2\omega_* t,$$
$$\langle\Delta D_t^r\rangle = \frac{9}{2}b^2\omega_*^2 d_3^2\big[D_1^V(m_5^V - m_2^V)^2$$
$$+ (D_2^V + D_5^V - 2K_{25}^V)(m_1^V)^2$$
$$- (K_{12}^V - K_{15}^V)m_1^V(m_5^V - m_2^V)\big].$$

Similarly we can derive the covariance function $\Delta K_{t,t'}^r$.

Comparing with the angular velocity r_t of the proper rotation presented in Section 2 for known initial conditions, we conclude that the correlation between the tidal humps of the first harmonic V_1, V_2 and the bulge V_5 gives rise to harmonic oscillations with frequencies ω_* and $2\omega_*$ with respect to the constant averages $\langle\Delta m_t^r\rangle = 0$ and $\langle\Delta D_t^r\rangle \neq 0$. In this case, there are no correlations between r_t and V_4, V_6, and $K_{4t}^{Vr} = K_{6t}^{Vr} = 0$. The effect of the parameter V_6 is absent. Using (33) and (34) for $m_2^V = m_5^V$ and $K_{12}^V = K_{15}^V$, we obtain

$$\Delta m_t^r = 0, \quad \Delta D_t^r = (3b\omega_* d_3)^2 \qquad (35)$$
$$\times (D_2^V + D_5^V - 2K_{25}^V)(m_1^V)^2\sin^2\omega_* t.$$

Let us extend the findings of Section 2 for the linear theory of stochastic oscillations and the trend of the Earth's pole to the nonlinear case of known initial conditions p_0 and q_0. In this case, taking into account (33)–(35), the equations for Δm_t^p, $\langle\Delta m_t^p\rangle$, Δm_t^q, and $\langle\Delta m_t^q\rangle$ take the form

$$\Delta\dot m_t^p + N_*\Delta m_t^q \qquad (36)$$
$$= -m_4^V\left[\bar D_t^r + \Delta D_t^r + (\Delta m_t^r)^2\right]$$

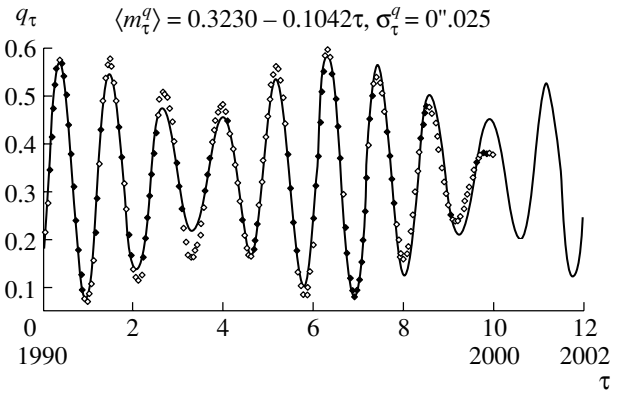

Fig. 2.

$$
\begin{aligned}
&- 3(m_2^V m_6^V + K_{26}^V) d_1 b \omega_*^2 \cos\omega_* t \\
&- 3(m_3^V m_5^V + K_{35}^V) d_1 \omega_*^2 (b' + b'' \cos 2\omega_* t), \\
&\Delta \dot{m}_t^q - N_* \Delta m_t^p \\
&= m_5^V \left[\bar{D}_t^r + \Delta D_t^r + (\Delta m_t^r)^2 \right] \\
&- 3(m_1^V m_6^V + K_{16}^V) d_2 b \omega_*^2 \cos\omega_* t \\
&- 3(m_3^V m_4^V + K_{34}^V) d_2 \omega_*^2 (b' + b'' \cos 2\omega_* t),
\end{aligned}
\tag{37}
$$

$$
\begin{aligned}
\langle \Delta m_t^p \rangle &= -m_5^V \langle \bar{D}_t^r + \Delta D_t^r + (\Delta m_t^r)^2 \rangle N_*^{-1} \\
&+ 3(m_3^V m_4^V + K_{34}^V) d_2 \omega_*^2 b' N_*^{-1},
\end{aligned}
\tag{38}
$$

$$
\begin{aligned}
\langle \Delta m_t^q \rangle &= -m_4^V \langle \bar{D}_t^r + \Delta D_t^r + (\Delta m_t^r)^2 \rangle N_*^{-1} \\
&- 3(m_3^V m_5^V + K_{35}^V) d_1 \omega_*^2 b' N_*^{-1},
\end{aligned}
\tag{39}
$$

where $\bar{D}_t^r$ are determined by the linear correlation theory (Section 2) and Δm_t^r and ΔD_t^r are determined by (33) and (34).

By virtue of (38), (39), and (25), the additional average trend in the p_t and q_t components of the angular velocity is determined by the parameters V_3, V_4, and V_5 and is equal to

$$
\begin{aligned}
\langle \Delta m_t^p \rangle &= \alpha_0^p + \alpha_1^p t + \alpha_2^p t^2, \\
\langle \Delta m_t^q \rangle &= \alpha_0^q + \alpha_1^q t + \alpha_2^p t^2,
\end{aligned}
\tag{40}
$$

where $\alpha_{0,1,2}^{p,q} = \alpha_{0,1,2}^{p,q}(m^{3,4,5}, K^{3,4,5})$ are the zeroth-, first-, and second-order time derivatives of $\langle m_t^{p,q} \rangle$.

Equations (32) represent a linear nonstationary system with random parameters contained linearly. Integrating these equations, we first find the effective influence functions $\tilde{\psi}_{i,t}^{p,q}$ for the parameters V_i and then the analytical expressions for the desired mathematical expectations and correlation characteristics using (26)–(28). The effect of the non-Gaussian behavior of the distributions of random parameters can be studied analogously [10].

7. ANALYTICAL MODELING AND DISCUSSIONS

Special software based on the equations of Sections 4 and 5 has been developed at the Institute for Problems of Informatics. The analytical models are shown in Figs. 1 and 2. The circles present the IERS data [3] and the solid curves, the mathematical expectations. The mean trends in the variables $p_\tau = p(t/T_h)$ and $q_\tau = q(t/T_h)$, where T_h is the time in years, display both constant and linear components. The averaged rms deviations are constant and nearly coincide. Experimental statistical tests have shown that the analytical modeling provides accuracies of $\sim 10\%$ for the linear correlation models and 3–5% for the quadratic correlation model.

When the random parameters $\bar{\mathbf{V}}$ contain some non-correlated parameters with $\mathbf{V} = \mathcal{A}_t \bar{\mathbf{V}}$, where A_t is a linear-transformation matrix, the finite correlation model (26)–(28) for $\bar{\mathbf{V}}$ is simplified considerably since $K_{ij}^{\bar{\mathbf{V}}} = 0$ for $i \neq j$. This approach is helpful when (1)–(3) take into account the tidal bulges and humps of higher zonal harmonics [1, 2].

Using the methods of mathematical statistics [10], the correlation models of the deformable Earth have enabled us to solve the following practical tasks:

(i) for known statistical characteristics of the random parameters $\mathbf{V} = [V_1 \dots V_9]^T$, calculate the statistical characteristics of the p_t, q_t, and r_t components of the angular velocity for various times (including statistical forecasting and identifying anomalous phenomena);

(ii) for known observational data [3], estimate the mathematical expectations, variances, and covariances of the parameters in (1)–(3) and determine their confidence intervals;

(iii) solve mixed problems, when only some of the observed parameters have acceptable accuracy.

8. ACKNOWLEDGMENTS

This work was supported by the Russian Foundation for Basic Research, projects nos. 01-02-17250 and 01-02-00758.

REFERENCES

1. W. Munk and G. Macdonald, *The Rotation of the Earth* (Cambridge Univ. Press, Cambridge, 1960; Mir, Moscow, 1964).
2. H. Moritz and I. I. Mueller, *Earth Rotation: Theory and Observation* (Ungar, New York, 1987; Naukova Dumka, Kiev, 1992).
3. IERS Annual Reports. 1990. July 1991–1999. July 2000 (Central Bureau IERS, Obs. Paris, 2000).

4. L. D. Akulenko, S. A. Kumakshev, and Yu. G. Markov, Dokl. Akad. Nauk **379** (2), 191 (2001) [Dokl. Phys. **46**, 508 (2001)].
5. L. D. Akulenko, S. A. Kumakshev, and Yu. G. Markov, Dokl. Akad. Nauk **382** (2), 199 (2002) [Dokl. Phys. **47**, 78 (2002)].
6. Yu. G. Markov and I. N. Sinitsyn, Dokl. Akad. Nauk **385** (2), 189 (2002) [Dokl. Phys. **47**, 531 (2002)].
7. V. S. Pugachev and I. N. Sinitsyn, *Theory of Stochastic Systems* [in Russian] (Logos, Moscow, 2000).
8. V. S. Pugachev and I. N. Sinitsyn, *Stochastic Differential Systems. Analysis and Filtration* [in Russian] (Nauka, Moscow, 1990, 2nd ed.).
9. V. S. Pugachev, *Theory of Probability and Mathematical Statistics* [in Russian] (Nauka, Moscow, 1979).
10. I.N. Sinitsyn, Dokl. Akad. Nauk **348** (3), 327 (1996) [Phys. Dokl. **41**, 218 (1996)].

Translated by V. Badin

Astronomy Reports, Vol. 47, No. 2, 2003, pp. 81–87. Translated from Astronomicheskiĭ Zhurnal, Vol. 80, No. 2, 2003, pp. 99–106.

A Method for Determining Redshifts from Radio Data

S. A. Tyul'bashev

Pushchino Radio Astronomy Observatory,
Astro Space Center, Lebedev Physical Institute, Moscow, Russia

Received April 1, 2002; in final form, August 21, 2002

Abstract—The possibility of estimating the redshifts of radio sources based on radio continuum observations is demonstrated. Since the pressure exerted on the intergalactic medium by radio lobes is associated only with their total energy, while the pressure exerted on the radio lobes by the intergalactic medium depends on the redshift, the redshift can be estimated. The proposed method does not require the use of standard candles or standard sizes for any features. Consequently, it is free of the influence of cosmological evolution of the radio sources. Our insufficient knowledge of the density and temperature of the intergalactic medium prevents us from applying the method to obtain direct estimates of the distances to extragalactic radio sources. Therefore, a method designed to enable indirect estimation of the source distances has also been developed. © *2003 MAIK "Nauka/Interperiodica"*.

1. INTRODUCTION

All means of determining the distances of extragalactic objects are related one way or another to optical observations. According to [1, 2], three main methods of distance determination can be distinguished. In the first, distances are determined using observations of supernovae. It is assumed that the maximum absolute brightnesses of all supernovae are the same. The second method assumes that the brightest elliptical galaxies in clusters (cD galaxies) all have the same absolute brightness. The third method is associated with determining the redshifts (z) of extragalactic sources. The first two methods are photometric, since they are based on the fact that the luminosity of any object falls off as $1/r^2$ (r is the distance to the object). If the absolute magnitude of an object is known, it is possible to derive its distance from its apparent magnitude. Distance estimates obtained using photometric and spectroscopic (redshift) methods may not coincide.

There are also other methods of distance estimation. In some of these, the observed width of some line in the optical or radio is linked to the absolute magnitude of the galaxy. The methods that are most often used are those of Tully and Fisher [3] (used to determine the distances to spiral galaxies) and of Faber and Jackson [4] (used to determine the distances to elliptical galaxies). Tully and Fisher found a good correlation between the widths of the HI (21 cm) profiles and the absolute magnitudes or diameters of the galaxies studied. The Faber–Jackson method makes use of the correlation between the dispersion of the stellar velocities derived from stellar absorption lines and the absolute magnitudes of the galaxies studied. Other methods relate the surface brightness of some observed feature with its distance. These methods are discussed in more detail together with a number of more exotic methods for distance estimation in the review [5]. We note only that, as a rule, the accuracy of these methods is not high. The main problem, in our view, is that all these methods require the use of standard candles or standard sizes associated with the object studied.

No types of radio source have been found that could serve as standard candles for observations of sources at cosmological distances. This has prevented the use of photometric distance-estimation methods in the radio frequency range. On the other hand, spectral features in the radio frequency range are typically very weak, so that methods based on direct redshift determinations are virtually never used.

Here, we propose a method for deriving redshifts from radio continuum observations of radio sources.

2. THE DISTANCE-DETERMINATION METHOD

The main idea behind deriving redshifts from radio-continuum observations is very simple. Let us suppose we observe a classic radio galaxy such as Cygnus A. It consists of a weak core located at the center of the host galaxy, two jets emerging from the core, and two large radio lobes located at the ends of the jets and placed symmetrically with respect to the core. What determines the total energy of the radio lobes? It seems that this total energy is determined, in the end, only by the accretion rate onto the black hole that lies in the core of the radio source. It may be that

1063-7729/03/4702-0081$24.00

there are additional factors that contribute to the total energy of the radio lobes, but, one way or another, they are all associated with the host galaxy. On the other hand, if these radio lobes have gone beyond the boundary of the host galaxy, their expansion into space is hindered only by the intergalactic medium. Accurate information about the intergalactic medium is sparse. However, it is reasonable to suppose that its characteristics, especially its density, are related primarily with the redshift at which the medium is located. Thus, if two radio galaxies with different accretion rates are observed at the same redshift, the physical dimensions of the radio lobes will be larger for the galaxy with the higher accretion rate. The energy density per unit volume of the radio lobes will be the same. If two radio galaxies have the same accretion rates, the intrinsic dimensions of their radio lobes will depend only on the distances to these objects: the higher the redshift z, the smaller the intrinsic dimensions of the lobes.

When the pressure of the intergalactic gas on the radio lobes is equal to the pressure exerted by the lobes on the intergalactic gas, we can write the simple equation

$$P_{\text{int.}} = P_{\text{ext}}. \tag{1}$$

It follows that, if we can find a way to determine the internal pressure in a radio lobe and the external pressure exerted on the lobe by the extragalactic medium, the possibility arises of directly estimating the cosmological distances to the radio sources associated with these lobes (i.e., the sources' redshifts).

This method would be suitable not only for radio galaxies, but also for quasars. Quasars more typically display only one radio lobe and a bright core. The core can easily be distinguished from the lobe, since the spectrum of the core is flatter than that of the lobe.

If the radio lobe is spherical and its total energy (U_{tot}) is known, then, according to Pacholczyk [6], the internal pressure can be estimated using the formula $P_{\text{int}} = \frac{6}{\pi}\frac{U_{\text{tot}}}{d^3}$ (where $d = d(z)$ is the intrinsic diameter of the lobe, which can be found from θ_{app}, the apparent diameter of the lobe).

However, we are not entirely clear about how to estimate the external pressure exerted by the intergalactic medium on the radio lobe. Let us suppose that the external pressure is determined primarily by the thermal pressure of the external gas and that, according to Pacholczyk [6], $P_{\text{ext}} = \frac{3}{2}nkT$, where $n = n(z)$ is the density of the intergalactic gas, k is the Boltzmann constant, and $T = T(z)$ is the temperature of the intergalactic gas. Equation (1) can then be rewritten in the form

$$\frac{6}{\pi}\frac{U_{\text{tot}}}{d(z)^3} = \frac{3}{2}n(z)kT(z). \tag{2}$$

We can estimate the redshift of the source by solving (2) for z.

Due to the uncertainty in the parameters associated with the external pressure, it is not possible to fully develop a method for direct estimation of the source distances. Therefore, in place of such a direct method, we present below an indirect method for estimating z.

Both P_{int} and P_{ext} contain parameters that depend on z. However, these dependences are complex, and it is not possible to cancel all z-dependent terms on both the right-hand and left-hand sides of (2). Thus, we can write

$$\frac{U^*_{\text{tot}}}{\theta^3_{\text{app}}} = f(z), \tag{3}$$

where U^*_{tot} is the total energy of the radio lobe in the rest frame of the lobe. Whatever method we select to estimate the energy of the lobe, it is very likely that the associated equation will contain terms that depend on the source redshift. Therefore, we estimate the total energy as if the source had zero redshift, so that all z-dependent terms are included in the function $f(z)$. The behavior of $f(z)$ can be derived empirically from observations of real sources with known redshifts. As a result, this method for estimating redshifts is indirect and will work only after an expression relating the internal energy in the radio lobe per unit volume (i.e., the energy density in the lobe) to the redshift of the radio source can be derived. It is also evident that this relation will be an increasing function of z; i.e., larger lobe energy densities will correspond to more distant sources.

Komberg and Smirnov [7] have also proposed a method for estimating source distances from the extended lobes of radio galaxies. They constructed a dependence between the surface brightness per unit area of a radio lobe and the lobe's size for radio galaxies with known redshifts. A good correlation was obtained, at least for radio galaxies with redshifts less than 0.1 (so that cosmological evolution was negligible). Their dependence could be used to derive estimates of the distances for sources with unknown redshifts.

In our proposed method, there is no need for standard candles or standard sizes for any features in the objects studied. Let us suppose, for example, that the radio galaxies undergo strong, non-linear cosmological evolution. This means that it is impossible to derive distances to these sources using classical methods, even if all the sources are standard candles, until we can determine the functional behavior of this cosmological evolution. However, this is not important for our method. The cosmological evolution of the radio galaxies will make sources at various redshifts, on average, brighter or dimmer. However, this will not

be important for our method, since we measure the total energy in the radio lobes. If the radio galaxies at some redshift are overall brighter, this means that they will have, on average, larger lobes. The energy density per unit volume will be determined only by the pressure exerted on the lobe by the intergalactic medium. Thus, our method is free of the influence of possible cosmological evolution of the objects considered.

3. ACCURACY OF THE METHOD

The accuracy of the proposed method for estimating the distances of radio sources is determined by the accuracy with which $U^*_{\rm tot}$ can be estimated. Let us assume that the main contribution to $U^*_{\rm tot}$ is made by the energies of the magnetic field and relativistic particles, as is most likely.

If there is equipartition between the energies of the magnetic field and relativistic particles, the total energy in the radio lobe can easily be estimated. The radio lobes are large (10–1000 kpc) and have long lifetimes (hundreds of millions of years). Consequently, it seems reasonable to suppose on general grounds that energy equipartition should be established. On the other hand, our previous studies [17] have shown that, as a rule, there is no energy equipartition in structures in radio galaxies and quasars that have sizes of up to 1 kpc. Therefore, this question requires further study.

If the energies of the magnetic field and relativistic particles are not in equipartition, we can obtain a correct estimate of $H_\perp$ if a low-frequency cutoff associated with synchrotron self-absorption is observed in the spectrum of the extended radio lobe. Artyukh [8] has developed a method for estimating $H_\perp$ and the density of relativistic electrons. In this method, which is based on the formula of Slysh [9], the accuracy of the $H_\perp$ estimate is determined by the accuracy with which the angular dimensions of the source are known ($H_\perp \sim \theta^4$). Artyukh [8] proposed to estimate the angular size of a compact radio source from the power spectrum of scintillations observed at low frequencies, which yields uncertainties in the source angular size of 30–100%. It follows that the corresponding accuracy of $H_\perp$ is very low (1.3^4–2^4, or a factor of 3–16)—an order of magnitude for the field and two orders of magnitude for the total magnetic-field energy. Roughly the same situation arises for estimation of the relativistic-particle energy.

Thus, using observations of interplanetary scintillations to estimate the source angular size leads to very large uncertainties in the estimates of $H_\perp$. However, aperture-synthesis systems such as the Very Large Array yield good UV coverage and high image dynamic ranges, substantially improving the accuracy of angular-size estimates ($\approx$10%). In this case, the uncertainty in the field estimate will be no more than a factor of 1.5, corresponding to an uncertainty in the field energy of about a factor of 2. Thus, the resulting estimates of z derived from $f(z)$ will also differ from their true values by up to a factor of 2. An uncertainty of a factor of 2 for distance determinations is, of course, large. Note, however, that this uncertainty can be decreased by increasing the accuracy of the source angular-size estimates. For example, if it is possible to measure the angular size of a radio lobe with an uncertainty of no more than 3%, the uncertainty in z will be only 30%, comparable with the accuracies of classical methods for estimating the distances of cosmological objects.

Unfortunately, there are additional factors that can distort the $f(z)$ relation in unpredictable ways. Two of these are the most important.

First, we have assumed that the internal pressure of the lobe and the external pressure exerted by the intergalactic gas are in equilibrium. This is a serious assumption for which there are no equally serious arguments to support it. Of course, there are indirect arguments. For example, it is known that the active phase of a galactic nucleus lasts about 100 million years, while the radio lobes are longer-lived formations. Therefore, it seems reasonable to suppose that an equilibrium between the media inside and outside the radio lobe should have been established. The case of ongoing expansion of a radio lobe in the course of its evolution is more complex. In this case, we must consider not a hydrostatic approximation (as we have done), but a hydrodynamical one. Then, Eq. (1) will remain unchanged, while the left-hand side of (2) will contain terms associated with the expansion speed of the lobe. However, it would be premature to complicate the distance-estimation scheme before obtaining some observational verification of the method.

Second, the radio sources could be located in superclusters or clusters of galaxies or could be simply isolated objects. We have implicitly assumed that the temperature and density of the intergalactic gas depends only on the redshift and not on the region surrounding the radio source. There are at least two possible ways to resolve this problem. The first is to divide samples of the radio galaxies under study into galaxies in clusters, in groups, and so forth, and then construct the relations between the energy density per unit volume and distance separately for the different subsamples. The second approach is more fundamental. If there is simply no clear dependence of the density and temperature of the intergalactic medium on the redshift, we can try to estimate the required densities and temperatures, for example, from X-ray observations. We can then insert the densities and temperatures derived observationally in the right-hand side of (2) and estimate the redshift from the

left-hand side of (2), since it contains the observed angular size of the radio lobe, which is related to its intrinsic linear size by the redshift.

Only observational tests can enable us to determine the contributions to the errors in the z estimates made by these two factors. We note only that we are considering here a simplified scheme and are not justified in making it too complex until we have additional information from real observations to use as a basis for this.

4. SOURCE SELECTION

There exist two main criteria for the construction of initial samples to be used to determine the $f(z)$ relation.

(1) To estimate the total energy in the radio lobes, we must know the physical conditions in these formations. If the main contribution to the total energy is made by the energies of the magnetic field and relativistic particles, as is most likely, we can use the method developed by Artyukh [8] for spherical sources uniformly filled with magnetic fields and relativistic particles. There also exist analogs for this method developed by Artyukh and Chernikov [10] for the case of non-uniform distributions of the field and particles. This second method requires very precise knowledge of the source spectrum, which is unfortunately very difficult to obtain observationally.

Thus, we propose to use the method of [8] to estimate the total energy. The main condition that must be satisfied in this case is the presence of an observable low-frequency cutoff in the radio spectrum. We can use the spectrum near the cutoff to estimate the magnetic field, use this value and the optically-thin part of the spectrum to estimate the relativistic-electron density, then finally use these results to estimate the energies of the magnetic field and relativistic particles.

The cutoff in the spectrum due to synchrotron self-absorption is determined by the angular size and flux density of the lobe. We can easily estimate the maximum frequency beyond which the cutoff begins using the formula of Slysh

$$\nu_{\max} = (5\times 10^{10})^{1/5} K(\gamma)^{-1/5}\theta^{-4/5} \times S^{2/5}(1+z)^{1/5} H_\perp^{1/5}, \quad (4)$$

where $\nu_{\max}$ is in MHz, $K(\gamma)$ is a coefficient of order unity tabulated by Pacholczyk [6], θ is the apparent (observed) angular size of the lobe in arcseconds, S is the lobe flux density in Jy, and $H_\perp$ is the magnetic field in G. We can see that this frequency depends most strongly on the angular size of the lobe, less strongly on the lobe flux density, and only slightly on the remaining parameters. If we take a typical redshift $z = 2$ and a spectral index for the radio lobe of $\alpha = 1$ ($S \sim \nu^{-\alpha}, \gamma = 2\alpha + 1$), formula (4) can be written in the form

$$\nu_{\max} = 172 H_\perp^{1/5} S^{2/5}\theta^{-4/5}. \quad (5)$$

Estimates of $\nu_{\max}$ for various values of $H_\perp$, S, and θ are presented in Table 1.

To elucidate which values of $\nu_{\max}$ in this table are the most plausible, we inspected a field with a total size of 20 square degrees from the FIRST catalog [11]. The angular resolution in the survey was about 5″ at 1.5 GHz. Most of the sources do not show any signs of structure. At the same time, there are many double sources in the field (radio galaxies?); in most cases, the two components are separated by distances from several arcseconds to several tens of arcseconds and do not show any indications of internal structure. This means that the sizes of these components are less than 5″.

The FIRST survey with its 5″ angular resolution is currently unique, and there is no realistic possibility of obtaining spectra for all the compact components appearing in this survey. Therefore, if we wish to test the capabilities of our method, we are forced to turn to other catalogs that have angular resolutions of arcminutes or even tens of arcminutes. If a cutoff is observed in the integrated spectrum, we can construct rough approximations to the spectra of individual components if we adopt some additional assumptions. According to [12], most modern catalogs contain from one to ten sources per square degree. This enables us to select from the FIRST catalog only those sources for which it is possible to construct integrated spectra over a broad frequency range. Integrated source counts based on the FIRST catalog are presented in [11], which indicate that, on average, $\simeq 3$ sources per square degree have flux densities ≥ 100 mJy at 1.5 GHz. We can easily estimate that a source with a spectral index $\alpha = 1$ and a flux density of 100 mJy at 1.5 GHz will have a flux density of ~ 4 Jy at 38 MHz. We have chosen 38 MHz here because high-sensitivity observations are available at this low frequency [13].

Values of $\nu_{\max}$ in Table 1 that are the most plausible are delineated in bold. Thus, as we expect, the synchrotron self-absorption cutoffs in the spectra of most of the radio lobes with angular sizes of 1″ will occur at frequencies from 10 to 40 MHz. We must also bear in mind that the peak frequency is given in the rest frame of the source. Since the sources can be located at large cosmological distances, we must apply an additional correction by dividing the values in Table 1 by $1 + z$, which will decrease the value of $\nu_{\max}$.

Unfortunately, there is no aperture-synthesis system operating at such low frequencies that has the

Table 1. Estimates of $\nu_{\max}$ in MHz for various S, $\theta_{\rm app}$, $H_\perp$

S, Jy	$\theta_{\rm app}$				H, G
	0.1″	1″	10″	100″	
	$\nu_{\max}$				
0.1	44	7	1	0.2	10^{-5}
1	109	**17**	3	0.4	
10	273	**43**	7	1	
0.1	26	4	0.7	0.1	10^{-6}
1	65	**10**	2	0.3	
10	164	**26**	4	0.6	

required angular resolution. We can easily estimate that the baseline lengths required in order for an interferometer operating at 10 MHz to have an angular resolution of 1″ are about 1500 km. The best characteristics in terms of angular resolution attained at low frequencies are possessed by the Ukrainian URAN system [14], which provides an angular resolution of 1.5″ at 20 MHz, and this instrument could, in principle, be suitable for our study. However, judging from published results, the low sensitivity of this system drastically limits its usefulness, since our sources will have low flux densities at low frequencies.

(2) We require that the radio lobe be beyond the edge of the host galaxy. The host galaxies of various types of radio sources can be either elliptical or spiral. Therefore, it seems expedient to consider a distance from the nucleus to the lobe that is clearly larger than the distance from the plane of the host galaxy to the boundary of its corona. It seems reasonable to adopt 30 kpc for this distance, so that the distance between the centers of the radio lobes ($l_{\rm true}$) will be 60 kpc. In this case, the observed angular distance between the two radio lobes will depend on the redshift and the deceleration parameter q_0. According to the handbook of Lang [1], we can estimate the apparent angular size of the source if q_0 is known:

$$\theta_{\rm app} = \frac{l_{\rm true}(1+z)^2}{D_L}, \qquad (6)$$

$$D_L = \frac{c}{H_0 q_0^2}(q_0 z + (q_0 - 1)[-1 + \sqrt{2q_0 z + 1}]), \qquad (7)$$

where D_L is the photometric distance and H_0 is the Hubble constant.

Using (6) and (7), we can estimate the apparent angular separation of the two radio lobes for various values of q_0 if we assume that the true separation is 60 kpc. Estimates of the apparent angular separations between the lobes are given in Table 2. When performing these calculations, we adopted the values $H_0 = 75\ {\rm km\,s^{-1}\,Mpc^{-1}}$ and $c = 300\,000$ km/s.

Table 2. Estimates of $\theta_{\rm app}$ as a function of z and q_0 for $l_{\rm true} = 60$ kpc

q_0	z							
	0.1	0.3	0.5	1	2	3	5	10
	$\theta_{\rm app}$							
1/2	36″	17″	14″	12″	14″	16″	22″	36″
1	36″	16″	13″	10″	11″	13″	14″	24″

We can see from Table 2 that apparent angular separations of the lobes of 20″–25″ are quite sufficient for us to work with redshifts that are observationally accessible at the present time. Unfortunately, such separations may substantially limit the number of radio sources in the sky that are suitable for redshift analyses using our method. The estimates of the apparent angular separations also indicate that, if an image obtained using an aperture-synthesis system with good angular resolution shows a core, jets, and lobes, this does not necessarily mean that the lobes have extended beyond the edge of the host galaxy, even if the observed angular separation between the lobes exceeds an arcsecond.

We attempted to construct the $f(z)$ relation for sources that had been studied earlier using scintillation methods. Our previous papers [15–17] present estimates of the physical conditions in a large sample of compact steep-spectrum sources. In all, we were able to estimate the physical conditions (i.e.,

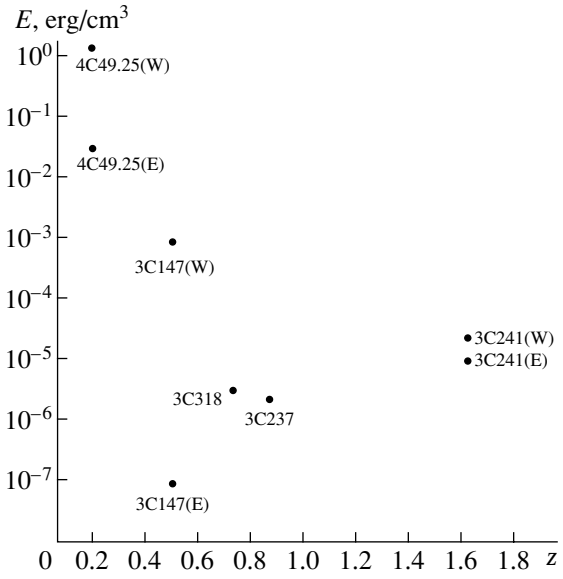

Figure

Table 3. Estimates of physical parameters in the radio lobes

Source	z	Ω, square deg	α	E_H, erg/cm^3	E_e, erg/cm^3	$\theta''_{\rm app}$	l, kpc
3C147Q(W)	0.545	0.17×0.05	1.1	10^{-3}	2×10^{-11}	$0.09''$	0.44
3C147Q(E)	–	0.5×0.5	1.3	10^{-7}	2×10^{-10}	0.49	2.5
3C237G	0.877	0.2×0.1	1.4	2×10^{-6}	5×10^{-9}	0.78	4.4
3C241G(W)	1.617	0.1×0.1	1.1	3×10^{-5}	8×10^{-10}	0.36	2
3C241G(E)	–	0.1×0.1	1.6	10^{-5}	10^{-8}	0.46	2.6
3C318G	0.752	0.062×0.043	1.5	10^{-9}	4×10^{-6}	0.5	2.7
4C49.25G(W)	0.206	0.23×0.16	1.4	2	5×10^{-15}	0.94	2.7
4C49.25G(E)	–	0.125×0.09	0.8	4×10^{-2}	6×10^{-14}	1.8	5.2

magnetic-field strength, magnetic-field energy, density and energy of the relativistic electrons) of 42 sources. A number of sources show the classical structure for radio galaxies and quasars, with a flat-spectrum core, jet, sometimes a counterjet, and either one or two lobes. We expect that, if the jets are not collimated, the role of the galactic (interstellar) medium is insignificant. Consequently, the lobes propagate in the intergalactic medium, so that we can derive the function $f(z)$. As indicated above, the chosen separation of 60 kpc is somewhat arbitrary and guarantees that the lobes propagate in the intergalactic medium. In reality, this distance may be several times smaller at least.

We selected the most "promising" sources to derive the $f(z)$ relation. Data on these sources are given in Table 3. The first column gives the name of the source. The letters Q and G denote quasar and galaxy, while W and E denote the western or eastern lobe of the source. The second column presents the source's redshift, the third the angular size of the lobes, and the fourth the spectral index in the optically thin part of the spectrum. The fifth and sixth columns contain the energy densities of the magnetic field and relativistic particles. The values of these energy densities were obtained by recalculating the values of [17] applying a correction for the redshift. The seventh and eighth columns give the apparent angular distance from the nucleus to the center of the radio lobe and the intrinsic distance obtained by assuming $q_0 = 1/2$. The information for the first six columns is taken from [17], and the references can be found therein. Column seven was derived from values in [17] and the references therein. The figure shows a plot of the total energy per unit volume as a function of the redshift.

Two facts stand out. The first is that equipartition of the energy densities does not hold for the radio galaxies and quasars for which we have estimates of the physical parameters for both lobes. It is clear from general considerations that a required (but not sufficient) criterion in order for the lobe to be propagating in the intergalactic medium is that there be equipartition between the two energy densities. The second is that we don't see any hint of the relation for which we are searching. As is noted above, we would expect *a priori* some dependence such that, the higher the redshift, the higher the energy density in the lobes. This means that it is crucial to select sources for which the apparent angular separation of their lobes exceeds $20''$.

5. CONCLUSION

(1) It is possible to estimate the distance to a radio source if its radio lobes have propagated beyond the edge of the host galaxy and interact only with the intergalactic medium. This direct method for distance estimation can be applied only when we have good estimates of the parameters of the intergalactic medium (its temperature and density).

(2) Existing estimates of the temperature and density of the intergalactic medium have large uncertainties; in particular, there is no good theory for the cosmological evolution of the intergalactic medium. Therefore, we have proposed an indirect distance-estimation method that is based on the method of direct distance estimation. It is proposed to construct a curve relating the energy density in a lobe with its redshift, with the redshifts taken from optical observations. After this relation has been constructed, it can be used to estimate the distances of objects with unknown redshifts. A similar method was suggested in [7].

Our distance-estimation method is very simple to use. The only requirements are the availability of radio observations with angular resolution of the order of $1''$, the presence of an observable low-frequency

cutoff in the lobe spectrum due to synchrotron self-absorption, and good estimates of the angular dimensions of the lobes, since uncertainty in this quantity dominates the uncertainty in the corresponding estimates of z. In addition, we must be sure that the radio lobes are located beyond the limits of the host galaxy, which we can judge indirectly based on the angular separation between the two lobes ($>20''-25''$), evidence for equipartition of the magnetic and particle energy densities in the lobes and a near spherical shape for the lobes.

(3) The main merit of the proposed method is that it excludes the influence of possible cosmological evolution of the radio galaxies, since it does not require the use of standard candles in the radio.

(4) In connection with the fact that there are currently no low-frequency surveys with angular resolutions of $1''$ or better, it is not feasible to try to derive large numbers of redshift estimates, since the synchrotron self-absorption cutoffs in the lobe spectra will not be observed. This should be become possible after the construction of the LOFAR low-frequency aperture synthesis system.

6. ACKNOWLEDGMENTS

The author is grateful to V. I. Shishov for comments on the workshop that stimulated him to prepare this work for publication, to P. A. Chernikov for discussions that facilitated the formulation of the solution to the problem of searching for redshifts using radio-continuum observations of the sources, and to B. V. Komberg for discussions about distance determinations for extragalactic sources. The author also thanks R. D. Dagkesamanskiĭ for a preliminary review of the manuscript and a number of interesting comments that made it possible to improve its content and readability. Finally, thanks are due to G. E. Tyul'basheva, L. B. Potapova, and O. I. Malov for help in processing the manuscript. This study was supported by the Russian Foundation for Basic Research (project no. 01-02-16191).

REFERENCES

1. K. R. Lang, *Astrophysical Formulae: A Compendium for the Physicist and Astrophysicist* (Springer-Verlag, Berlin, 1974; Mir, Moscow, 1978).
2. Yu. N. Efremov, *Physical Encyclopedia* (Moscow, 1994), Vol. 4, p. 284.
3. R. B. Tully and J. R. Fisher, Astron. Astrophys. **54**, 661 (1977).
4. S. M. Faber and R. E. Jackson, Astrophys. J. **204**, 668 (1976).
5. B. V. Komberg, Preprint No. 1151, IKI (1986).
6. A. G. Pacholczyk, *Radio Galaxies: Radiation Transfer, Dynamics, Stability and Evolution of a Synchrotron Plasmon* (Pergamon, Oxford, 1977).
7. B. V. Komberg and M. A. Smirnov, Astrofizika **22**, 257 (1985).
8. V. S. Artyukh, Tr. Fiz. Inst. Akad. Nauk SSSR **189**, 223 (1988).
9. V. I. Slysh, Nature **199**, 682 (1963).
10. V. S. Artyukh and P. A. Chernikov, Astron. Zh. **78**, 20 (2001) [Astron. Rep. **45**, 16 (2001)].
11. R. H. Becker, R. L. White, and D. J. Helfand, Astrophys. J. **450**, 559 (1995).
12. H. Andernach, *Astronomy from Large Databases-II,* Ed. by A. Heck and F. Murtagh, ESO Conf. Work. Proc., Vol. 43, p. 185 (1992).
13. S. E. G. Hales, E. M. Waldram, N. Rees, and P. J. Warner, Mon. Not. R. Astron. Soc. **274**, 447 (1995).
14. A. V. Men', S. Ya. Braude, S. L. Pashkovskiĭ, *et al.*, Pis'ma Astron. Zh. **22**, 428 (1996) [Astron. Lett. **22**, 385 (1996)].
15. V. S. Artyukh, S. A. Tyul'bashev, and P. A. Chernikov, Astron. Zh. **76**, 3 (1999) [Astron. Rep. **43**, 1 (1999)].
16. S. A. Tyul'bashev and P. A. Chernikov, Astron. Zh. **77**, 331 (2000) [Astron. Rep. **44**, 286 (2000)].
17. S. A. Tyul'bashev and P. A. Chernikov, Astron. Astrophys. **373**, 381 (2001).

Translated by D. Gabuzda

Astronomy Reports, Vol. 47, No. 2, 2003, pp. 88–98. Translated from Astronomicheskiĭ Zhurnal, Vol. 80, No. 2, 2003, pp. 107–117.

The Chemically Distinct Nucleus and Structure of the S0 Galaxy NGC 80

O. K. Sil'chenko[1], S. E. Koposov[1], V. V. Vlasyuk[2], and O. I. Spiridonova[2]

[1] *Sternberg Astronomical Institute, Universitetskiĭ pr. 13, Moscow, 119992 Russia*

[2] *Special Astrophysical Observatory, Russian Academy of Sciences, pos. Nizhniĭ Arkhyz, Karachaĭ-Cherkessia, Russia*

Received April 3, 2002; in final form, May 23, 2002

Abstract—The giant lenticular galaxy NGC 80, which is the brightest member of a rich group, possesses a central evolutionarily-distinct region: the stars in the nucleus and in a circumnuclear ring of radius 5″t–7″ have a mean age of only 7 Gyr, whereas the stellar population of the bulge is older than 10 Gyr. The nucleus of NGC 80 is also chemically distinct: it is a factor of 2–2.5 richer in metals than its immediate neighborhood and is characterized by a high magnesium-to-iron abundance ratio [Mg/Fe] ≈ +0.3. The global stellar disk of NGC 80 has a two-tiered structure: its outer part has an exponential scale length of 11 kpc and normal surface density, while the inner disk, which is also exponential and axisymmetric, is more compact and brighter. Although the two-tiered structure and the chemically distinct nucleus obviously have a common origin and owe their existence to some catastrophic restructuring of the protogalactic gaseous disk, the origin of this remains unclear, since the galaxy lacks any manifestations of perturbed morphology or triaxiality. © *2003 MAIK "Nauka/Interperiodica".*

1. INTRODUCTION

Circumnuclear star-forming rings in galaxies are a spectacular phenomenon and are especially prominent on high-resolution images taken, e.g., by the Hubble Space Telescope (see NGC 4736 in [1] and NGC 7742 in [2] and many other galaxies). The nature of this phenomenon is now believed to be well understood, mainly owing to the efforts of Buta [3, 4]. Since circumnuclear rings are most often found in barred galaxies, it seems likely that the gas that flows along the bar from the outer regions of the disk toward the center accumulates in the region of the inner Lindblad resonance, becoming denser and more compressed, resulting in a burst of star formation. However, rings are also found, albeit less frequently, in galaxies without bars. To explain such cases, the presence of a triaxial halo (NGC 7217 [5]) or transient bars that have disappeared by the time of the observations have been hypothesized [6, 7]. However, it remains unclear whether a circumnuclear ring can develop in an absolutely axisymmetric galaxy; e.g., in a galaxy with regular round isophotes at all galactocentric radii. We have suggested a scenario that does not directly involve the effect of a triaxial potential [8].

When studying chemically peculiar central regions in nearby galaxies, we have come up against the complex structure of isolated compact circumnuclear stellar disks: the stellar populations at the very centers of these disks are often on average 2–3 Gyr older that the populations at the disk edges, 100–400 pc from the center (NGC 1023 [9], NGC 7331 [10]). Moreover, both populations appear to be about 10–12 Gyr younger than the population of the neighboring bulge regions, leading us to conclude that the circumnuclear disks formed during relatively recent bursts of star formation that were efficient and brief (shorter than 1 Gyr) in the core and continued for several Gyr at the periphery of the circumnuclear disk.

Since several gigayears make up an appreciable fraction of the total age of the galaxy and since our estimates suggest that chemically distinct nuclei can be found in 25–50% of all early-type disk galaxies, a diligent observer has a real chance of catching a galaxy at the time when a burst of star formation has already finished in its nucleus but is ongoing at the periphery of the circumnuclear disk. It is at this time that the galaxy possesses a circumnuclear ring.

The most certain way to distinguish such "relic" rings from rings that form in a quasi-stationary way at the inner Lindblad resonances of bars is that they can be found in round galaxies viewed face-on. We have already had one successful such attempt when we found a ring of HII regions with a radius of just under 1 kpc in the E0 galaxy NGC 759 [11]. This was by no means a blind search: Wilkind *et al.* [12] had earlier reported the discovery of a rapidly rotating molecular gas torus with a total mass of $2.4 \times 10^9 M_\odot$ in this elliptical galaxy, which by itself is a unique phenomenon. We used two-dimensional spectroscopy and surface photometry to analyze the structure of

1063-7729/03/4702-0088$24.00

the stellar component and verified that the massive, extended, spheroidal subsystem contains a compact stellar circumnuclear disk embedded in it, where active star formation is ongoing at a considerable galactocentric distance. We thus caught a chemically distinct central stellar system at the very time of its formation in NGC 759.

In the current paper, we report a second discovery of a ring of young stars in an early-type round galaxy. This discovery was almost accidental, except for the fact that we had listed the galaxy as a candidate for a galaxy possessing a chemically distinct nucleus [13]. Here, we analyze our results for the giant lenticular galaxy NGC 80.

The main global parameters of the galaxy are listed in Table 1. It is the brightest member of either a rich group (the RC1 catalog) or a poor cluster (the UGC catalog): the aggregate contains nine NGC galaxies brighter than 16^m ($M_B < -18.5$) of various morphological types within several arcmin, or half a megaparsec, of each other. NGC 80 is not located at the geometric center of the group but somewhat to the side. This lenticular galaxy does not exhibit peculiarities of any kind: it has a very red integrated color, as expected for a bright, early-type galaxy (Table 1, see also [14]), no emission lines in the spectrum of its nucleus, and no detected neutral hydrogen [15]. The galaxy has virtually perfectly round isophotes, and attempts to measure its rotation have yielded an upper limit of $v_{\rm los,max} < 15$ km/s for the line-of-sight projection of the rotational velocity [16], indicating that the galaxy appears symmetric and must be viewed face-on. We have performed both two-dimensional spectroscopy and surface photometry of NGC 80, and below we report results that improve our understanding of this interesting object.

Table 1. Global parameters of NGC 80

Morphological type (NED)	SAO
R_{25}	21 kpc
B_T^0 (RC3)	13.03
M_B	−21.43
$(B-V)_T^0$ (RC3)	0.94
$(U-B)_T^0$ (RC3)	0.64
V_r (NED)	5698 km s^{-1}
Distance (LEDA)	78 Мпк ($H_0 = 75$ km s^{-1} Mpc^{-1})
Inclination (LEDA)	28^o
PA_{phot}	?

2. OBSERVATIONS AND DATA REDUCTION

We observed the central part of NGC 80 on August 17, 1996, with the Multi-Pupil Field Spectrograph (MPFS) mounted at the primary focus of the 6-m telescope of the Special Astrophysical Observatory (SAO) of the Russian Academy of Sciences (see [17] for a description of the instrument). Our observations covered the spectral region of the MgIbλ5175 absorption line (wavelength interval 4880–5650 Å) with a reciprocal dispersion of 1.6 Å pixel (a spectral resolution of about 4 Å) and a seeing equal to 2.5″. We observed the object over a one-hour exposure time and then obtained a 20 min exposure of an "empty" area of sky to be subtracted from the integrated object frame after normalization and smoothing. The detector used was a 520 × 580 CCD manufactured by the Russian company Elektron. During the MPFS observations, an 8 × 12 array of microlenses constructs a matrix of pupils that is used as the input for the diffraction spectrograph. This configuration enables up to 96 spectra to be recorded simultaneously, each corresponding to a spatial element of the galaxy image. In our case, each element had a size of 1.6″ × 1.6″. We calibrated the wavelength scale using a separate exposure of a He-Ne-Ar lamp spectrum and corrected the spectra for vignetting and the different transmissions of the microlenses using a spectrum of the morning sky. The main stages of the data reduction—bias subtraction, cosmic-ray removal, extraction of the one-dimensional spectra from the frame, and construction of the two-dimensional surface-brightness distributions and velocity fields—were carried out using a software package developed at the SAO [18].

We used the MPFS observations at 4880–5650 Å to analyze the radial dependences of the equivalent widths of absorption lines, and also to construct the two-dimensional stellar radial-velocity field at the center of the galaxy. We achieved the first task by summing spectra within concentric rings centered on the nucleus of the galaxy with widths and a radius step of 1.6 arcsec; i.e., equal to the size of a spatial element. This method enabled us to maintain an approximately constant signal-to-noise ratio as the radius increased, which is impossible, for example, in long-slit observations. We then computed the $H\beta$, Mgb, Fe 5270, and Fe 5335 line indices in the well-known Lick system [19]. Detailed model computations in the context of models of old stellar populations are available for these strong absorption lines [20, 21].

To construct the two-dimensional stellar radial-velocity field at the center of the galaxy, we cross-correlated the spectrum of each spatial element with

Table 2. Photometric observations of NGC 80

Date	Telescope	Filter	Exposure time, min	Seeing, arcsec	Scale, arcsec/pixel
Nov. 29, 1997	1.2 m, OHP	B	10	3.1	0.69
Nov. 29, 1997	1.2 m, OHP	V	5	2.8	0.69
Nov. 29, 1997	1.2 m, OHP	R	5	2.5	0.69
July 18, 2001	1 m, SAO	V	30	1.9×2.3	0.27×0.37
July 18, 2001	1 m, SAO	R	35	1.8×2.2	0.27×0.37
Aug. 16, 2001	1 m, SAO	B	20	3.2	0.27×0.37
Aug. 16, 2001	1 m, SAO	V	10	2.9	0.27×0.37
Aug. 16, 2001	1 m, SAO	R	10	2.6	0.27×0.37
Aug. 16, 2001	1 m, SAO	I	15	2.8	0.27×0.37
Aug. 17, 2001	1 m, SAO	B	20	2.2	0.27×0.37
Aug. 17, 2001	1 m, SAO	V	10	2.0	0.27×0.37
Aug. 17, 2001	1 m, SAO	R	10	1.8	0.27×0.37
Aug. 17, 2001	1 m, SAO	I	10	1.8	0.27×0.37

the spectra of K0–K2 giants observed on the same night and with the same instruments as the galaxy, after subtracting the continuum and converting the results to a velocity scale. We monitored the accuracy of the wavelength scale and the zero point of the measured velocities using observations of the λ5577 Å night-sky line. We estimate the accuracy of individual stellar radial-velocity measurements to be 20 km/s and the accuracy of the derived equivalent widths in the azimuthally averaged spectra to be 0.1 Å. In this paper, we will discuss only the properties of the stellar population. Our analysis of the existing data indicated that the kinematic properties of NGC 80 require further study.

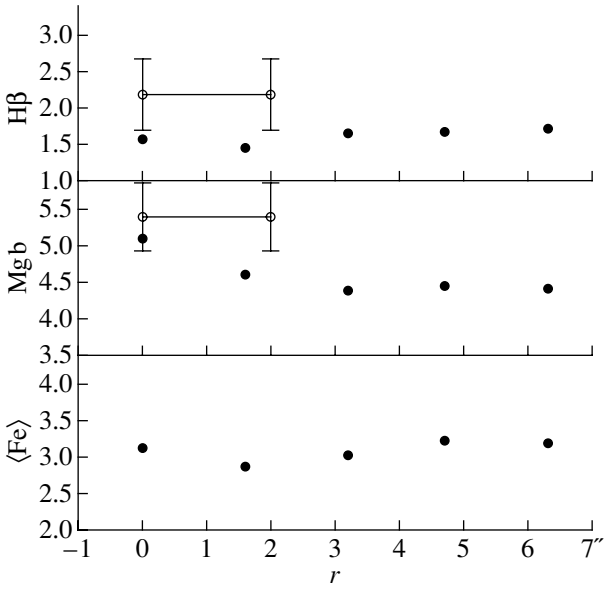

Fig. 1. Radial variations of the azimuthally averaged measurements of the Hβ, Mgb, and $\langle$Fe$\rangle \equiv$ (Fe5270 + Fe5335)/2 absorption-line indices in NGC 80 based on our data (filled circles). For comparison, we have also plotted the measurements of Trager *et al.* [24] made in a $2'' \times 4''$ aperture (open circles with error bars).

We conducted photometric observations of NGC 80 in July–August 2001 with the 1-m Zeiss telescope of the SAO. The detector used was a 520×580 Russian-made Elektron CCD with 18×24 μm rectangular pixels. After reduction to square pixels, we obtained a 397×580 image with a scale of $0.37''$ per pixel. We calibrated the magnitudes to the standard Johnson–Cousins system by comparing our data with the aperture photometry of Poulain [22]; we also observed Landolt [23] photometric standards on one of the nights (August 17, 2001). Table 2 gives a detailed log of the observations. In addition to our own data, we used FITS data taken from the HYPERCAT archive of extragalactic data. These photometric data were obtained at the 1.2-m telescope of the Observatoire de Haute-Provence (OHP) under very modest seeing conditions (about $3''$) and with a rather coarse scale of $0.7''$/pixel, but they are deeper than our photometry in terms of limiting magnitude.

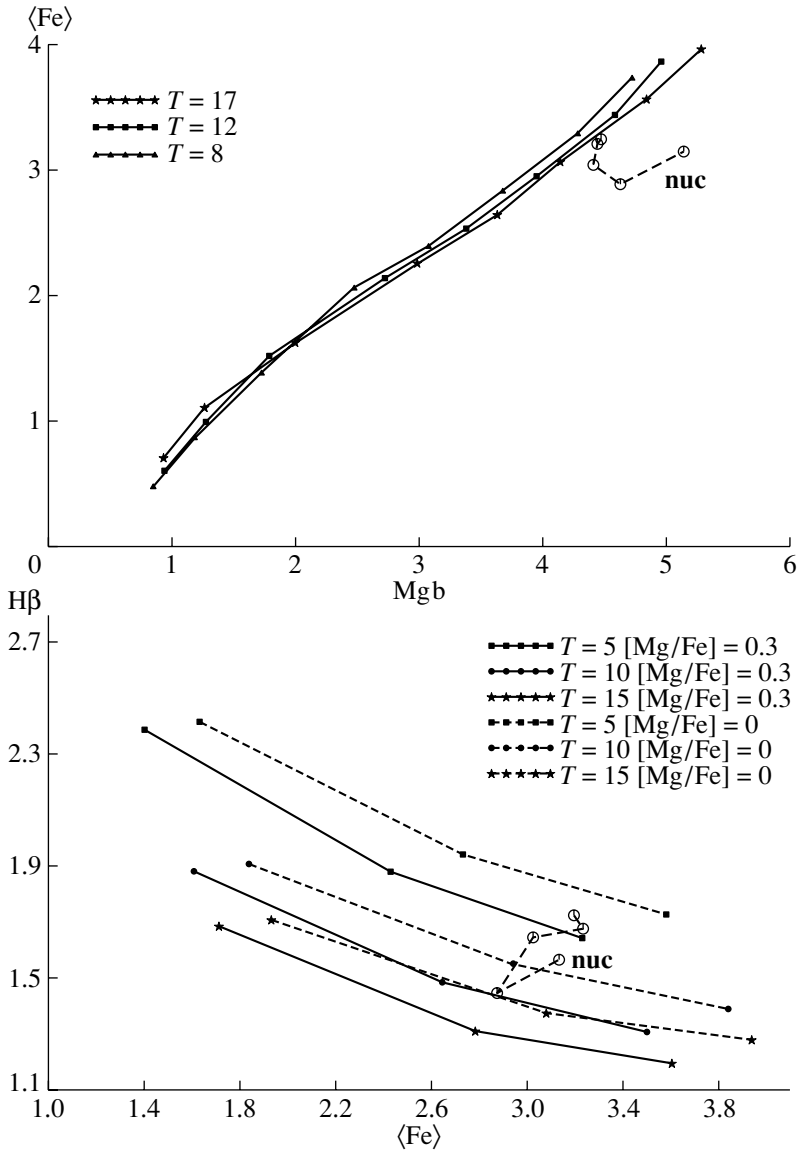

Fig. 2. Index–index diagnostic diagrams for the azimuthally averaged measurements for NGC 80 (large open circles). The MPFS data are taken with a step of 1.6″ in galactocentric radius and are connected by the dashed line in order of increasing R. The nucleus is indicated as "**nuc**." The small symbols connected by solid lines (or by solid lines for [Mg/Fe] = +0.3 and dashed lines for [Mg/Fe] = 0 in the lower diagram) represent models for stellar populations of the same age adopted from [20] (upper) and [21] (lower). The age T of each model is indicated in Gyr. The model metallicities corresponding to the sequence of small symbols connected by lines are (from right to left): +0.50, +0.25, 0.00, −0.22, −0.50, −1.00, −1.50, and −2.00 for models [20] and +0.4, 0.0, and −0.7 for models [21].

3. THE CHEMICALLY DISTINCT NUCLEUS AND "YOUNG" RING AT THE CENTER OF NGC 80

Figure 1 shows the radial variation of the Lick indices measured for the integrated spectra of annular rings in the radius interval 0″–7″. We can see that the iron index ⟨Fe⟩ remains virtually constant with radius and the observed fluctuations within 2.9–3.2 Å confirm the 0.1 Å accuracy of the individual estimates. However, the magnesium index exhibits a prominent 0.7 Å discontinuity nearly coincident with the unresolved nucleus of the galaxy. Beyond the nucleus (whose effect in the case of 2.5″ seeing becomes negligible at $R \geq 3''$), the radial profile of the magnesium index flattens, and becomes fairly constant in the "bulge." Thus, Fig. 1 leads us to conclude that the nucleus of NGC 80 is chemically distinct from the bulge. If interpreted in terms of the models for old stellar populations suggested by Worthey [20], a 0.7 Å

discontinuity in the Mgb index corresponds to about a twofold variation of the mean stellar metallicity.

However, the variations of a single index are degenerate with respect to the effects of the age and metallicity of the stellar population: a decrease in either parameter results in a decrease in the equivalent widths of metal absorption lines and an increase in the equivalent widths of hydrogen absorption lines (see, e.g., [25]). Therefore, to remove this degeneracy and determine both characteristics simultaneously, we must compare the observational data with models for the integrated spectra of stellar populations in "index–index diagrams." In this case, the above estimate of the metallicity variation corresponding to $\Delta\mathrm{Mgb} = 0.7$ Å is valid only if the stellar populations in the nucleus and bulge have the same mean ages.

We will first estimate the magnesium-to-iron abundance ratio. This is necessary in order to correctly choose a system of models for the age estimation. Figure 2a shows a ($\langle$Fe$\rangle$, Mgb) diagram comparing our data with Worthey's [20] models for the solar magnesium-to-iron abundance ratio [Mg/Fe] = 0. On this diagram, model isochrones along which the metallicity [Fe/H] varies from -2 to $+0.5$ form a narrow beam, and it is immediately apparent that the nucleus of NGC 80 deviates significantly to the right of the model band, which includes various stellar populations with [Mg/Fe] = 0. Most of the elliptical galaxies behave in the same way [26], which is indicative of magnesium (and other α-process elements) being overabundant relative to iron. Modern concepts about the chemical evolution of galaxies explain this as being due to the brevity of the star-formation epoch in the galaxy, which lasts less than 1 Gyr. Calibration of the displacement of the nucleus of NGC 80 in Fig. 2 relative to the model sequences [Mg/Fe] = 0 based on the computations of Tantalo *et al.* [21] yields [Mg/Fe] $\approx +0.3$. The Mg/Fe ratio decreases with galactocentric distance and is close to the solar value in the bulge, at $R \geqslant 3''$.

Figure 2b is a diagnostic diagram for determining the ages of stellar populations: we compare our data for NGC 80 with the models of Tantalo *et al.* [21] in the (Hβ, $\langle$Fe$\rangle$) plane. Although Tantalo *et al.* [21] did not model the Mgb index, their models are computed for three different [Mg/Fe] ratios, whereas Worthey [20] modeled about 20 different indices for only the solar abundance ratio. We used the models of Tantalo *et al.* [21] for [Mg/Fe] = 0 and [Mg/Fe] = $+0.3$ for the bulge and nucleus, respectively. It is immediately apparent from Fig. 2b that, if we ignored the difference between the Mg/Fe ratios in the nucleus and bulge, the systematic error in the age estimates would amount to 2–3 Gyr for both populations. At the same time, if correctly computed, the mean age for stars in the nucleus is 7 Gyr; the mean stellar age increases abruptly in the immediate vicinity of the nucleus and then drops again to 7 Gyr at a galactocentric radius of $5''$–$7''$. We cannot reliably determine the age of the stellar population in the "old" region at $R \approx 2''$, since these measurements are too contaminated by the nucleus at our seeing. However, this population is obviously older than 10 Gyr. Thus, in a lenticular galaxy that is absolutely devoid of gas and star formation, we have found a stellar nucleus and a ring with a radius of about $6''$, both with a mean age of 7 Gyr. This is significantly lower than the mean age of the bulges of lenticular galaxies, which exceeds 10 Gyr [27]. Since the nucleus of NGC 80 is chemically distinct, these results obviously suggest that we have found traces of a secondary burst of star formation that had a fairly complex geometry.

4. RESULTS OF OUR PHOTOMETRIC ANALYSIS OF NGC 80

We already mentioned in Section 2 that the data from the Observatoire de Haute-Provence have lower spatial resolution than our observations of August 17, 2001, but are deeper in terms of their limiting magnitude. We accordingly used the OHP BVR images to investigate the large-scale structure of the galaxy and our own $BVRI$ images of August 17 to analyze the circumnuclear region.

Figure 3a shows the results of an isophotal analysis of the OHP data: radial variations of the position angle of the isophotal major axis and ellipticity. The ellipticity is small throughout the region studied, as is expected from the round appearance of NGC 80; however, it is not equal to zero. The LEDA database (Table 1) also gives $i = 28°$ and not 0°; i.e., the galaxy is not viewed exactly face-on. Therefore, the asymptotic value $(1 - b/a)_0 = 0.09$ obviously characterizes the inclination of the galactic disk to the line of sight—the galaxy is viewed at an angle of 25°. However, it is then surprising that the ellipticity reaches the asymptotic level at a galactocentric radius as small as $\sim 10''$; this may imply that the photometric structure of the giant lenticular galaxy NGC 80 is already dominated by the disk at $R \approx 10''$, since the axisymmetric bulge, being "plump" in the direction of the vertical coordinate, always yields a lower projected ellipticity than the disk. At radii of $30''$–$45''$, the ellipticity begins to exhibit some irregularity in its behavior; however, the radial variations settle down in the vicinity of $1 - b/a \approx 0.1$ farther from the center. The position angle of the isophotal major axis also behaves fairly monotonically and does not deviate from $\mathrm{PA}_0 \approx 180°$ by more than 5° virtually throughout the radius interval studied. On the whole,

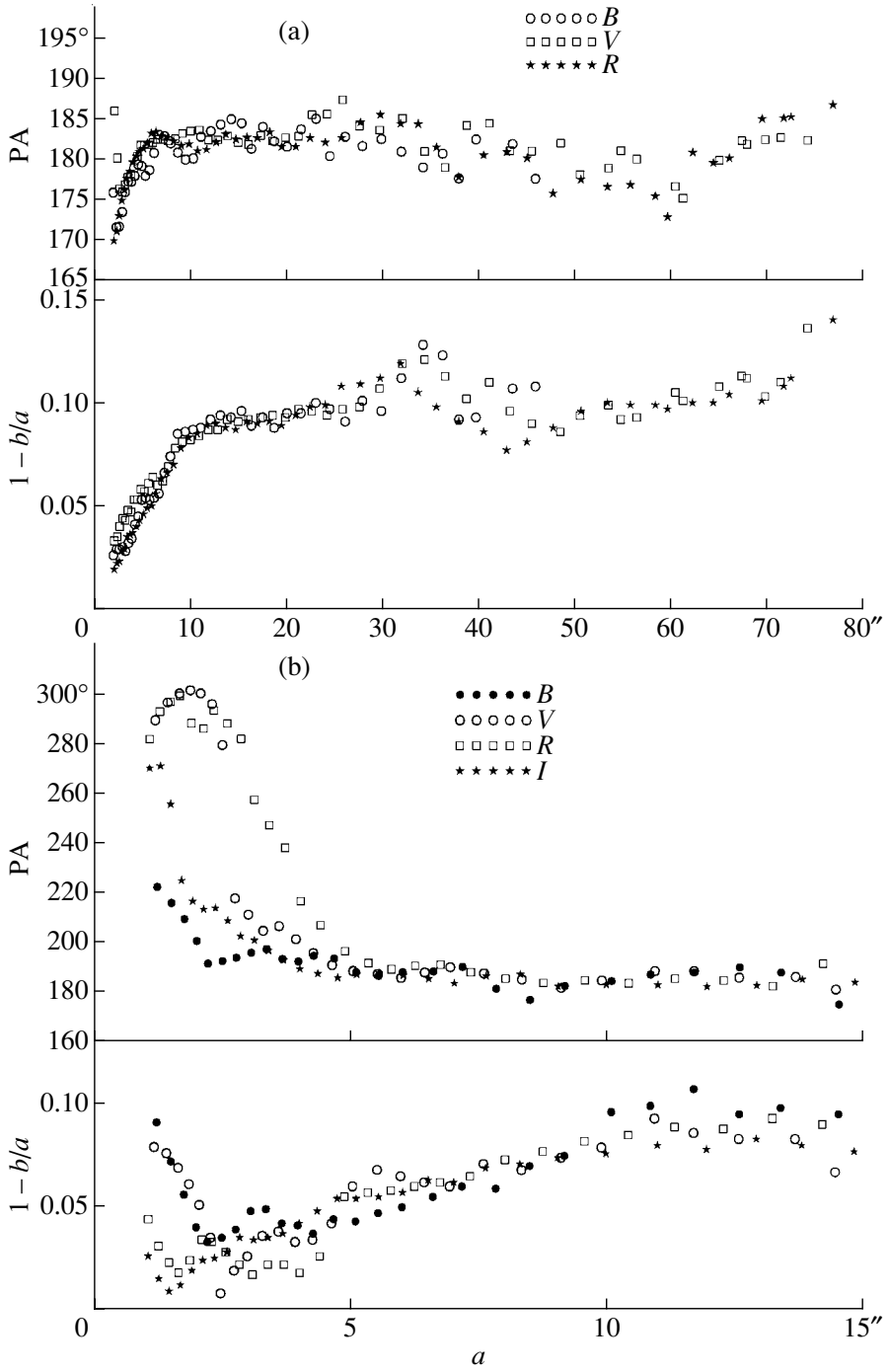

Fig. 3. Radial variations of the isophotal parameters (the position angle of the line of nodes and isophotal ellipticity) in NGC 80 in various photometric bands for (a) data obtained at the 1.2-m OHP telescope and (b) our own observations of August 17, 2001 with the 1-m SAO telescope. The spatial resolutions are 3″ and better than 2″ in (a) and (b), respectively.

the dependences shown in Fig. 3a are typical of a galaxy dominated exclusively by a flat, round stellar disk with no warps or bar.

Figure 3b is similar to Fig. 3a but is based on our data of August 17, 2001, and shows only the very central part of NGC 80. Recall that our B image has a spatial resolution of 2.2″, whereas the resolutions in the remaining three filters are better than 2″. This seemingly small improvement in the spatial resolution had a very dramatic effect on the results of the isophotal analysis: the isophotal major axis rotated by about 90° at the center, and, after reaching a minimum of 0.03 at $R = 2.5''$, the ellipticity again increases toward the nucleus, reaching 0.08–0.09 in the blue

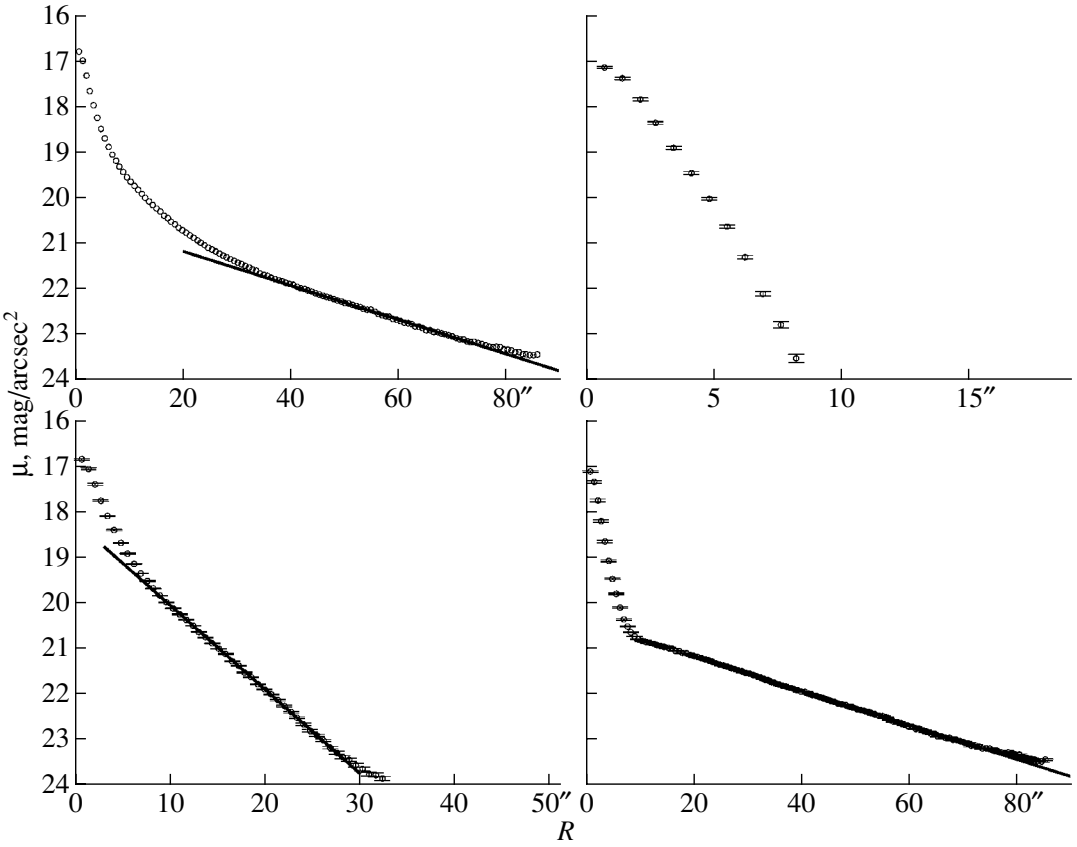

Fig. 4. Example of a decomposition of the azimuthally averaged R surface-brightness profile. Top left: the initial profile (OHP data) with its outermost part fitted by an exponential law; bottom left: the residual brightness profile after subtracting the outer disk, with its outermost part fitted by an exponential law; bottom right: the residual brightness profile after subtracting the inner disk from the initial image (the outer disk obeys a single exponential law throughout the radius interval $8''$–$80''$); top right: the residual brightness profile after subtracting two exponential disks from the initial image.

filters (B, V). All these peculiarities in the behavior of the isophotes are concentrated near the center at $R \leq 3''$, which is close to the limit of our spatial resolution and so may not represent entirely trustworthy measurements. However, our results are supported by those of other studies. The measurements of a V photographic image of NGC 80 by Magrelli *et al.* [28] also showed the isophotes at the center of the galaxy to rotate by 90° and the ellipticity of the isophotes to reach 0.15 near the nucleus. Thus, the chemically distinct nucleus of NGC 80 also stands out as a separate structural subsystem of the galaxy.

Let us now analyze the radial surface-brightness profile (Fig. 4 shows the R profile as an example). In contrast to the dependences shown in Fig. 3a, the brightness profile changes its behavior near $R \approx 35''$–$40''$: the galaxy appears to consist of several global structural components. Let us first assume, in line with tradition, that the outer and inner components are an exponential disk and de Vaucouleurs bulge, respectively. The B brightness profile in the radius interval $R \approx 10''$–$46''$ can indeed be fitted within the observational errors by a $R^{1/4}$ law; this implies that the global exponential disk does not have an inner part $R < 40''$; however, global disks with central "holes" are quite common in early-type disk galaxies [29, 30]. However, this approach leads to rather unusual bulge parameters: $r_e = 36''$, or 13.6 kpc and $B_{e,0} = 24.14$, which deviates by more than 1^m (toward lower brightnesses) from the well-known statistical dependence of Kormendy [31], $B_{e,0} = 19.74 + 3.02 \log r_e$. The implied exponential scale length of the outer disk is 11 kpc, which is unusually large, and is smaller than the effective bulge radius, although, statistically, it should be the other way round [32]. The situation is clarified if we approach the problem from a different angle and abandon the hypothesis of a central "hole" in the outer disk. In this case, the residual brightness profile after subtracting the modeled outer exponential disk from the observed image of NGC 80 can likewise be fitted by an exponential law in the radius interval $R \approx 8''$–$28''$ (Fig. 4) but, naturally, with a shorter scale length (of about 2 kpc) and higher central

Table 3. Parameters of exponential fits to the photometric components of NGC 80

Component (disk)	μ_0, mag/arcsec^2 (2D)	r_0''	μ_0, mag/arcsec^2	r_0''	r_0, kpc
			B		
Outer (40″–75″)	21.7	27.3	21.82 ± 0.01	28.7 ± 0.2	10.8
Inner (10″–24″)	19.5	5.6	19.66 ± 0.02	5.91 ± 0.04	2.2
			V		
Outer (40″–77″)	20.8	28.3	20.90 ± 0.01	29.4 ± 0.1	11.1
Inner (8″–27″)	18.5	5.7	18.63 ± 0.01	6.01 ± 0.02	2.3
			R		
Outer (40″–77″)	20.1	27.3	20.28 ± 0.01	28.8 ± 0.1	10.9
Inner (8″–27″)	17.9	5.5	18.04 ± 0.01	5.84 ± 0.01	2.2

brightness. The exponential law in the inner component can be followed over three scale lengths, giving the fit very high confidence. After subtracting the modeled inner disk from the observed galaxy image, it becomes immediately apparent that the outer disk exhibits a rarely seen exponential behavior over the radius interval $R \approx 10''$–$80''$ (Fig. 4). This "residual" image enables us to refine the parameters of the outer disk, which we have done.

Table 3 lists the parameters for our approximations of the NGC 80 images using two exponential laws in all three BVR filters and the OHP data. We present our results for two methods: iterative decomposition of the azimuthally averaged brightness profiles and fitting the two-dimensional images by a sum of two exponential disks. The results obtained using the two methods are in good agreement. The central surface densities have been corrected for Galactic absorption in accordance with the recommendations given in the NED database.

It is now clear that the main structural components of NGC 80 are two exponential stellar disks with different scale lengths. The outer disk has fairly ordinary characteristics, although its scale length is among the longest known. Its central brightness is absolutely typical of such objects and lies at the center of the well-known distribution of Freeman [33]. The inner disk has an unusually high central brightness but is a flat disk and not a so-called exponential bulge, since, as we pointed out above, the isophotal ellipticity already reaches its asymptotic level at $R \approx 10''$. After subtracting two asymptotic disks from the images of NGC 80, we obtain a compact, circumnuclear component with a radius of about $R \approx 7''$–$8''$ and a weakly convex brightness profile (Fig. 4). However, the poor seeing of the OHP images makes it impossible to analyze the profile of this compact component, so its nature remains unclear.

Finally, Fig. 5 shows azimuthally averaged radial color profiles for NGC 80 based on our August 2001 data, for which the calibration in the standard Johnson–Cousins system is most reliable. Out to $R = 10''$–$20''$, we use the data for August 17, which have the best spatial resolution, and farther from the center, we use coadded data for August 16 and 17. All the color profiles exhibit a well-defined "blue" ring at $R = 7''$–$8''$ and, although our spectroscopic data end at $R = 6.3''$, the blue ring in Fig. 5 can nevertheless be identified with the region with a relatively young stellar population in Fig. 2. This region apparently ends completely by $R \approx 12''$. The color difference between the nucleus and the ring can be interpreted as reflecting the difference in the mean metallicities of the corresponding stellar populations. In this case, $\Delta(B-V) = 0.12$ corresponds to $\Delta[\mathrm{m/H}] = +0.4$; i.e., the nucleus is richer in metals (here, we have adopted the color calibration in terms of properties of stellar populations of [34]). Recall that the magnesium line yielded $\Delta[\mathrm{m/H}] = +0.3$. The color difference between the ring and more outer regions at $R > 12''$ must be due to a superposition of the effects of age and metallicity differences, which cannot be disentangled without spectroscopic data. The color variations in NGC 80 are fairly small outside the circumnuclear region. More precisely, we can say with confidence that the color does not change at all with radius within the inner disk, while there may be a color difference between the inner and outer disks (see the $B-I$ and $V-I$ profiles in Fig. 5), with the outer disk being slightly bluer than the inner disk.

5. RESULTS AND DISCUSSION

We find the giant lenticular galaxy NGC 80, which is the brightest member of a rich group (or a poor cluster), to possess a chemically distinct nucleus: the

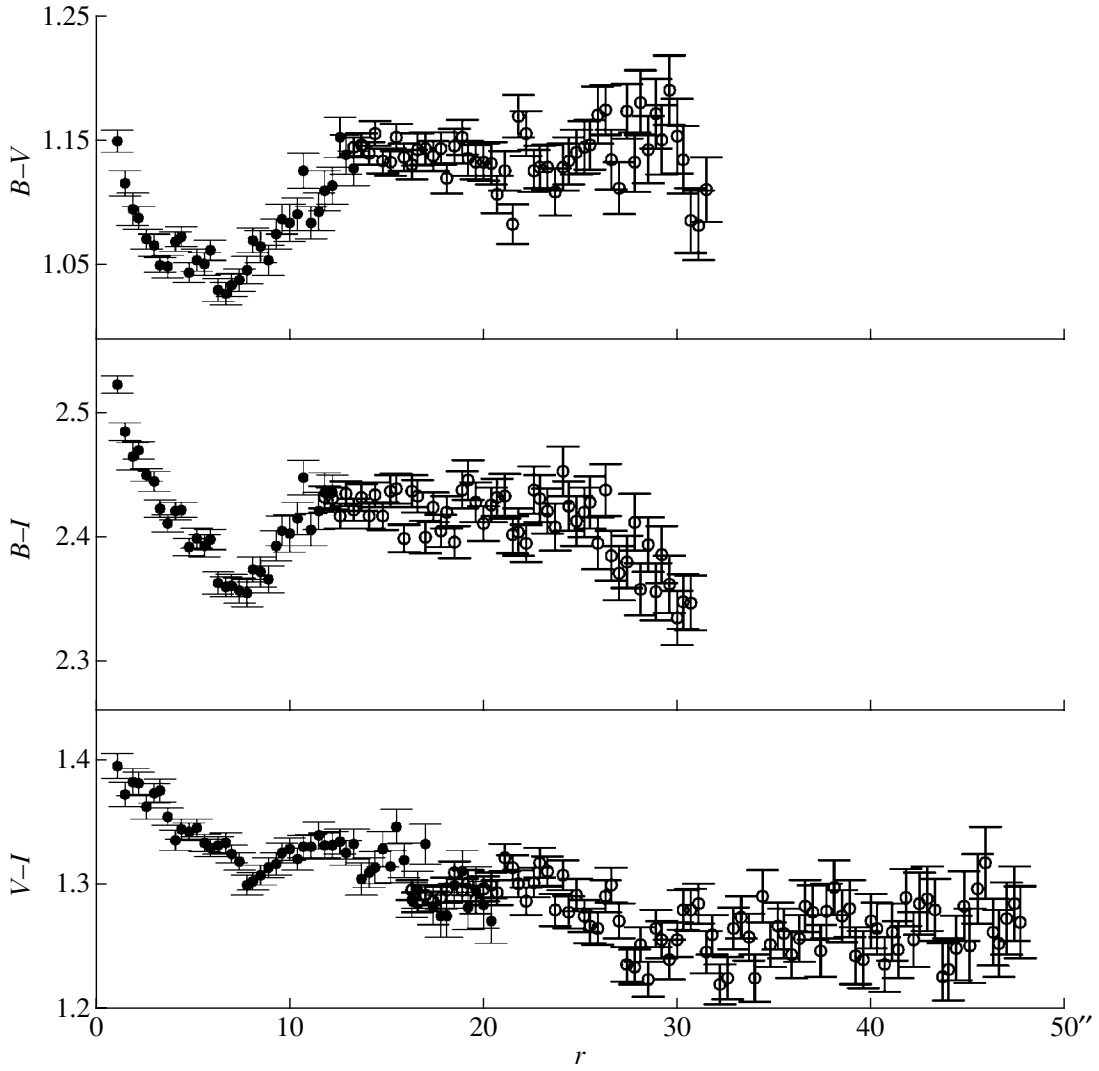

Fig. 5. Azimuthally averaged color profiles for NGC 80 derived from the 1-m SAO data. The filled and open circles show the high-resolution data of August 17, 2001, and the coadded data of August 16 + 17, 2001, respectively.

mean metallicities of the nucleus and circumnuclear region ($R = 2''$–$7''$) differ by about +0.3 to +0.4 dex, or a factor of 2–2.5. The age structure of the central region of NGC 80 is also complex: the mean age of the populations in the nucleus and in the ring of radius $R = 5''$–$8''$ is 5–7 Gyr, whereas the stars located between the nucleus and this ring are much older. It appears that there was a secondary burst of star formation that produced the chemically distinct nucleus, which had the geometrical form of a ring of radius 2–3 kpc and an additional source of star formation at the center of this ring. The fact that the elemental abundance ratio in the nucleus is $[\mathrm{Mg/Fe}] \approx +0.3$ but is $[\mathrm{Mg/Fe}] \approx 0$ in the ring leads us to conclude that the burst of star formation was shorter (albeit more efficient) in the nucleus than in the ring. Given the equal mean ages of the stellar populations, this implies that the onset of the burst of star formation in the ring preceded that in the nucleus. At the same time, triggering a ring-shaped circumnuclear burst of star formation requires a bar (triaxial potential), which is currently absent from NGC 80.

The global structure of NGC 80 is also unusual. The disk in this galaxy has a sort of two-tiered structure consisting of an outer exponential disk with a long scale length and normal central surface brightness and an inner, compact, bright disk that is also exponential. Since the galaxy is viewed almost face-on, we can firmly conclude that the two disks are round, flat, and coplanar. We have already encountered two-tiered disks in galaxies with chemically distinct nuclei and suggested that these two phenomena may be related. If at some time an outer tidal action or internal bar instability perturbed the global gaseous

disk of a spiral galaxy, the infall of gas from the outer regions of the galaxy into its inner regions should have triggered both a central burst of star formation and an abrupt change in the characteristic radial scale length for the distribution of newly born stars. However, in both NGC 615 [35] and NGC 7217 [36], to which this hypothesis was to be applied, the inner compact disks have oval shapes, which is clear evidence of the past existence of a global bar, which could have triggered the large-scale redistribution of gas in the disk.

In two other galaxies (the lenticulars NGC 4429 and NGC 7013), we [37] found relatively young circumnuclear rings, similar to the ring in NGC 80 but with smaller radii of about 0.5 kpc. However, the global brightness profiles of these galaxies contain an additional component—a "lens," which is also oval and, again, is believed to have been produced by the disruption of a bar. In NGC 80, we have found for the first time a ring structure for a central burst of star formation and a multi-tiered structure for the stellar disk combined with clear axial symmetry of all the galactic components. Is it possible in a very dense environment with a high probability for multiple impacts of satellites into the galaxy to obtain a pure $m = 0$ mode for the perturbation of the global gaseous disk? Or did the galaxy actually have a bar, which has dissipated without leaving a trace? Only specialized three-dimensional models can provide answers to these questions. Resolving these problems may also shed light on the origin of lenticular galaxies: it is possible that NGC 80 was previously a giant late-type spiral galaxy that lost its gas as a result of catastrophic events whose consequences we have just discovered. In any case, NGC 80 lacks any significant spheroidal component (bulge), which is believed to be a mandatory attribute of a classical lenticular galaxy.

6. ACKNOWLEDGMENTS

We are grateful to V.L. Afanasiev, A.N. Burenkov, and S.N. Dodonov of the Special Astrophysical Observatory for their support with the observations at the 6-m telescope and to V.P. Mikhailov for his support with the observations at the 1-m telescope. Some of the observational data used in this work were obtained on the 6-m telescope funded by the Ministry of Industry and Science of the Russian Federation (registration number 01- 43). We also used photometric data obtained by Philippe Prugnel with the 1.2-m telescope of the Observatoire de Haute-Provence. We acquired these data from the HYPERCAT archive of extragalactic data. We also made use of the Lyon–Meudon extragalactic database (LEDA), provided by the LEDA team at the CRAL observatory (France), and the NASA/IPAC NED extragalactic database, operated by the Jet Propulsion Laboratory of the California Institute of Technology under a contract with the National Aeronautics and Space Administration (USA). This work was supported by the Russian Foundation for Basic Research (project no. 01-02-16767) and the Federal Research and Technology Program "Astronomy. Fundamental Space Research" (section "Astronomy") 1.2.4.1.

REFERENCES

1. D. Maoz, A. V. Filippenko, L. C. Ho, *et al.*, Astrophys. J., Suppl. Ser. **107**, 215 (1996).
2. P. T. de Zeeuw, M. Bureau, E. Emsellem, *et al.*, Mon. Not. R. Astron. Soc. **329**, 513 (2002).
3. R. Buta, Publ. Astron. Soc. Pac. **105**, 654 (1993).
4. R. Buta and D. A. Crocker, Astron. J. **105**, 1344 (1993).
5. R. Buta, W. van Driel, J. Braine, *et al.*, Astrophys. J. **450**, 593 (1995).
6. R. Buta, Astrophys. J. **370**, 130 (1991).
7. L. Athanassoula, *Barred Galaxies,* Ed. by R. Buta, D. A. Crocker, and B. G. Elmegreen, Astron. Soc. Pac. Conf. Ser. **91**, 309 (1996).
8. O. K. Sil'chenko, Astron. Astrophys. Trans. **20**, 123 (2001).
9. O. K. Sil'chenko, Astron. J. **117**, 2725 (1999).
10. O. K. Sil'chenko, Astron. J. **118**, 186 (1999).
11. V. V. Vlasyuk and O. K. Sil'chenko, Astron. Astrophys. **354**, 28 (2000).
12. T. Wiklind, F. Combes, C. Henkel, and F. Wyrowski, Astron. Astrophys. **323**, 727 (1997).
13. O. K. Sil'chenko, Astron. Zh. **71**, 706 (1994) [Astron. Rep. **38**, 624 (1994)].
14. R. Buta and K. L. Williams, Astron. J. **109**, 543 (1995).
15. P. Chamaraux, C. Balkowski, and P. Fontanelli, Astron. Astrophys. **165**, 15 (1986).
16. P. Prugniel and F. Simien, Astron. Astrophys. **282**, L1 (1994).
17. V. L. Afanas'ev, V. V. Vlasyuk, S. N. Dodonov, and O. K. Sil'chenko, Preprint No. 54, SAO AN SSSR (1990).
18. V. V. Vlasyuk, Astrofiz. Issled. (Izv. SAO RAN) **36**, 107 (1993).
19. G. Worthey, S. M. Faber, J. J. González, and D. Burstein, Astrophys. J., Suppl. Ser. **94**, 687 (1994).
20. G. Worthey, Astrophys. J., Suppl. Ser. **95**, 107 (1994).
21. R. Tantalo, C. Chiosi, and A. Bressan, Astron. Astrophys. **333**, 419 (1998).
22. P. Poulain, Astron. Astrophys., Suppl. Ser. **72**, 215 (1988).
23. A. U. Landolt, Astron. J. **104**, 340 (1992).
24. S. C. Trager, G. Worthey, S. M. Faber, *et al.*, Astrophys. J., Suppl. Ser. **116**, 1 (1998).
25. O. K. Sil'chenko, Pis'ma Astron. Zh. **19**, 693 (1993) [Astron. Lett. **19**, 279 (1993)].
26. G. Worthey, S. M. Faber, and J. J. González, Astrophys. J. **398**, 69 (1992).

27. O. K. Sil'chenko, in *Galaxies: The Third Dimension,* Ed. by M. Rosado, L. Binette, and L. Arias (2002) (in press).
28. G. Magrelli, D. Bettoni, and G. Galetta, Mon. Not. R. Astron. Soc. **256**, 500 (1992).
29. J. Kormendy, Astrophys. J. **217**, 406 (1977).
30. W. E. Baggett, S. M. Baggett, and K. S. J. Anderson, Astron. J. **116**, 1626 (1998).
31. J. Kormendy, Astrophys. J. **218**, 333 (1977).
32. R. S. de Jong, Astron. Astrophys. **313**, 45 (1996).
33. K. C. Freeman, Astrophys. J. **160**, 811 (1970).
34. A. Vazdekis, E. Casuso, R. F. Peletier, and J. E. Beckman, Astrophys. J., Suppl. Ser. **106**, 307 (1996).
35. O. K. Sil'chenko, V. V. Vlasyuk, and F. Alvarado, Astron. J. **121**, 2499 (2001).
36. O. K. Sil'chenko and V. L. Afanasiev, Astron. Astrophys. **364**, 479 (2000).
37. O. K. Sil'chenko and V. L. Afanasiev, Astron. Astrophys. **385**, 1 (2002).

Translated by A. Dambis

Astronomy Reports, Vol. 47, No. 2, 2003, pp. 99–109. Translated from Astronomicheskiĭ Zhurnal, Vol. 80, No. 2, 2003, pp. 118–129.

The H_2O Supermaser Region in Orion KL: Epoch 1982.9

V. A. Demichev, K. M. Zakharin, and L. I. Matveenko*

Space Research Institute, Russian Academy of Sciences, Profsoyuznaya ul. 84/32, Moscow, 117810 Russia

Received April 5, 2002; in final form, May 23, 2002

Abstract—Radio interferometric observations of an H_2O maser flare in the Orion Nebula at epoch 1982.9 have been used to determine the flare's spatial structure. Antennas in the Crimea, Effelsberg, and Onsala were used. The emission region consists of three groups of components. The angular sizes of the components are 0.2–0.9 mas, and the widths of the emitted lines are 0.2–0.7 km/s. The velocities of the components are correlated with their relative positions, which correspond to expanding concentric rings. Assuming a 1 $M_\odot$ protostar in a Keplerian approximation, the radius of the inner ring R is 15 AU, the velocity of its rotation $V_{\rm rot}$ is 8.98 km/s, and the radial component of the velocity $V_{\rm rad}$ is 1.79 km/s. For the outer ring, $R = 15.7$ AU, $V_{\rm rot} = 8.79$ km/s, and $V_{\rm rad} = 2.61$ km/s. © *2003 MAIK "Nauka/Interperiodica"*.

1. INTRODUCTION

Active star formation is occurring in gas–dust complexes such as the Orion Nebula. The star-formation processes are accompanied by powerful maser emission in the water vapor line at $\lambda = 1.35$ cm, corresponding to the 6_{16}–5_{23} rotational transition ($f_0 = 22\,235.08$ MHz). This line is a sensitive tracer of physical processes in the regions of formation of stars and planetary systems, and opens considerable opportunities for high-angular-resolution studies using Very Long Baseline Interferometry.

The H_2O maser emission is highly linearly polarized and variable. In some cases, powerful flares are observed. This phenomena was first discovered in 1970 in the object W49 [1], whose brightness temperature exceeded 10^{17} K. The second case of high activity manifest as individual flares of the H_2O maser emission was observed in 1979–1987 in the Orion Nebula. The radial velocity V of the emission region was ≈ 8 km/s, and the degree of linear polarization P reached $\geq 60\%$ [2–4]. This region was located in one of eight active zones [5]. Preliminary analyses suggested it had a highly organized structure in the form of a chain of compact components, tracing an accretion disk at the stage of its separation into protoplanetary rings [6–9]. The computer resources of that time limited our abilities to carry out detailed studies of the object's structure. We now possess the facilities required to study the fine structure of the region of H_2O supermaser emission in Orion KL at various stages of its development [10].

*E-mail: demichev@mx.iki.rssi.ru

2. OBSERVATIONS OF THE H_2O MASER EMISSION FLARE

We observed an H_2O supermaser flare at $\lambda = 1.35$ cm in the Orion Nebula on December 1, 1982, from 20:00 to 23:00 UT using an array of three radio telescopes: the 100-m Effelsberg, 22-m Simeiz, and 20-m Onsala antennas. The flux density F of the flare emission reached 1.8×10^6 Jy. The antenna temperatures $T_{\rm a}$ toward the source exceeded 10^5 K and were much greater than the system noise temperatures, $T_{\rm sys} \approx 100$ K. The received signals were recorded using MK-II equipment with a total bandwidth of 500 kHz. Hydrogen frequency standards were used to synchronize the time and local-oscillator frequencies. The time signals at the radio telescopes were synchronized using navigation signals to an accuracy of $\Delta T \approx 1$ μs [10].

The observations were correlated on the MK-2 correlator of the National Radio Astronomy Observatory in Socorro. This correlator had 96 complex channels, providing a frequency resolution of 5.2 kHz. After spectral processing (applying a Fourier transform) and calibration, the correlated signals were averaged over 5 min.

The small number of antennas used and the resulting incompleteness of the uv coverage necessitated deriving information about the object's structure via model fits to the data. We assumed the brightness distributions and emission profiles of the components to be either Gaussians or δ functions.

3. INTERFEROMETER RESPONSE

The measured amplitudes and phases of the interferometric signal (radio interferometer response)

1063-7729/03/4702-0099$24.00

depend on the source brightness distribution $T_b(x, y)$. The phase of the correlated signal includes the following components:

$$\varphi = 2\pi[\Delta\tau_{hf} f + \Delta\tau_{lf} f_{if1} + (\tau_g - \tau_c) f + \tau_c f_{lo1} + (\tau_{lf2} + \tau_c)\Delta f_{lo} + \Delta f_{lo} t] + \Delta\varphi_{lo}, \quad (1)$$

where τ_{lf} is the delay at the high frequency ($f \cong 22$ GHz) occurring in the atmosphere, ionosphere, and receiver; τ_{lf} includes the delay in the receiver at the intermediate frequency $f_{if} = f - f_{lo}$ and the timing error; τ_g is the geometrical delay; τ_c is the calculated geometrical delay; f_{lo} is the local-oscillator frequency; and φ_{lo} is the phase of the local-oscillator signal.

The measured quantity is the geometrical delay τ_g. The remaining phase components in (1) are determined by the observational errors and are functions of both time $\varphi(t)$ and frequency $\varphi(f)$:

$$d\varphi/dt = 2\pi d[(\tau_g - \tau_c) f + \tau_c f_{lo1} + \tau_c \Delta f_{lo} + \Delta f_{lo}]/dt + d\Delta\varphi_{lo}/dt,$$

$$d\varphi/df = 2\pi[\Delta\tau_{hf} + \Delta\tau_{lf} + \tau_g - \tau_c].$$

The effect of the errors can be considerably reduced by calibrating using a reference continuum source and one of the components of the target object itself. Maser sources can have fairly complex spatial structures, and the reference feature adopted is usually the brightest compact component.

The phase difference after calibration is

$$\Delta\varphi = 2\pi[(\Delta\tau_{hf} + \Delta\tau_{lf} - \tau_c + \tau_g)\Delta f + \Delta\tau_g f_g]. \quad (2)$$

Obviously, in this case, the terms due to the main phase errors, which are associated with instability of the local oscillators, are eliminated

$$(\tau_c f_{lo1} + (\tau_{lf2} + \tau_c)\Delta f_{lo} + \Delta f_{lo} t).$$

However, there remains the phase component due to the delay $(\Delta\tau_{hf} + \Delta\tau_{lf} - \tau_c + \tau_{lo})$, which depends on the frequency Δf. This delay $\tau = \dfrac{1}{2\pi}\dfrac{d\Delta\varphi}{d\Delta f}$ can be eliminated via calibration using data for a continuum source.

Table 1. Correction factors for the baselines

Polarization	K
Simeiz–Onsala (LCP–LCP)	1
Simeiz–Onsala (RCP–LCP)	1.7
Effelsberg–Onsala (L–LCP)	0.57
Effelsberg–Simeiz (L–RCP/LCP)	0.57

In the case of observations using three or more antennas, the closure phases can be for calibration [11]. This approach is based on the fact that the sum of the errors for the phases on three baselines of a closed triangle are $\sum\tilde{\varphi} = 0$. Thus, the sum of the phases is determined solely by the geometrical delays:

$$\varphi_{12} + \varphi_{23} + \varphi_{31} = \varphi_{g123}.$$

This enables us to make a mutual connection of the phases of the spatial harmonics in the image studied.

We calibrated the data phases using a reference signal injected into channel 64. Calibration using a continuum source showed that the residual phase progression is $-95°$ per channel ($\Delta f_{ch} = 5.2$ kHz) for the Effelsberg–Simeiz (ES) baseline, corresponding to a delay of $\tau = -51$ μs. For the Simeiz–Onsala (SO) baseline, the phase progression is 133° per channel, or $\tau = 71$ μs, and the phase progression for the Effelsberg–Onsala (EO) baseline is 43° per channel, or $\tau = -23$ μs. The sum of the phase progressions is $-5°$ per channel; according to the phase closure method, this suggests a probable calibration inaccuracy. Figures 1a–1c show the signal profiles of the target after calibration (time $t = 20^h17^m$ UT). The amplitude of the correlated data was corrected for atmospheric absorption, the antenna gains, and pointing variations using the autocorrelation spectra of the signals. The source signal considerably exceeded the intrinsic system noise ($F_{peak} = 1.8 \times 10^6$ Jy), which simplified the amplitude calibration.

4. POLARIZATION

The supermaser emission flare had a high degree of linear polarization, $P \approx 57\%$, with a position angle of $\chi_p \approx -27°$ [3, 4]. To enable measurement of the polarization parameters, the radio telescopes recorded the following polarizations: linear vertical (L) in Effelsberg, left-circular (LCP) in Onsala, and alternating left/right-circular (LCP/RCP, toggled every 30 min) in Simeiz.

The emitted signal of the target, T, includes $T_n + T_{lin}$, where T_n is the unpolarized component and T_{lin} is the linearly polarized component. The degree of polarization P is T_{lin}/T and was $P = 0.568$ at the epoch of the observations on December 24, 1982 [3]. The antennas have altitude–azimuth mounts, and the received signal of the polarized component depends on the parallactic angle χ. The Effelsberg telescope received the vertical component of linear polarization. During the observations, the angle χ varied from $-14°$ to 9°. Accordingly, the level of the received polarized component changed from 0.9 to 1.

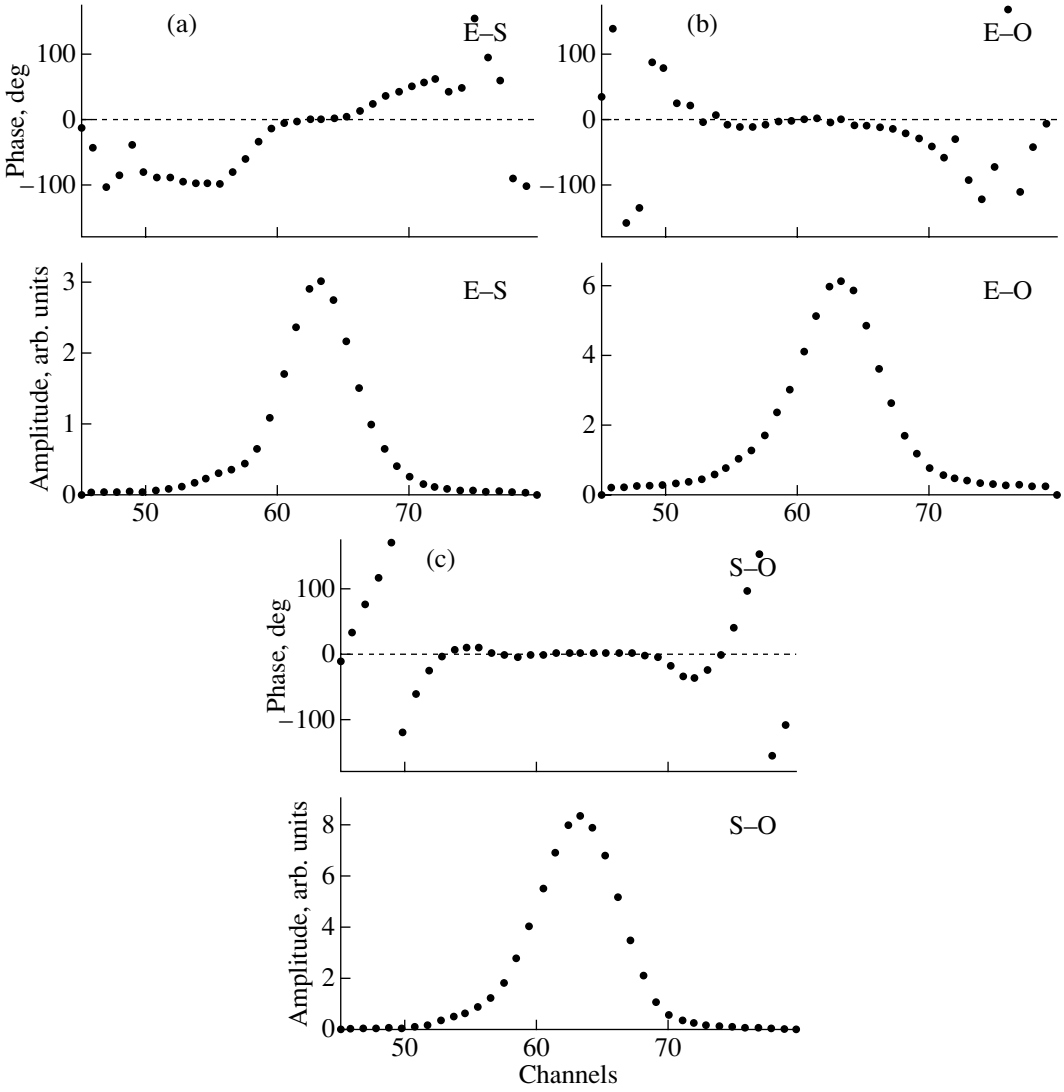

Fig. 1. Correlated fluxes and phases versus channel number ($t = 20^{\rm h}17^{\rm m}$) recorded on the (a) Effelsberg–Simeiz, (b) Effelsberg–Onsala, and (c) Simeiz–Onsala baselines.

The correlated output signals at the interferometer backend with regard to the polarization received are

$$\text{Effelsberg–Onsala}$$
$$(T_{aL} \times T_{aLCP})^{0.5} \sim (0.5)^{0.5} T_n + 2T_{\rm lin} \cos \Delta\chi,$$
$$\text{Effelsberg–Simeiz}$$
$$(T_{aL} \times T_{aLCP})^{0.5} \sim (0.5)^{0.5} T_n + 2T_{\rm lin} \cos \Delta\chi, \quad (3)$$
$$\text{Simeiz–Onsala}$$
$$(T_{aLCP} \times T_{aLCP})^{0.5} \sim T_n + T_{\rm lin}$$
$$\text{or } (T_{aLCP} \times T_{aRCP})^{0.5} \sim T_{\rm lin}.$$

These relationships indicate that the baselines' responses are different. The corresponding correction factors K are given in Table 1. A single response is $T_n + T_{\rm lin}$.

We can see from the above relationships (3) that the Simeiz–Onsala baseline response is proportional to the total signal when identical polarizations are received or to its polarized component when orthogonal polarizations are received. Figure 2 explains this case. We can see that the correlated flux decreases with increasing angular resolution from 3.5 units ($\varphi_{\rm l} = 3.6$ mas) to 0.3 units ($\varphi_{\rm л} = 1.7$ mas). However, the degree of polarization degree remains virtually the same: $P = 58\%$. This suggests that the degree of polarization does not depend on the component sizes: the polarization level within the considered structures is constant.

5. RELATIVE POSITIONS OF THE COMPONENTS

The coordinates of a compact source can be determined from the interference fringe rate and its

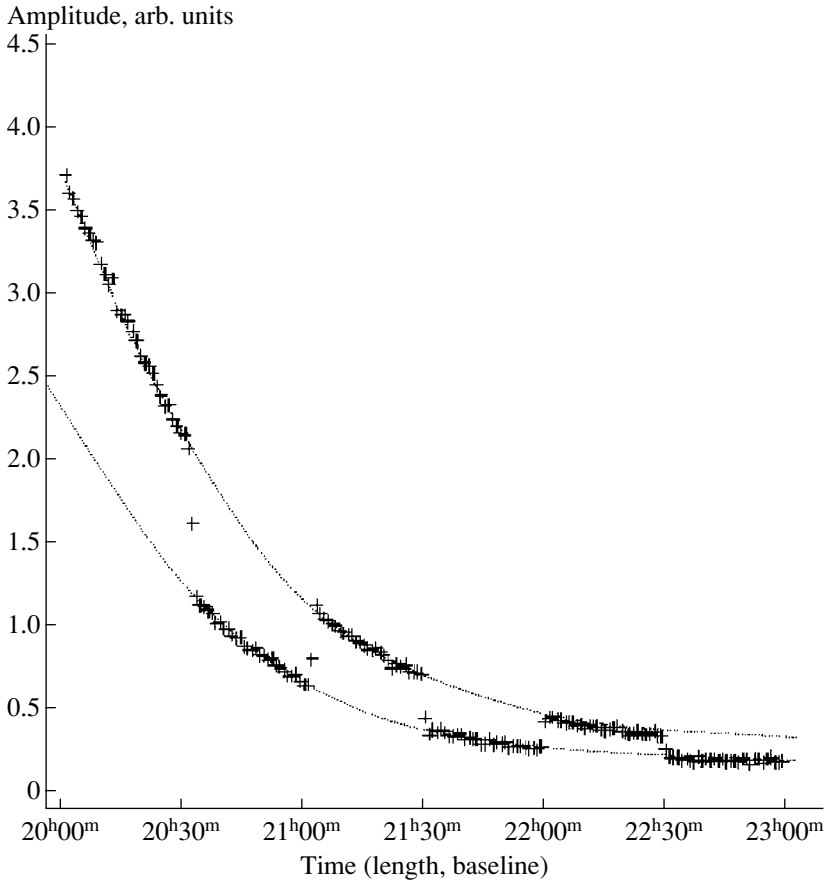

Fig. 2. Correlated flux versus Simeiz–Onsala baseline (i.e., time). The jumps are caused by the polarization toggling in Simeiz.

phase [11]. The measurement accuracy depends on the signal-to-noise ratio. In the case of measurements using the fringe rate, the error is

$$\Delta\beta \cong \frac{\sigma_{\rm fr}}{\omega_e B_\lambda \cos\delta_b},$$

where $\sigma_{\rm fr} = \sqrt{\frac{3}{2\pi^2}}\left(\frac{T_s}{T_s - T_{\rm noise}}\right)\frac{1}{\sqrt{\Delta f t^3}}$ is the error in the fringe rate, ω_e is the angular speed of the Earth's rotation, $\delta_{\rm b}$ is the baseline declination, T_s and $T_{\rm noise}$ are the on-source and off-source system noise temperatures, and t is the time of the measurement.

The on-source antenna temperature increase is $T_{\rm a} = \frac{FA_{\rm eff}}{2k}$. The effective areas of the Simeiz, Effelsberg, and Onsala antennas $A_{\rm eff}$ were 180–800 m^2. The source flux density F was 1.8×10^6 Jy, so that $T_{\rm a} = (1\text{–}5) \times 10^5$ K. The system noise temperatures did not exceed 100–150 K; i.e., the ratio $T_s/(T_s + T_{\rm noise}) \approx 1$. Thus, the errors in the positions measured using the fringe rates for various baselines are $\Delta\beta =$ (0.07–0.2) mas.

The accuracy of positions determined using the interference fringe phases are [11]:

$$\Delta\beta \cong \frac{\sigma_{\rm ph}}{B_\lambda},$$

where $\sigma_{\rm ph} = \frac{T_{\rm s}}{T_{\rm a}\sqrt{2\Delta f t}}$. In our case, $\Delta\beta = (0.14\text{–}0.5)$ μs, appreciably better than for the fringe-rate positions.

6. STRUCTURE OF THE FLARE REGION

An object is mapped using the baseline responses—the correlated fluxes and their phases. The baselines in our array have high angular resolution, which considerably limits their response to extended structures in the source. The large-scale structure of the emission region was estimated in our Gaussian approximations directly from the variations in the correlated fluxes as a function of the baseline lengths. Figure 2 presents the correlated source flux in channel 64 ($V = 7.56$ km/s) as a function of length of the Simeiz–Onsala baseline. The analogous data for all three baselines suggest a structure formed by two

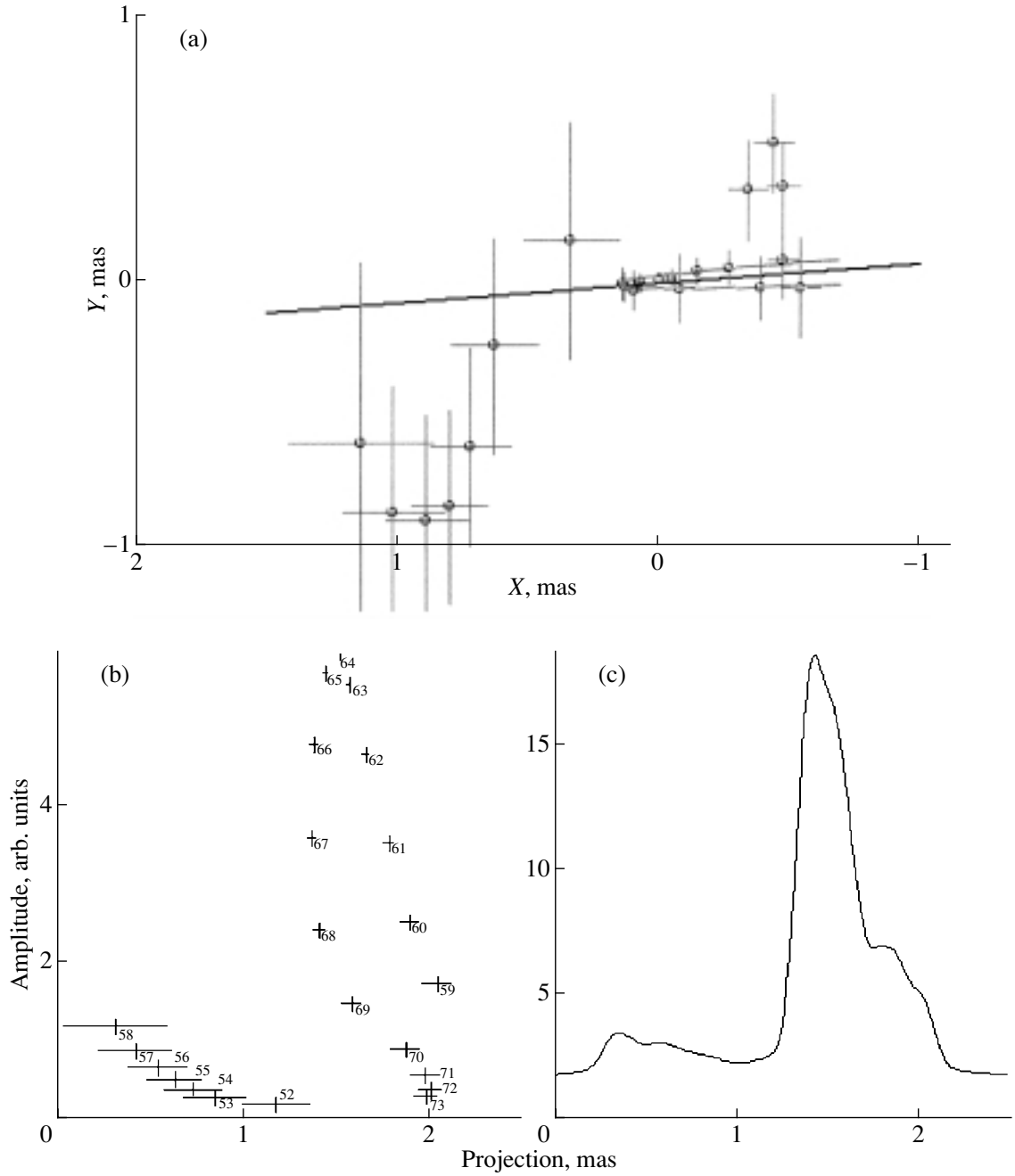

Fig. 3. (a) Distribution of the components in the X–Y plane, (b) projection of the components along the direction $Q = 86°$, (c) brightness distribution smoothed with a 0.2-mas Gaussian beam.

Gaussian components with half-power sizes of 1.9×1.13 and $\approx 0.9 \times 0.3$ mas. The components are elongated in the direction $Q \approx 90°$, and the average transverse size of the extended component does not exceed 1 mas. The flux densities of the components are $F = 1.57 \times 10^6$ and 0.25×10^6 Jy, and their brightness temperatures are $T_\mathrm{b} = 2.0 \times 10^{15}$ and 2.6×10^{15} K.

Our estimate of the fine structure of the studied region was then refined using the complex correlated fluxes as functions of time in each individual channel. As a first approximation, we assumed that the emission of only one compact source dominates in each channel. We represent the overall brightness distribution as a set of compact components (δ-functions).

The interferometer response to a source with brightness distribution $T_\mathrm{b}(\beta, f)$ is

$$\mathbf{R}(\theta, \beta, f) = \int_{-\infty}^{+\infty} T_\mathrm{b}(\beta, f) \exp(j2\pi B_\lambda \beta) d\beta,$$

Table 2. Distribution of the components

No.	Channels		LSR velocity, km/s		X, mas		Y, mas		Relative separation, mas		Group amplitude, arb. units
	from	to	from	to	from	to	from	to	from	to	
1	59	69	7.21	7.91	−0.54	0.14	−0.04	0.04	0	0.54	3.6
2	52	58	7.98	8.4	0.34	1.14	−0.91	0.15	0.37	1.34	0.58
3	70	73	6.93	7.14	−0.47	−0.34	0.07	0.51	0.48	0.67	0.53

where $\beta = (xu_j + yv_j)/B_\lambda$ is the component's position along the baseline direction, x and y are relative coordinates on the celestial sphere, $B_\lambda = |u_j, v_j|$ is the projected baseline in wavelengths.

In this case, the phase difference $\phi = \Delta\varphi$ of the signal of the ith component for the jth baseline projection can be represented as the scalar product

$$\phi_{ij} = 2\pi(x_i u_j + y_i v_j + N_{ij}), \qquad (4)$$

where the N_{ij} are integers.

This equation contains a $2\pi N_{ij}$ ambiguity, corresponding to a certain number of interference lobes. In the case considered, the interference lobe width θ_l is 1.7–4 mas. The uncertainty for each value of i and j can be eliminated using the fringe-rate measurements of the components' positions [9, 10].

The time variation of the correlated signal phase (fringe rate) is $\Delta F_\mathrm{fr} = \dfrac{1}{2\pi}\dot{\phi}(t)$ and depends on the baseline derivatives:

$$\Delta F_\mathrm{fr} = (x_i \dot{u}_\mathrm{j} + y_i \dot{v}_j).$$

In our case, the time discretization is determined by the averaging time, which was equal to 300 s. For various values of i and j, we can obtain a set of equations and find the relative positions of the components via a least-squares fit. The optimal solutions are achieved for the values of x, y corresponding to the set of two equations

$$\sum_j \dot{u}_j \Delta F_{fr\,ij} = \sum_j (\dot{u}_j^2 x_i + \dot{u}_j \dot{v}_j y_i),$$

$$\sum_j \dot{v}_j \Delta F_{fr\,ij} = \sum_j (\dot{u}_j \dot{v}_j x_i + \dot{v}_j^2 y_i).$$

The accuracy of the relative positions lies within an interference lobe and reaches 0.07–0.2 mas, allowing us to eliminate the $2\pi N_{ij}$ ambiguity, so that (4) is transformed into

$$\phi_{ij} = 2\pi(x_i u_j + y_i v_j + N_{ij}).$$

The solutions (x, y) are found via a least-squares fit using the equations

$$\sum_j \phi_{ij} u_j = 2\pi \sum_j (x u_j^2 + y u_j v_j),$$

$$\sum_j \phi_{ij} v_j = 2\pi \sum_j (y v_j^2 + x u_j v_j).$$

The errors, which are determined by the sensitivity, are ∼0.14–0.5 mas.

The derived distribution of the components is presented in Fig. 3a. The crosses show the relative errors of the component positions; their relatively large values are due to the inconsistency of the initial model assumptions with the actual observed pattern, in particular, the overlap of the lines of several components within a channel [10, pp. 21–22], and to the presence of an extended structure. The fine structure of the flare region consists of components distributed in three compact groups (Fig. 3a, Table 2). The first group forms a bright extended arc, while the other two are separated from it by ≃1 and ≃0.5 mas. The sizes of the groups of compact components are 0.2–0.9 mas, and their brightness temperatures T_b reach $\leq 10^{16}$ K.

However, there may be errors related to inaccurate compensation of the derivative $d\varphi/df \leq 5°$ per channel, which can reach ≤0.05 mas per channel.

7. INTERPRETATION OF THE RESULTS

The distribution of the components in the first group (No. 1) in the X–Y plane (Fig. 3a) has an arclike shape. The component amplitudes smoothed with a Gaussian beam have a characteristic appearance, which is presented in Fig. 3c. In the first group, we can see a certain correlation between the velocity of the components and their relative position. Figure 4 shows the velocity distribution of the components along the group structural angle ($Q = -86°$). Such dependences are typical of components that form a ring structure observed at a small viewing angle $\gamma \approx 0°$–$1°$.

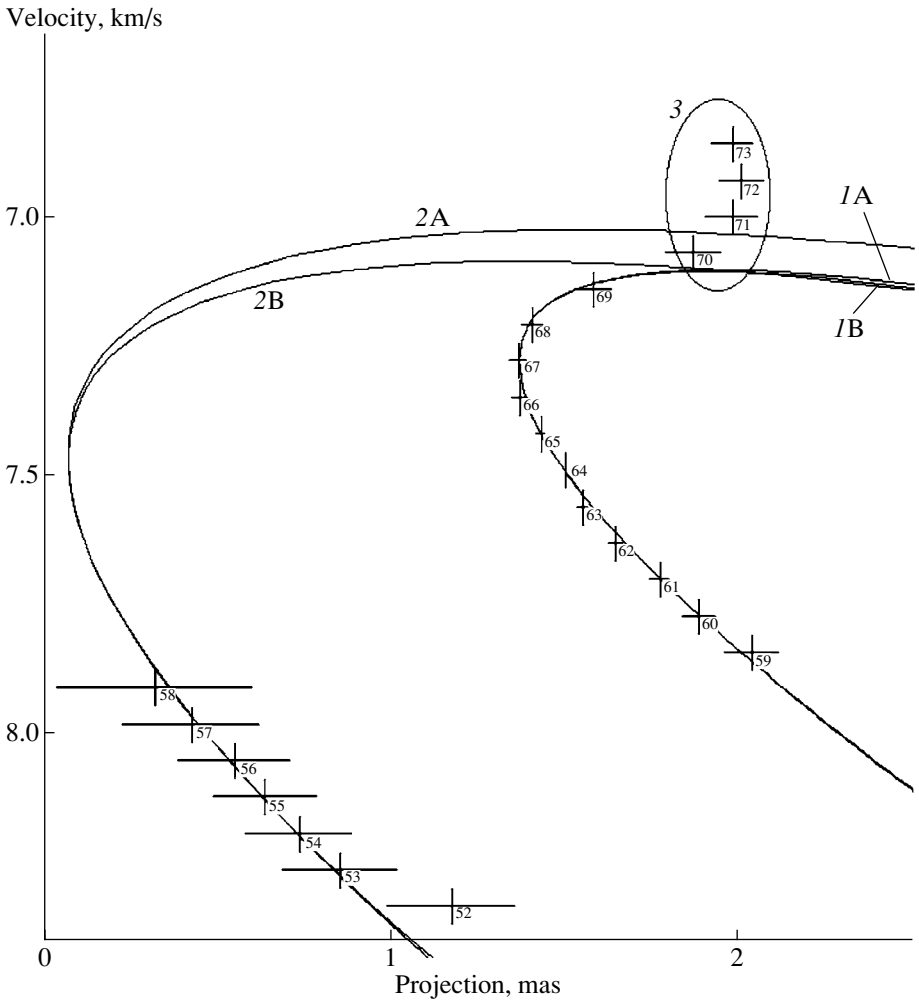

Fig. 4. Velocities of the components versus their relative positions. (*1*) first ring; (*2*) second ring; A and B correspond to $R = 6$ and 15 AU, respectively.

Consider a ring with radius R and thickness $r \ll R$ rotating at velocity $V_{\rm rot}$ and expanding at velocity $V_{\rm rad}$ (Fig. 5). In this case, the radial component of the velocity of a ring element $V_{\rm obs}$ as a function of angle α is

$$V_{\rm obs} = V_{\rm LSR} + V_{\rm rad}\sin\alpha + V_{\rm rot}\cos\alpha,$$

where $V_{\rm LSR}$ is the velocity with respect to the Local Standard of Rest.

Depending on the relative position Δx (Fig. 5), the observed velocity of a ring element is

$$V_{\rm obs} = V_{\rm LSR} + V_{\rm rot}\left(1 - \frac{\Delta x}{R}\right) + V_{\rm rad}\sqrt{\frac{2\Delta x}{R} - \frac{\Delta x^2}{R^2}}.$$

At point S ($\Delta x = 0$), the radial component of the expansion velocity $V_{\rm rad} = 0$ and $V_{\rm S} = V_{\rm LSR} + V_{\rm rot}$. If the position is measured from point S, the observed velocity is

$$\Delta V_{\rm obs} = V_{\rm rot}\left(-\frac{\Delta x}{R}\right) + V_{\rm rad}\sqrt{\frac{2\Delta x}{R} - \frac{\Delta x^2}{R^2}}.$$

Table 3. Parameters of the rings

Central mass, $M_\odot$	Ring no.	$V_{\rm rot}$, km/s	$V_{\rm rad}$, km/s	R, AU
0.1	1	3.62	1.11	6
	2	3.44	1.78	6.6
1	1	8.98	1.79	15
	2	8.79	2.61	15.6

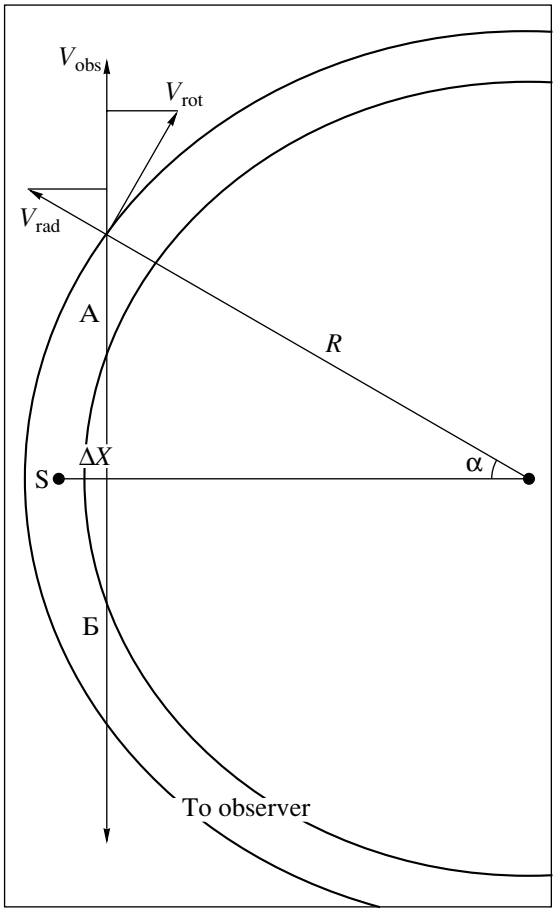

Fig. 5. A rotating and expanding ring.

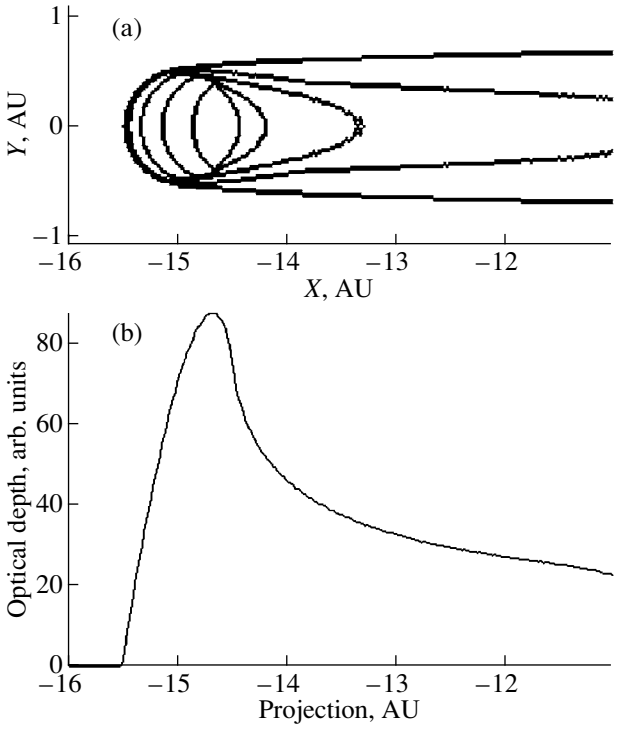

Fig. 6. Distribution of optical depth (τ_{opt}) in a ring observed at angle $\gamma = 1°$ (a) in the X–Y plane (the contour levels correspond to 0.2 of the maximum) and (b) projected on the X axis.

Let us estimate the ring parameters via a least-squares fit. We assume the values of the radii are 6 and 15 AU (Fig. 4, curves 1A and 1B, respectively; Table 3). These correspond to rotation velocities $V_{rot} =$ 3.62 and 8.98 km/s and to radial velocities $V_{rad} =$ 1.14 and 1.79 km/s.

The radial component of the ring velocity testifies to the system's non-stationarity, consistent with the early stage of formation of a protostar and the accompanying accretion disk. In fact, the observed non-stationarity of the ring could be due to the expansion or contraction not of the ring itself, but of the maser halo around it. This protoplanetary ring contains ice particles and dust. The infrared radiation from the protostar (central object) sublimates ice particles, forming water-vapor molecules, which are blown away by the radiation pressure and stellar wind. They also determine the maser pumping, so that an expanding maser ring is formed. We observe a similar phenomenon as a comet flies close to the Sun. The inverse effect—the contraction of the ring under the action of the accreting material—is possible, but the halo will then be localized in the inner part of the ring.

Let us estimate the mass of the central massive body M assuming Keplerian motion:

$$RV_{rot}^2 = MG, \qquad (5)$$

where G is the gravitational constant. For the considered radii, $R = 6$–15 AU, the mass of the central object M is 0.1–$1 M_\odot$, within the range of masses for brown dwarfs and protostars.

Near the group of components considered is group no. 2 (Table 2, Fig. 3a), which is probably a fragment of a second, outer ring. In this case, according to (5), its velocities are $V_{rot} = 3.44$–8.79 km/s, $V_{exp} =$ 1.78–2.61 km/s (Fig. 4, curves 2A, 2B). The group of components no. 3 is probably a fragment of another ring; however, the number of points is obviously insufficient to determine its parameters.

8. PARAMETERS OF THE MASER RING

The brightness distribution of a maser ring with radius R and thickness $2r = 1$ AU, observed at some angle γ, depends on the distribution of water-vapor molecules and the maser pumping. Let us assume a uniform distribution for the water vapor and pumping in the ring, a radius $R = 15$ AU, and an angle to the line of sight $\gamma \approx 1°$, as follows from Fig. 3a.

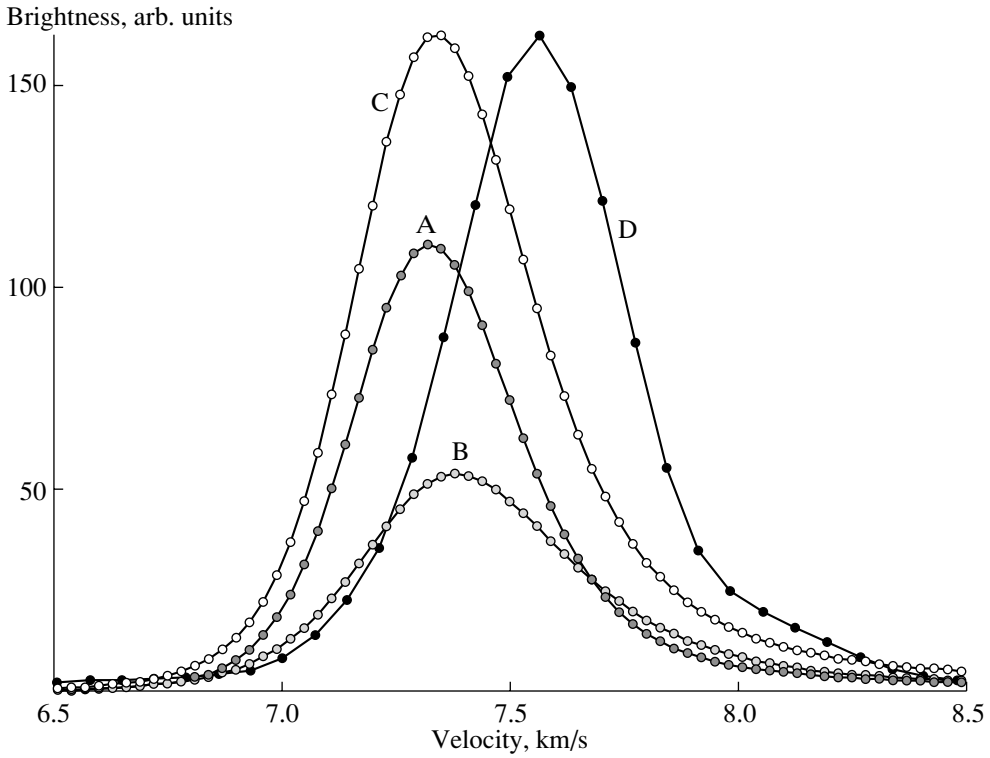

Fig. 7. (A) Inner ring ($V_{\rm rot} = 8.98$ km/s), (B) outer ring ($V_{\rm rot} = 8.79$ km/s), (C) sum A + B, (D) the observed profile.

The intensity of the maser emission I is determined by its optical depth $\tau_{\rm opt}$ and the spontaneous kinetic temperature of the active region $T_{\rm s}$ and background $T_{\rm b}$. In an unsaturated maser, the intensity is

$$I = \frac{F}{\Omega} = \frac{2k}{\lambda^2}\left[|T_s|\left(e^{\tau_{\rm opt}} - 1\right) + T_{\rm b}e^{\tau_{\rm opt}}\right],$$

where k is Boltzmann's constant and Ω is the angular size.

The background temperature $T_{\rm b}$ can be taken to be equal to the average brightness temperature of the nebula ($\approx$10 K), and T_s is $\approx$100–200 K. Thus, the observed maser emission intensity is determined by spontaneous emission [5]:

$$I \sim T_s(e^{\tau} - 1).$$

Let us find the optical-depth distribution in the ring in the plane of the sky, assuming it is proportional to the line-of-sight component of the geometrical cross section. We will take into account the distribution of the velocity in the ring along the line of sight (the maser window width).

The linewidth of an unsaturated maser is determined by the expression [5]

$$\Delta f = \Delta f_{\rm D}\frac{1}{\sqrt{\tau_{\rm opt}}},$$

where $\Delta f_{\rm D}$ is the Doppler linewidth (kHz), $\Delta f_{\rm D} = 3.73\sqrt{T_{\rm k}}$.

For a given velocity V, the line-of-sight (L) optical depth is

$$\tau_{\rm opt}(x, y, V) = \tau_{\rm opt0}(x, y)\int e^{-\frac{(V - V_0(x,y,L))^2}{0.36\Delta V^2}}dL,$$

where $\tau_{\rm opt0}$ is the geometrical thickness of the maser ring and V_0 is the velocity of the line center of a small volume (dx, dy, dL).

This integral can be calculated numerically by splitting the model into a large number of small volumes (Δx, Δy, ΔL, Δv). Let us assume $\Delta V = 0.8$ km/s, which corresponds to $T_{\rm k} = 240$ K. The derived dependence $\tau_{\rm opt}(x, y)$ is shown in Fig. 6a. The lines of equal optical depth are drawn in steps of 0.2. The optical-depth variations projected onto the X axis are presented in Fig. 6b. The maximum intensity corresponds to a compact region located at the ring inflection point. The size of the region (bright source) does not exceed half the ring cross section, and depends on the optical depth and maser mode. In the case considered here, the apparent angular size of the compact source is $\approx 0.5 \times 0.9$ AU, or 1×1.8 mas.

The velocity distribution of the observed intensity—i.e., the line profile of the ring, $F(V)$—is shown in Fig. 7 (curve A). Curve B in Fig. 7 shows the analogous dependence for the second ring ($R = 15.6$ AU, $V_{\rm rot} = 8.79$ km/s, $V_{\rm exp} = 2.61$ km/s). The total curve C has a maximum at $V_m = 7.3$ km/s, whereas the

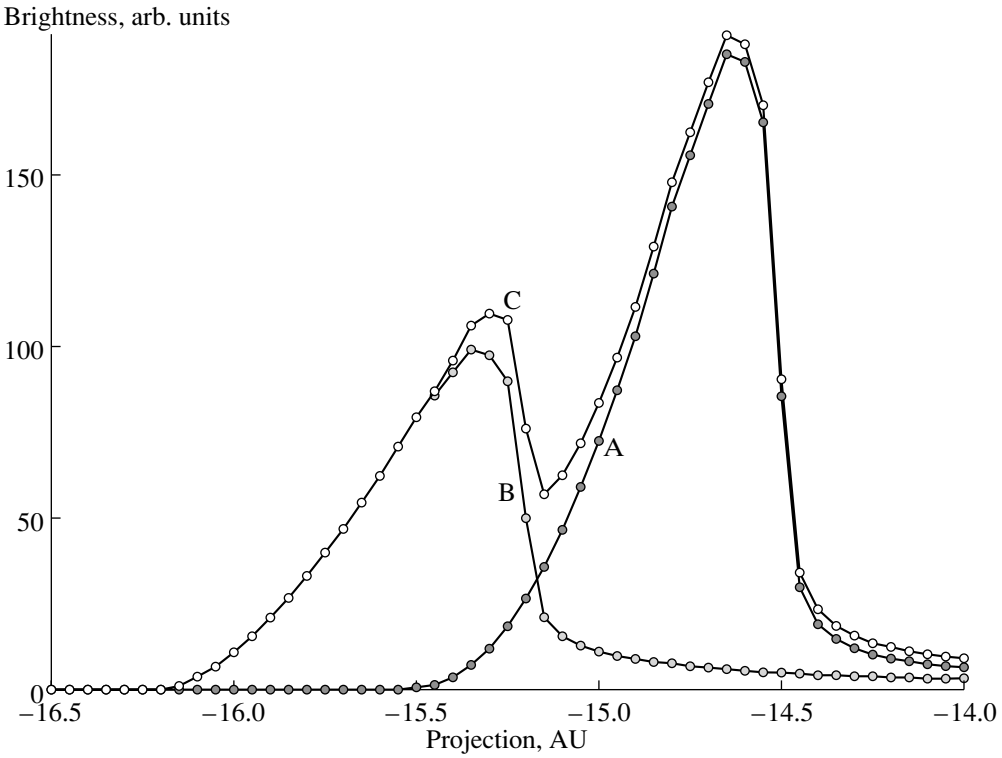

Fig. 8. Brightness distribution along the X axis; (A) inner ring; (B) outer ring; (C) sum A + B.

observed curve D peaks at $V_m = 7.56$ km/s, which can be explained by amplification of the emission in an external maser cloud [7], whose radial velocity $V_{\rm emc}$ is 7.6 km/s, and profile width is ∼0.5 km/s.

The brightness distribution along the X axis, $T_{\rm b}(x)$, for the first and second rings are shown by curves A and B in Fig. 8. The total brightness-distribution curve includes large-scale (≈1 AU) and compact (≈0.3 AU) components (2 and 0.6 mas, respectively). However, the external amplification and degree of saturation substantially influence the contribution of the individual components to the total emission profile.

Thus, as a whole, the model of the maser source is consistent with the observed correlations and confirms that the observational data are consistent with a ring structure.

9. CONCLUSION

Using observations of a polarized flare of the H_2O supermaser emission in the Orion Nebula at $\lambda =$ 1.35 cm on December 1, 1982, on a radio interferometer formed by antennas in Simeiz, Onsala, and Effelsberg, we have obtained the following results.

We have modeled the spatial structure of the flare region as a set of pointlike sources (δ functions) and Gaussian components. The components are distributed in three groups. In the main group, the components are distributed along an arc 0.9 mas in length and oriented in the plane of the sky along position angle $Q = -86°$. This arc is a segment of a circle, inclined to the line of sight at an angle of $\gamma \approx 1°$. The accuracy of the relative positions of the components is shown in Fig. 3a.

The components emit narrow spectral lines. The linewidth of the emission of the bright groups of components (nos. 1, 2) is 15–50 kHz, or 0.2–0.7 km/s.

The main emission of the flare is contributed by an elongated extended component, whose size in a Gaussian approximation is 1.1×1.9 mas. Its brightness temperature $T_{\rm b}$ is 2.0×10^{15} K. Compact components are scattered within this region, one with a size of 0.3×0.9 mas and a brightness temperature of $T_{\rm b} = 2.6 \times 10^{15}$ K. The presence of still more compact components with sizes of < 0.2 mas is possible, with their contribution to the emission being ≈5%.

The degree of polarization P of the maser emission of both the extended and compact components is 58%.

The spatial distribution of the components and their velocities fit a model with rotating and expanding rings (components nos. 1, 2) with radii differing by ≈0.7 AU. Component no. 3 may correspond to a third ring.

The expansion velocity of the maser ring is determined by the velocity of blown-off water-vapor molecules, which form a halo around a protoplanetary ring consisting of ice particles.

In the case of Keplerian rotation and a protostar mass of $0.1-1M_\odot$, the radius of the inner ring is $R = 12-30$ mas (6–15 AU), its rotation velocity is $V_{rot} = 3.62-8.98$ km/s, and its expansion velocity is $V_{rad} = 1.14-1.79$ km/s. The data for the other two rings are listed in Table 3.

Thus, the observational data can be represented by a model with expanding concentric rings observed at a small angle to the line of sight.

ACKNOWLEDGMENTS

L.I.M. thanks the NRAO staff for the opportunity to correlate the data and for hospitality. This project was supported by the Russian Foundation for Basic Research (project no. 99-02-01) and the Ministry of Science and Technology (Astronomy Program). The authors are grateful to R.D. Dagkesamanskiĭ for helpful comments.

REFERENCES

1. B. F. Burke, K. J. Johnston, and V. A. Efanov, Astron. Zh. **49** (3), 465 (1972) [Sov. Astron. **16**, 379 (1972)].
2. Z. Abraham, N. L. Cohen, R. Opher, *et al.*, Astron. Astrophys. **100**, L10 (1981).
3. G. Garay, J. M. Moran, and A. D. Haschick, Astrophys. J. **338**, 244 (1989).
4. L. I. Matveenko, Pis'ma Astron. Zh. **20** (6), 456 (1994) [Astron. Lett. **20**, 388 (1994)].
5. R. Genzel, D. Downes, J. M. Moran, *et al.*, Astron. Astrophys. **66**, 13 (1978).
6. L. I. Matveenko, Pis'ma Astron. Zh. **7** (2), 100 (1981) [Sov. Astron. Lett. **7**, 54 (1981)].
7. L. I. Matveenko, P. J. Diamond, and D. A. Graham, Astron. Zh. **77** (9), 669 (2000) [Astron. Rep. **44**, 592 (2000)].
8. L. I. Matveenko, P. J. Diamond, and D. A. Graham, Pis'ma Astron. Zh. **24** (10), 723 (1998) [Astron. Lett. **24**, 623 (1998)].
9. L. I. Matveenko, Preprint No. Pr-2013, IKI RAN (Institute for Space Research, Russian Academy of Sciences, Moscow, 1999).
10. V. A. Demichev, K. M. Zakharin, and L. I. Matveenko, Preprint No. Pr-2040, IKI RAN (Institute for Space Research, Russian Academy of Sciences, Moscow, 2001).
11. A. R. Thompson, J. M. Moran, and G. W. Swenson, Jr., *Interferometry and Synthesis in Radio Astronomy* (Wiley, New York, 1986; Mir, Moscow, 1989).

Translated by G. Rudnitskiĭ